UNIVERSITY OF SUSSEX SCHOOL OF GLOBAL STUDIES
GEOGRAPHY DEPARTMENT

Saharan Heat Low: A Comprehensive analysis of thermodynamics, dynamics and associated variability

A thesis submitted for the partial fulfilment of degree of Doctor of Philosophy

Netsanet Alamirew

2/8/2018

DECLARATION

I confirm that this is my own work and the use of all material from other sources has been properly and fully acknowledged.

Netsanet Alamirew

Abstract

During summertime Saharan heat low, a region of low pressure system, is formed as a result of large solar insolation superimposed with the convergence of west African South westerly monsoon flow and dry north easterly Harmattan flow along the intertropical discontinuity. This region plays significant role in the initiation and development of the West African Monsoon. The Saharan heat low is co-located with region of maximum load of dust aerosol which is known to have impact on the climate. Further the Saharan heat low plays key role in the global circulations including its role in formation of African Easterly Jets and African Easterly Waves. Despite its role in influencing the dynamic and thermodynamics of the region, the Saharan Heat low is not extensively studied partly due to lack of comprehensive data due to the harsh weather conditions of the region.

Climate system of the Saharan heat low is a result of different complicated atmospheric and land surface processes most dominantly immense solar input at the surface, large convergence of sensible heat flux from the ground into the atmosphere, and low level cooling by horizontal advection of moisture from the surrounding area. These dynamical and thermodynamical processes take part in transport and redistribution of heat and transport of the moisture in the region.

This thesis aims at providing a detailed analysis of the physical processes responsible for the development, maintenance, and decadal variability of the Saharan heat low region. I investigate three specific aspects of the Saharan heat low region.

1. **Heat and Moisture Budget**: Heat and moisture are drivers of dynamics and thermodynamics of a region. Previous studies presented heat and moisture budget of the Saharan heat Low without attributing to the detailed mechanisms by which heat and moisture is transported from the surrounding area to the Sahara heat low and vice versa. This thesis presents components of heat and moisture budget resulting from mean and transient flows that are responsible for heating/cooling and moistening/drying of the Sahara heat low region. Heat and moisture budget are derived using commonly used reanalyses simulations (ERA-I, NCEP, and MERRA) and comparison of the results between the three reanalyses are made. I investigate the mechanisms responsible for the decadal variability of intensity of the Sahara heat low and provide implications. This work has not been done previously to the best of knowledge.

2. **Role of Dust and Water vapor in controlling the radiative flux**: Recent studies show that water vapour greenhouse forcing is responsible for

intensification of the Saharan heat low and as a consequence recovery of Sahel rainfall. Dust aerosol is known to have impact on the climate through its interaction with radiation. The large dust load in the Sahara heat low makes it important in controlling the variability in the radiative budget of the region. Previous studies have quantified the role of dust and water vapour in the region in controlling day to day variability in the radiative flux in the heat low. There is still uncertainty in the radiative forcing and associated variability partly due to lack of observational data. Furthermore separating the radiative effect of dust from that of water vapour is challenging due to the co-variability of dust and water vapour. This thesis quantifies separate and combined effect of dust and water vapour in controlling the radiative flux of the Saharan heat low using the recently made FENNEC observations of meteorological variables and dust loading. Theoretical experiments are made to study sensitivity of radiative flux to variations in dust and water vapour.

3. **Characteristics of convective density currents**: Convective down drafting density currents (cold pools) are ubiquitous features of the Saharan Heat low region which are shown to play important role in the transport of moisture and emission of dust in the region. Despite this, the characteristics of these atmospheric processes are not well studied in the Sahara Heat Low. Improving our knowledge of properties of convective density currents is imperative to better understand atmospheric processes within boundary layer of the Saharan heat low and thus improve model simulation performance. Here I provide magnitude, spatial distribution, and seasonal variability of cold pools using data from the Automatic weather Station (AWS) spread over the Sahara desert. I implement a unique identification method which is further verified by satellite observations of cold pool signatures. Once cold pools are identified at all stations, statistical description of the occurrence frequency and distribution are presented. Finally I asses reanalyses model simulation of convection triggered cold pool outflows through comparison with measurements.

Acknowledgement

My special thanks goes to both my supervisors, Prof. Martin Todd and Dr. Yi Wang. I am grateful to Martin who has been by my side throughout this journey providing me continuous guidance and support. Martin has helped me to believe in myself and now I do feel that I can do research and contribute in the field of climate science. I would like to thank Martin for recommending me and helping me attend a number of trainings and conferences which were important part of learning process. I gained insight to new ideas of climate science in these events. Getting the balance between study and family commitment was a challenging aspect during my PhD. I thank Martin for being extremely patient and encouraging during these times. Most importantly I would like to sincerely thank Martin for being such a nice human being. Martin I always feel privileged for getting this chance to work with you. But I do not want to hide my regrets that I should have gained more from Martin than I did. I also thank Yi for his support including facilitating admin stuffs right from the beginning of my PhD. I am thankful to Yi for getting me involved in the McGaill project. I further built my skill in climate modelling in this project, the payment was also good. Thank you Yi for being encouraging and friendly. Without both Martin and Yi this PhD would not have come to this stage.

I like to thank Peter Carpenter for providing the fund required to undertake my PhD. This fund has given opportunity for talented students from Africa get high level education and training, particularly climate related science which otherwise would have been challenging. Africa being the most vulnerable continent to climate change impacts, needs scientists who can provide scientific information to decision makers. Peter Carpenter is doing a great job in this regard.

I would like to thank John Marsham for sharing his academic expertise during my visit at Leeds and through email exchanges. I am thankful for Claire Ryder who has helped me learn radiative transfer code during my visit at Redding. I also thank all the FENNEC group for providing valuable comments at the beginning of my PhD. I am thankful for all my office colleagues who has made PhD more enjoyable. I would like to thank Carolina Cavazos Guerra (former post doc) for helping me get used to the linux system here in Sussex and learn how to run WRF model on the famous Apollo (our supercomputing cluster in Sussex!) where I spent pretty lot of time of my PhD.

And last I would like to thank my wife, Mahider and my son Fitsum for being loving, caring, supportive, as well as patient throughout my study.

Netsanet Kassa Alamirew

Feburary, 2018

List of Acronyms and their definitions

AEJ: Africa Easterly Jet
AERONET: AErosol RObotic NETwork
AEW: Africa Easterly Wave
AMJJA: April May June July August
AMMA: African Monsoon Multidisciplinary Analysis
AOD: Aerosol Optical Depth
ARG: Averaged Rectified Geolocated
AWS: Automatic Weather Station
BBM: Bordj Badji Mokhtar
BLH: Boundary Layer Height
BTD: Brightness Temperature Differences
CALIOP: Cloud-Aerosol Lidar with Orthogonal Polarization
CALIPSO: Cloud Aerosol LIDAR Infrared Pathfinder Satellite Observations
CERES: Cloud and the Earth Radiant Energy System
CCN: Cloud Condensation Nuclei
DABEX: Dust and Biomass Experiment
DODO: Dust Outflow and Deposition to the Ocean
DRE: Direct Radiative Effect
ECMWF: European Centre for Medium-Range Weather Forecasts
EBAF: Energy Balanced and Filled
GERBILS: Geostationary Earth Radiation Budget Intercomparison of Longwave and Shortwave radiation
GERB: Geostationary Earth Radiation Budget
HVR: high resolution visible
IN: Ice Nuclei
IOP: Intensive Observation Period
IQR: Inter-Quartile Range
ITD: Inter-Tropical Discontinuity
JJA: June July August
LLAT: Low Level Atmospheric Thickness
LLJ: Low Level Jet
MEC: Mass Extinction Coefficient
MERRA: Modern-Era Retrospective analysis for Research and Application
MSG: Meteosat Second Generation

NCEP: National Centre for Environmental Prediction

NWP: Numerical Weather prediction

RGB: red-green-blue

RMSE: Root Mean Square Error

RT: Radiative Transfer

SAMUM: SAharan Mineral dUst experiMent

SEVIRI: Spinning Enhanced Visible and InfraRed Imager

SHF: Sensible Heat Flux

SHL: Sahara Heat Low

SOCRATES: Suite Of Community Radiative Transfer codes based on Edwards and Slingo

SS1(2): Super Site One(two)

SSA: Single Scattering Albedo

SST: Sea Surface Temperature

TCWV: Total Column Water Vapour

TOA: Top of Atmosphere

WAM: West African Monsoon

Table of Contents

CHAPTER I

1.1 Introduction

Sahara desert which engulfs most of North Africa surrounded by the Red sea in the east and the Atlas Mountains and Mediterranean in the north to Atlantic Ocean in the west is the hottest desert in the world. The characteristics of the atmosphere and land surface, including dry features and prevailing high temperature, make the Sahara desert an important component of global climate system. The Sahara desert is also known for being the largest source of dust in the world (Prospero et al., 2002; Tanaka and Chiba, 2006; Washington et al., 2003). It is estimated that more than half of the global dust is emitted from the Sahara desert. Climate models estimate dust emission from Sahara desert ranges from 200 to 3000 Tg yr^{-1} (Huneeus et al., 2011).

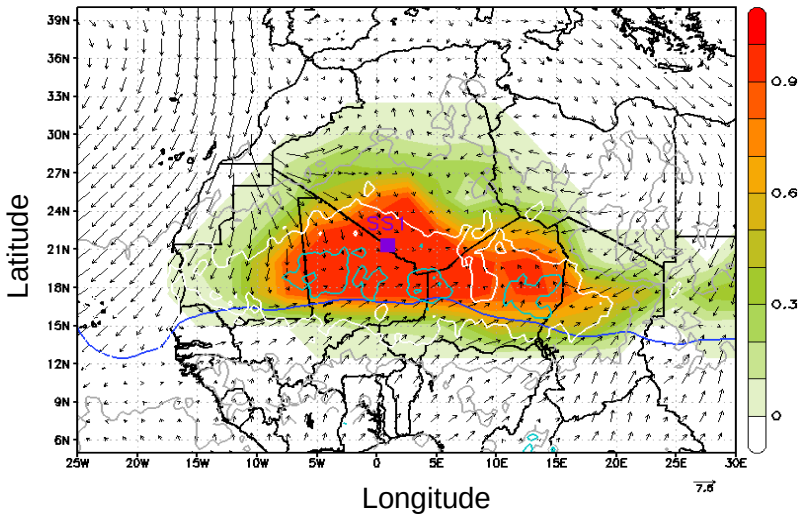

Figure 1.1. Climatological state of the Saharan heat Low region (mean June from 1979-2013): SHL location, low level circulation, and dust load. Shaded: the mean position of heat low region (occurrence frequency of 90% of llat), arrows: mean 925 hPa wind (m s^{-1}), Blue Line: the mean position of the inter-tropical discontinuity from ERA-Int reanalysis data (925 hPa 10 g Kg^{-1} specific humidity) and aerosol optical depth (AOD) from satellite MISR data (contour intervals are 0.4, 0.6, and 0.8 for grey, white, and cyan lines respectively). The purple rectangle denotes location of the FENNEC Supersite 1 (SS1)

During the northern hemisphere summertime a low-pressure region, known as Saharan Heat Low (SHL), is formed embedded within the Sahara desert over northern

Mali, southern Algeria, and eastern Mauritania (fig. 1.1). SHL is known for its unique extreme features: high surface temperature or equivalently low surface pressure (Lavaysse et al., 2009;Messager et al., 2010a) with little or no precipitation and being largest source of dust on the planet. The large insolation over the region is the prime driver for the formation of the heat low resulting in surface temperature as high as 40 ^{0}C during summer (fig. 1.2). The excess solar energy at the surface is converted to sensible heat that triggers deep atmospheric convection with a well-mixed boundary layer during the day. The SHL is known for its deepest Planetary Boundary Layer (PBL) on Earth, often extending up to ~4 - 5 km (Marsham et al., 2013b). Coupled with synoptic circulations, the SHL is a dominant component of the region's dynamical system playing key role in: (i) initiation of west Africa monsoon (Sultan and Janicot, 2003), (ii) influencing the structure and development of Africa Easterly Jets(AEJs) (Thorncroft and Blackburn, 1999), and (iii) driving precipitation over Sahel (Evan et al., 2015;Lavaysse et al., 2010a).

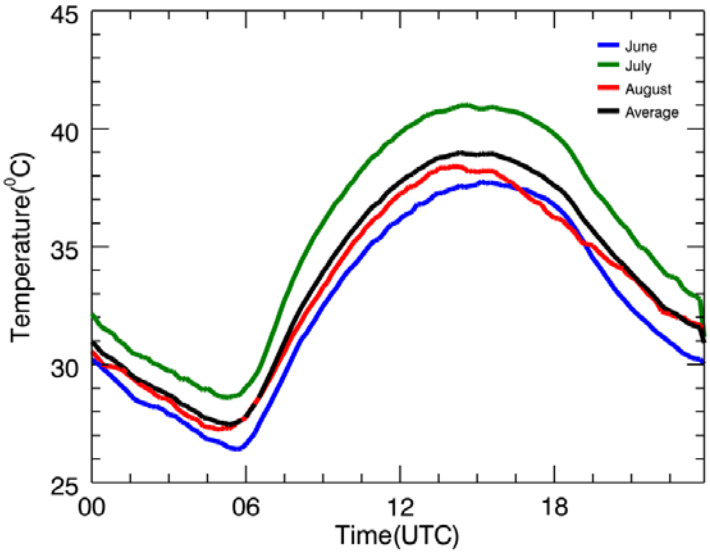

Figure 1.2 Mean 2m air temperature averaged for all Automatic Weather Stations (AWS stations, see chapter II) during summer months in 2011.

Despite its key role in regional dynamics and thermodynamics, the detailed processes within the Sahara heat low region, associated variability and its link with the West Africa monsoon system and Sahel rainfall are not well understood. Both observational evidences and model simulations prove that the Saharan Heat Low region display decadal warming trend, sometimes termed as 'desert amplification' (Cook & Vizy, 2015; Evan, Flamant, et al., 2015; Lavaysse, 2015; Lavaysse et al., 2016; Wei et al., 2017; Zhou, 2016). However there is still no clear unanimity on the

causes of warming of the Saharan heat low. In line with this, some publications show recovery in Sahelian rainfall to be correlated with intensification of SHL (Biasutti et al., 2009; Evan, Fiedler, et al., 2015). Others contradict the idea that SHL intensification has enhancing effect on Sahelian rainfall (Shekhar & Boos, 2017). A lot of publications suggest the cause of recovery for Sahel precipitation from severe draught in the 1970's and 1980's to be anomalies in SST (Giannini et al., 2013; Giannini et al., 2003; Hagos & Cook, 2008; E. R. Martin et al., 2014; Roehrig et al., 2013). It is also argued that global temperature increase due to greenhouse increase is driver of enhanced Sahel precipitation (Cook & Vizy, 2015; Dong & Sutton, 2015).

The points stated above suggest the need to investigate the causes of variability of the SHL and its link with Sahel precipitation. The dominant factor responsible for the circulation within SHL is temperature gradient between the hot SHL and the cooler surrounding ocean driving advection of moisture towards the heart of the Saharan desert which includes the summer West African Monsoon (WAM), (Lavaysse et al., 2009;Parker et al., 2005;Sultan et al., 2003), surges from Mediterranean sea (Lavaysse et al., 2010b;Vizy and Cook, 2009), and the Atlantic inflow (Grams et al., 2010) inflow. The variability in SHL intensity modulates moisture transport, convective activity, and thus precipitation within the surrounding region most importantly on the WAM across a range of timescales, including (i) the synoptic (Couvreux et al., 2010) to intra-seasonal (Chauvin et al., 2010) (ii) mean seasonal (Sultan and Janicot, 2003;Xue et al., 2010) (iii) inter-annual and decadal through to future climate change in the WAM (Martin and Thorncroft, 2014;Roehrig et al., 2013). On longer time scales SHL is observed to have a positive trend in surface temperature which is attributed to different causes (Dong and Sutton, 2015;Evan et al., 2015;Lavaysse et al., 2016;Vizy and Cook, 2009). The exact cause for warming trend of the SHL is still unknown (Lavaysse, 2015).

Lavaysse et al. (2009) have studied the seasonal evolution of the SHL. They proposed a method for detection of the seasonal evolution of the SHL using differences in geopotential heights at 700 hPa and 925 hPa, which they refer it as Low Level Atmospheric Thickness (LLAT). Over the annual cycle, they showed the SHL core migrates from a position south of the Darfur mountains (centred on ~6N, 20E) in winter to central western Sahara (centred on ~23N,3W) in summer (fig. 1.1) covering much of northern Mauritania, Mali and Niger and Southern Algeria. The annual seasonal displacement of the heat low region is linked with the transition of the maximum surface temperature resulting from solar insolation. Northwest (rather than north) shifting of the heat low region from winter to summer is argued to be associated with the orography of

the region (Drobinski et al., 2005;Semazzi and Sun, 1997). Figure 1.3 displays the seasonal evolution of location of the SHL region in a year averaged from 1979-2015.

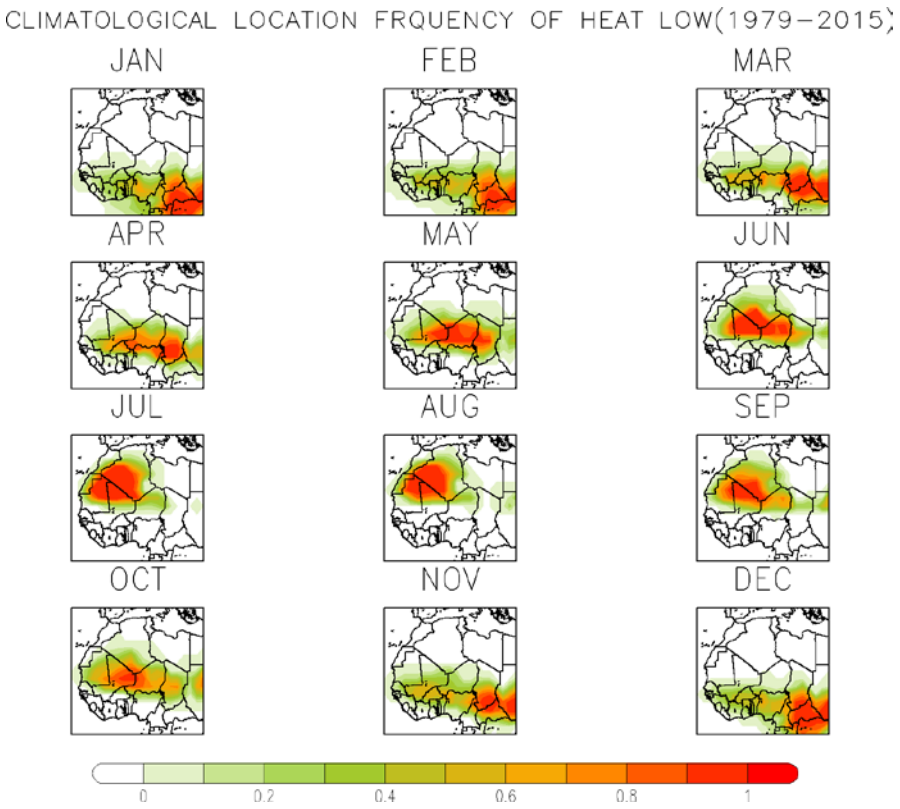

Figure. 1.3 Climatological Occurrence Frequency (colour) of West Africa Heat Low Region averaged from 1979-2015, Era-Int data

In relation to this Chauvin et al. (2010) investigated the intra-seasonal variability of SHL and its link with mid-latitudes. They identified two modes variability (namely west phase and east phase) using composite analysis of 850 hPa potential temperature. The west phase is associated with changes in the Atlantic westerly polar jet and the North Africa subtropical westerly jet configurations while the east phase is associated with large extension of the Azores anticyclone over Europe and western Mediterranean. In both phases they showed west (east) anomalous temperature propagation in southeastward (southwestward) and concluded the SHL bridges the mid-latitudes and the West African monsoon. The variability of the climate system of SHL has been extensively studied by many authors (Chauvin et al., 2010; Couvreux et al., 2010; Parker et al., 2005; Peyrille & Lafore, 2007; Thorncroft & Blackburn, 1999; Xue et al., 2010). Despite large volume of study, there is still a need for better understanding of the physical processes causing variability within the SHL.

In addition to the important dynamical aspects mentioned above, the SHL is region of largest dust loading on the globe during boreal summer (Engelstaedter et al., 2006) which has various environmental and climate impacts. There are various mechanisms responsible for dust uplift including low level jets(LLJ, Washington and Todd (2005)), dry convection (Ansmann et al., 2009), monsoon surges (Karam et al., 2009), and cold pool outflows (Allen et al., 2013;Heinold et al., 2013;Marsham et al., 2013b). The contribution of each mechanism to the total dust loading in the Sahara heat low has been estimated in recent studies (Allen et al., 2013;Heinold et al., 2013) but the total dust loading in the region still remains uncertain. Dust aerosol is known for altering the radiation budget on top of atmosphere, within the atmosphere, and surface of the Sahara desert (Ansell et al., 2014;Banks et al., 2014;Haywood et al., 2005;Marsham et al., 2016;Yang et al., 2009). Dust is also known for its impact on atmospheric circulation as a consequence of its radiative effect (Evan et al., 2011;Solmon et al., 2012;Stanelle et al., 2010). Atmospheric dust particles emitted from the Sahara desert are transported to large distances eventually being deposited providing nutrient to ocean (Jickells et al., 2005) and on land such as the Amazon (Bristow et al., 2010). In addition, dust may affect visibility and thus causing impact on aviation (Weinzierl et al., 2012). There is also evidence that dust can be health problem on dryland and downwind environments (Goudie, 2014). The above reasons make dust an important component of the atmosphere which needs interdisciplinary study.

There is large uncertainty associated with climate effect of dust (predominantly radiative effect) partly due to lack of accurate knowledge on the optical properties of dust. On a global scale magnitudes of the radiative effect of dust are uncertain that it is still not clear atmospheric dust has a net cooling or heating effect on global climate. A recent study using dust observational and chemical model transport simulations, (Kok et al., 2017) estimate the direct radiative effect of dust to be in the range -0.48 and +0.28 W m^{-2}. In a similar study an estimated -0.3 and +0.1 W m^{-2} (Myhre et al., 2014) direct radiative forcing of anthropogenic dust, which constitutes 20% of total dust, is reported in the Intergovernmental Panel on Climate Change (IPCC) assessment report 5. A number of field campaigns have been taking place near Sahara desert to better understand dust properties and its influence on the regions climate. Table 1.1 summarises mineral dust field campaigns carried out near the dust sources of the Sahara desert. Despite the continuing experimental and modelling studies and substantial progresses, there still exists unanswered questions concerning the role of dust in the climate system (Ansmann et al., 2011; Ryder et al., 2015). Given the large presence of dust and its key role in the atmosphere of region, there is a research need

to determine and hence improve the radiative forcing of dust and its role in shaping the dynamics of the SHL.

Table 1.1 List of experimental dust field campaigns in the vicinity of Sahara

Campaign Acronym	**Campaign Time**	**Campaign Location**	**Campaign Objective**	**Reference**
AMMA	Jan and Feb 2006	West Africa	Characterize Saharan aerosol and biomass-burning aerosols from West Africa	(Redelsperger et al., 2006)
DABEX	Jan and Feb 2006	Niger	Same topic as AMMA-SOP0	(Haywood et al., 2008)
DODO	Feb and Aug 2006	West Africa	Characterize Saharan dust in two seasons, constrain model simulations, quantify deposition of iron to the North Atlantic Ocean	(McConnell et al., 2008)
SAMUM-1	May and Jun 2006	Southern Morocco	Characterize Saharan aerosol near the source region and quantify dust-related radiative effects	(Heintzenberg, 2009)
GERBILS	Jun 2007	North Africa	Geographic distribution and physical and optical properties of Saharan dust, impact on radiation, validation of satellite retrievals and numerical weather prediction models	(Haywood et al., 2011)
FENNEC	Apr and Jun 2011, Jun 2012	Algeria and Mauritania	Improve understanding of the Saharan climate system through a synergy of observations and modeling	Washington et al. (2012); (Ryder et al., 2015)

For the two major reasons, i.e. role on the dynamical system of the region more importantly on WAM and being large source of dust emission, the SHL has attracted

the attention of researchers around the globe. A progress has been made in the past two decade and our understanding of the different components of the climate system of the region has improved. Despite the ongoing efforts, there still remains a gap in our understanding on the detailed physical processes and variability that lead to the formation and maintenance of the SHL. The scarce ground observational dataset due to the harsh weather conditions has hindered the research at least partly. This thesis will try to help fill the gap by providing a comprehensive analysis of different aspects of the SHL. As a part of understanding the climate system of the SHL region, I first provide a brief description of the main known features of the climate system of the region followed by defining the research objectives of this thesis. The remainder of this chapter is organized as follows. Section 1.2 presents an overview of components of climate systems of the SHL region which are responsible for its development and evolution. This will be followed by giving roles of dust and water vapour in the climate system of the region which is given in section 1.3. A review of literature from selected past papers is summarized in section 1.4. Last I define the objectives of that this research work in section 1.5.

1.2 Overview of the Saharan Heat Low summertime Climate System

1.2.1 Energy budget of Sahara Heat Low

Deserts are known by the large intake of direct solar radiation which controls the surface and atmospheric state. The net surface radiative energy Q^R at any time of a day is given by:

$$Q^R = Q_G + Q_H + Q_L \tag{1.1}$$

where Q_G is ground conduction flux, Q_H is sensible heat flux, and Q_L is latent heat flux. In deserts the radiation budget equation is characterized by large radiant input and output. This is mainly due to the following reasons: in the sub-tropics the Sun is often close to the zenith, absence or limited cloud coverage of deserts, and low water vapour content, and surface properties of deserts. Besides to that deserts have relatively very high surface albedo and thus considerable amount of incoming shortwave energy is reflected at the surface back to space. Moreover because of low evaporation rates from the dry surfaces of deserts and small thermal conductivity of sand, only a small fraction of the incoming solar energy is lost as non-radiative energy. The resulting high surface temperature of deserts arising from soil factors makes longwave emission very large.

The clear sky conditions let much of the longwave radiation escape. Therefore the net radiation absorbed by desert is not as large as one would expect rather it is less than that for bare soil in mid-latitudes in the same season (Oke, 1987). Figure 1.4 shows observed mean diurnal cycle of surface radiative shortwave, longwave and total flux averaged for all the AWS stations during summertime (JJA) in the year 2011.

Since latent heat is negligible over deserts, most of the excess radiant energy (approximately 90%) at the surface is converted into as sensible heat (heating the air or the soil) and a very small amount is converted to ground heat energy flux. The large convergence of surface sensible heat flux into the atmosphere during summer in the Sahara heat low results in deep atmospheric boundary layer (BL). On annual basis the ground conduction is zero (because net sub-surface storage must be zero). Based on zero net evaporation assumption, integrated over a one year period the net surface radiation is approximately equal to the sensible heat flux converged into the atmosphere.

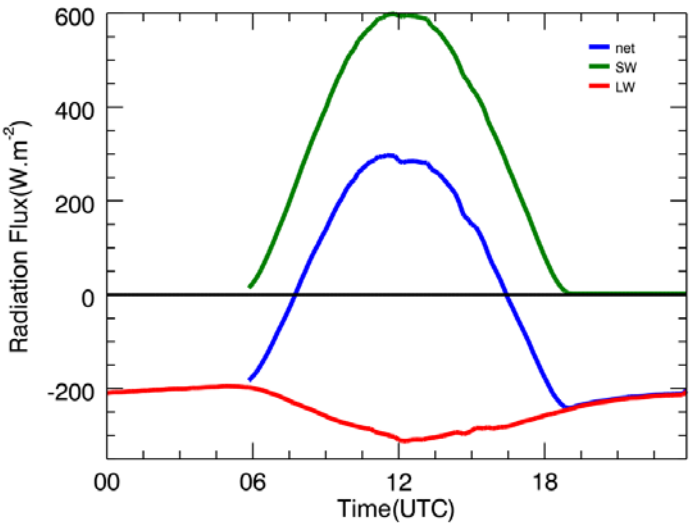

Figure 1.4 summertime (JJA, 2011) Mean Diurnal Surface radiative flux (Net: blue line, Shortwave: green line, and red: longwave) averaged for AWS stations

Diabatic heat which constitutes sensible heat, latent heat, and radiative energy is crucial part of Earth-Atmosphere interaction and driver of transport of mass and energy on the planet. On a global scale latent heat and radiative heat are dominant components of the diabatic heat while sensible heat is an important component of the heat budget in dry lands with high surface temperature. Diabatic heating is an elusive quantity to measure and climate models parameterize to derive it from horizontal and vertical heat advection (Bounoua and Krishnamurti, 1991;Chan and Nigam,

2009;Hagos and Zhang, 2010). In general low latitude regions have positive top of atmosphere radiation where the incoming solar radiation exceeds the outgoing infrared radiation opposed to high latitudes where there is a negative net top of atmosphere radiation with more outgoing than incoming. This is not always true particularly for deserts due to the reasons previously mentioned above, i.e. large surface albedo, transparent atmosphere, and insignificant latent heat releases, deserts may have net outgoing larger than the incoming making it a radiative deficit (Blake et al., 1983). Furthermore the presence of dust over desert surface significantly changes the radiative budget. For instance over the Sahara desert the net TOA radiative flux is weak or positive. Advection plays significant role in the redistribution of energy on a global scale. The relative importance of advective terms in transport of energy can be different depending on the location. For instance in extra tropical regions, horizontal advection is dominant means of heat transportation. During summertime the relatively large temperature gradient between the gulf of guinea and desert favours temperature and moisture advection into the SHL (Bounoua and Krishnamurti, 1991;Lavaysse et al., 2009;Peyrille and Lafore, 2007). This will be further investigated over the SHL region in this thesis.

1.2.2 Dynamics of Sahara Heat Low

The dynamics of the heat low region characterized by low level cyclonic and mid-level anticyclonic circulations (Racz and Smith, 1999). This basic structure is influenced by the configuration of topography and land-ocean boundaries resulting in a complex circulation pattern of horizontal temperature and moisture advection, with pronounced zonal and meridional gradients. The low pressure over the SHL (fig. 1.3) drives both the low level north easterly hot dry flow (harmattan) and the South westerly cool moist air monsoon flow (Lafore et al., 2010), converging along then Intertropical Discontinuity (ITD) to the south of the SHL (see fig. 1.1). The convergence of the two opposing low level flows, creates a strong baroclinic instability across the ITD leading to diverging flow at the mid tropospheric level. This diverging anticyclonic flow is responsible for the maintenance of mid-level African Easterly Jets (AEJ) (Thorncroft and Blackburn, 1999). Figure 1.5 displays a schematic of different components of summer time Saharan heat low circulation. The low level convergence followed by ascent and overturning divergent northerly wind near 700 hPa constitutes what is referred to as Saharan shallow meridional circulation (Shekhar and Boos, 2017). Another important feature of circulation over the Saharan region are African Easterly waves (AEWs) which are known to have influence on convection and thus rainfall in the

Sahel. They are also noted for being precursors to tropical cyclones in the tropical Atlantic and east Pacific Ocean basins (Thorncroft and Hodges, 2001). AEWs are commonly observed over latitudinal extent of 10^0 to 15^0 with characteristics wavelength of 2000 to 4000 km, period of 3 to 5 days, and westward propagation at speeds of 7 to 8 m s^{-1}. The AEW seasonal peak and migration is linked to the cycle of the AEJ. The mechanism by which AEWs initiate is still under active research although the instability of the AEJ is clearly a major factor. However the formation and evolution of AEWs is believed to be influenced by the topography in the Ethiopian highlands and Darfur mountains (Mekonnen et al., 2006) that can be described as a trough or cyclonic curvature maximum that develops on the AEJ.

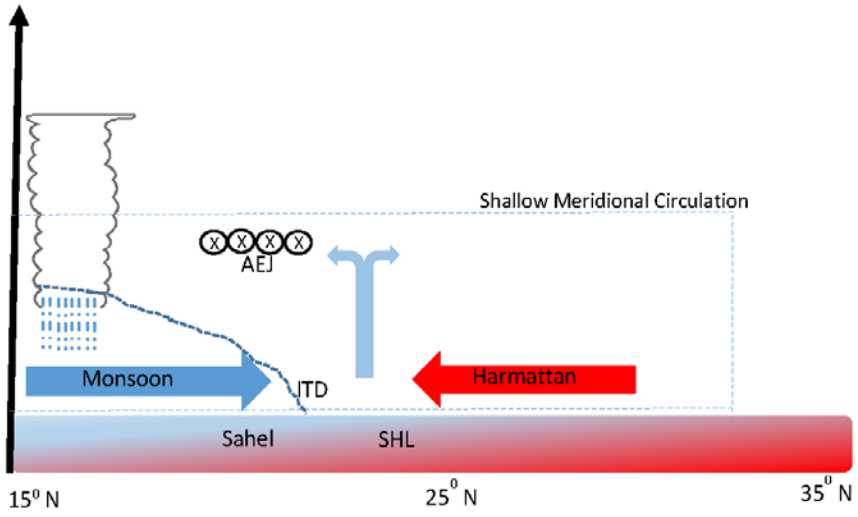

Figure 1.5 Schematic diagram representing the Saharan atmospheric Circulation. The blue arrow represent wet cold monsoon flow, and red arrow represent the dry hot harmattan flow and the thick blue dashed line represents the position of the inter tropical discontinuity (ITD)Rectangular box shown in dashed lines represent the Saharan shallow meridional circulation. The crosses inside circles show into page direction, which represents the African easterly jets.

1.2.3 Convective Density Currents (Cold pools)

The climate system of the Sahara heat low briefly described above shows that it is a result of different complex physical processes among which two pronounced processes are the summertime intensification of the Saharan heat low and subsequent monsoon flow advecting moist air towards the heart of the Sahara desert from the gulf of Guinea.

The moist air together with hot temperature of the Sahara boundary layer creates a favourable condition for the development of convection in the region. In the heart of the Sahara desert it is common that convective rain evaporates before reaching the ground due to the extreme large surface temperature.

Cold pools are formed when precipitation resulting from mesoscale convective cloud evaporates before reaching the ground (Charba, 1974;Simpson, 1969). Figure 1.6 illustrates the processes involved during the formation of convective triggered cold pools. The down drafting cold air creates a density current (Weisman and Rotunno, 2004) spreading out horizontally up to hundreds of kilometres from the source (Knippertz et al., 2009). The size and magnitude of cold pools vary ranging from intense microscale downdrafts with vertical velocity up to 15 m s^{-1} covering horizontally up to 1 km to synoptic or planetary subsidence with vertical velocity as small as cm s^{-1} (Lafore et al., 2016). Cold pools particularly large ones are commonly observed in low latitude arid regions pertaining to their optimal conditions. The two dominant sources for cold pool downdrafts in the Sahara are convection from the monsoon flow and Atlas Mountains which will be further investigated in Chapter V. The high speed air arising as a result of the density difference between the moist cold pool air and the hot surrounding atmospheric air can emit wall of dust referred locally as 'haboob' (Allen et al., 2013;Heinold et al., 2013;Karam et al., 2014). As the cold pool expands, it can lift

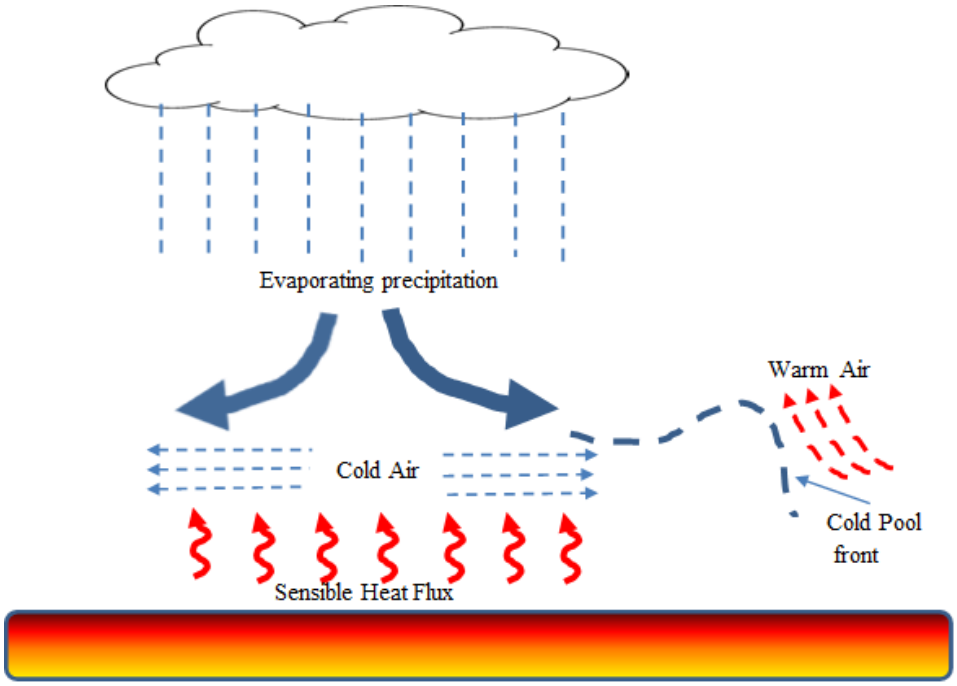

Figure 1.6 Schematic showing formation of cold pool

the surrounding warm air (fig 1.6) and thus creating condition for the development of new convective cells which can lead to formation of multi-cell thunderstorms as a

consequence (Tompkins, 2001;Weisman and Klemp, 1982). Studies show cold pools play key role in the organization of deep convection (Tompkins, 2001;Weisman and Rotunno, 2004).

1.3 Roles of Dust and Water vapour on the radiation budget of Saharan Heat Low

Dust is known for its radiative effect making it important actor in controlling the energy budget of the Saharan heat low region. The radiative effect of dust comes from absorption, scattering, and emission of solar and teresterial radiation shortwave radiation (Balkanski et al., 2007; Haywood et al., 2005; Sokolik et al., 2001; Tegen, 2003) emitted by both the atmosphere and Earth's surface. Dust confined within the mixed layer has a warming effect on the atmosphere primarily due to its absorption of shortwave radiation (Ackerman and Cox 1982). This could increase the top of atmosphere net incoming radiation. For instance the long mean (1979-2015) JJA net top of atmosphere radiation at the Saharan heat low region derived using ERA-I data is 26 W m^{-2}. It is also understood that dust has net cooling effect at the surface and warming above the dust layer (Tegen and Lacis, 1996). In addition to its direct radiative effect, dust is known to have indirect radiative effect by serving ice nuclei (IN) (Hoose & Mohler, 2012) altering the microphysics of cloud (Seinfeld et al., 2016)

During summer time moisture is transported dominantly from the monsoon flow and further deep in to the desert by cold pools (Garcia-Carreras et al., 2013;Marsham et al., 2013a). Though debatable, it is recently indicated that greenhouse effect of water vapour is responsible for the intensification of the SHL. But there is a clear positive trend in the moisture level within the Sahara desert. It is well understood that water vapour, along with carbon dioxide and ozone, is the most important radiatively active greenhouse gas of the Earth's atmosphere which has longwave cooling effect in the troposphere. Water vapour molecules also absorb solar radiation resulting in heating of the troposphere. However the longwave effect of water vapour is dominant over its shortwave effect with a net effect being cooling of the troposphere. In the Sahara heat low, in addition to dust, water vapour has also dominant role in controlling the radiative budget of a region (Evan et al., 2015;Marsham et al., 2016).

1.4 Literature Review

The Saharan heat low is a region of immense research interest to scholars around the globe with active research going on to answer the existing questions in relation to its climate variability and associated impact on the initiation and intensity of monsoon flow and precipitation in the Sahel. Here I present previous research works relevant to the research questions I would like to address in this thesis.

Recent studies show desert amplification, that is strongest near surface warming observed in the arid regions (Cook & Vizy, 2015; Wei et al., 2017). Large downward longwave radiation is believed to be driver for near surface warming which in turn in is strongly correlated with increased water vapour over deserts (Cook & Vizy, 2015; Evan, Fiedler, et al., 2015; Wei et al., 2017). In agreement with this Sahara desert has been detected to have surface warming of 2 – 4 times greater than that of the tropical mean temperature (Cook and Vizy, 2015). In line with this, intensification of the Saharan heat low is implicated with recovery of Sahelian rain fall. There are two suggestions for intensification of SHL: (i) warming due to increased water vapour in the SHL (Evan et al., 2015;Zhou, 2016) and (ii) warming due to increased greenhouse gases(Cook and Vizy, 2015;Dong and Sutton, 2015) resulting in warming of the African continent and thus enhancing land-sea thermal contrast. However it is consistently proposed that the surface warming in the SHL is a result of the increased downward longwave radiation despite what it might caused it. Most previous studies prove that intensification of the SHL leads to increased Sahel rainfall. Stronger Saharan circulation (shallow meridonal circulation) as a result of the intensification of the SHL is attributed to the increase in Sahel precipitation (Martin and Thorncroft, 2014). Others argue that the changes in Sahel precipitation to be associated with changes in sea surface temperature (SST), (Hagos and Cook, 2008;Roehrig et al., 2013). A more recent work (Shekhar and Boos, 2017) suggested that stronger shallow meridonal circulation weakens Sahel rainfall. They further attributed anomalies in SST and surface albedo for ultimate cause for the changes in Sahel precipitation. The above studies suggest the SHL still needs further investigation so that a consensus can be arrived in relation to the causes of variability to and its influence on Sahel precipitation.

PART I (Heat and moisture budget of SHL)

The SHL experiences strong temperature and moisture advection (termed ‘ventilation’ by (Chou et al., 2001) around its peripheries. Notably, maritime air from the Eastern Atlantic at the western SHL boundary, from the Mediterranean on the northeastern boundary and from the monsoon at the southern boundary. These circulations have a strong diurnal cycles and intra-seasonal variability e.g. Parker et al.

(2005), Grams et al. (2010), Todd et al. (2013), and Marsham et al. (2013b). Previous studies have investigated the heat and moisture budget of the Saharan region and associated impact on intensity of the heat low at various time scales. For instance an earlier work, Bounoua and Krishnamurti (1991) studied the thermodynamic energy and moisture budget for a five day wave over the Sahara desert. They showed the contribution of horizontal and vertical advection is removing heat from the surface layer. During their period of study they also showed that water vapour is supplied via horizontal advection from the monsoon region. Lavaysse et al. (2009) used temperature tendency equation to investigate the process controlling the displacement of SHL. They suggested the advective terms are less important in the seasonal displacement of SHL. However the decadal variability is not considered in their work. Further Evans et al. (2015), through heat and moisture budget analysis from 1979-2012, suggested that the intensification of the SHL to be associated with increased moisture advected from the monsoon flow which has also a positive feedback of further intensifying the SHL due to the greenhouse effect of water vapour. To investigate the year-to-year variability, Evan et al. (2015) considered ten warmest and ten coolest seasons. In a more recent work Martin et al., 2017 investigated the 3-D distribution of diabatic heating using CMIP5 over the North Africa region and studied its role on the West African Monsoon (WAM) circulations. However the contribution of mean and transient flows to the heat and moisture budget are not presented in previous works. The relative magnitude of these processes at various spatial/temporal scale remains to be resolved fully. Although climate model projections for the 21st century link changes in SHL intensity with Sahel precipitation (Biasutti et al., 2009), uncertainty in representation of the mean state of the SHL in models is high (Evan et al., 2014). Therefore, improved understanding the dynamics and thermodynamics of the SHL is required. I here investigate specifically the heat and moisture budget of the core heat low region and attribute the mean and transient flows to the total advection of heat and moisture. To see decadal variability, I will consider the composite three warmest and three coolest seasons and compare it with the long mean of moisture and heat budget. I extend this to investigate the variability of the SHL region and its association with diabatic heating of the region. To the best of our knowledge this has not been done previously. This will help understand the detailed process that make up SHL and its variability.

Part II Role of Dust and Water vapour in controlling radiative budget of SHL

During summertime, SHL is broadly co-located with the maximum dust aerosols location (Knippertz and Todd, 2012). Direct radiative effects of dust aerosol at the top of atmosphere and surface has been quantified from in situ observations and satellite data (Ansell et al., 2014; Banks and Brindley, 2013; Yang et al., 2009). There is still considerable uncertainty on the local radiative forcing of dust because it depends on many factors such as geometrical properties (size distribution), optical properties (composition), altitude of dust, and underlying surface albedo that collectively determine whether radiative effect of dust is cooling or warming (Haywood et al., 2005;Highwood et al., 2003;Muller et al., 2009;Petzold et al., 2009;Ryder et al., 2013b). In this thesis, I will present different experiments on the sensitivities of dust radiative effect to different parameters including size distributions and surface albedo. In a recent study water vapour is shown to have impact on the heat budget and thus intensity of the Sahara heat low region (Evan et al., 2015). Marsham et al. (2016) empirically derived variability in the DRE due to water vapour variations, and implicitly cloud, as well as dust. However, there remain important gaps in our understanding. First, there are substantial uncertainties in the magnitudes of radiative fluxes (and other heat budget terms) across both the various reanalyses and observations. Second, separating the radiative effects of water vapour from both its and associated clouds and from dust aerosol is challenging, given the strong co-variability of dust and total column water vapour anomalies in the Sahara associated with monsoon surges and resulting convective cold pool events (‘haboobs’) which transport water vapour and dust into the central Sahara (Garcia-Carreras et al., 2013; Marsham et al., 2008; Marsham et al., 2013b). As such, there is a need to quantify more fully the DRE of dust and water vapour, both independently and together, over the Sahara. This information is necessary to resolve the processes that govern the fundamental structure and maintenance and variability of the SHL. Addressing these research gaps is hindered by the acute shortage of routine observations in the region and large discrepancies between models and reanalyses (Evan et al., 2015a; Roberts et al., 2015).

Part III Convective density currents and their role in the SHL

Convection triggered density currents, which are ubiquitous features in the Sahara region, have been shown to play significant role in the advection of moisture to the heart of the Saharan desert (Marsham et al., 2013a, Redl et al., 2015) and emission and transport of dust (Allen et al., 2013;Heinold et al., 2013). Cold pools are also shown to influence the displacement of the ITD (Flamant et al., 2009). Despite their influence in the transport of moisture and dust with in the Sahara, the

characteristics of cold pools including their seasonal and spatial variation is under documented. Partly this is due to models lack of simulation of convection and partly due to lack of observational data. In order to better represent regional surface and boundary layer processes in models, and thus improve simulation of convection and related processes, it is essential to understand the characteristics of such convective triggered density currents. A number observational analysis has been made to characterise cold pools over different locations: in the United States (Engerer et al., 2008), in the southern Arabian Peninsula (Miller et al., 2008), in the southern foothills of the Atlas mountains (Emmel et al., 2010;Redl et al., 2015), and in Niger, Niamey (Provod et al., 2016). Previous studies in the region are limited to case studies focusing on few locations and shorter period. I would like to extend this to larger domain and relatively longer study period on the condition of data availability. Fennec AWS data provides an opportunity to make an in depth study on the properties of these common atmospheric processes over the central Sahara region. Here give a comprehensive description of the cold pool events using the FENNEC AWS station surface measurements of atmospheric variables. I further compare characteristics of selected cold pool events with MERRA re-analysis product and thus derive the associated error arising due to lack of resolving these mesoscale processes in models.

1.5 This thesis

The physical processes by which the SHL develops and is maintained are not fully understood, not least due to the relative lack of observations in this remote region. Given that SHL is changing I need to understand it better if I are to improve prediction of future climate. This research is necessary for the following two key reasons.

1. Sahara heat low is believed to play key role in the onset and development of the West African Monsoon (WAM) and the livelihood of millions of people inhabitant in the Sahel are dependent upon the monsoon rain. Therefore understanding the detailed processes involved in the Saharan heat low is thus vital to better understand associated impact and long-time variability of the WAM.
2. Sahara desert is the largest source of dust aerosol which is known to impact the climate system through its interaction with radiation on both regional and global scale. Recently it has been shown that dust has significant role in controlling the intensity of the Saharan heat low. Nevertheless climate impact of atmospheric aerosols in general and dust in particular is still poorly represented in climate models. Radiative forcing of aerosols is one of the major sources of uncertainty

in IPCC reports. Uncertainty of dust aerosol in driving the variability of radiative energy in the region still remains high in the region.

Driven by the above two important reasons, this research attempts to address three important questions which are clearly stated below. The big picture of this research is to provide a comprehensive analysis of the different components of climate system of the SHL which are crucial for its development and maintenance. Here I attempt to answer the following three questions which are the main objective of this research:

1. What processes are responsible for formation, maintenance, and large scale variability of SHL? To answer this question I provide a comprehensive analysis of the SHL heat and moisture budgets from reanalysis data and thus determine the important processes responsible for its structure and maintenance. The 3D spatial distributions of the long term mean heat and moisture budget will be analyzed. I will establish degree of uncertainty in heat budget estimates by comparisons across a range of available reanalysis products. Further I aim to quantify inter-annual variability in the SHL intensity and the associated heat budgets to determine the drivers of such variability. By answering the above research question I will be able to determine the relative importance of each advective terms in the maintenance of the Saharan heat low region.
2. The first research question leads us to further investigate the role of dust and water vapour in controlling the heat budget of the heat low region and thus my second research question: How important are water vapour and dust in controlling variability of heat budget of the Saharan heat low?
3. It is well understood climate models misrepresent the amount of dust and moisture in the atmosphere. The third and last research question I address in this thesis is: What are the characteristics and how frequent are convective triggered cold pool outflows in transporting of moisture in the Sahara heat low region? This will enable us to characterize mean features, distribution and frequency of cold pools in the remote central Sahara. I will also provide bias of climate models in resolving these processes and the resulting error in the amount of moisture in the region.

The detailed explanation of the methodology implemented to carry out the specific research objectives mentioned above and the required dataset are presented in chapter II. Each research question is addressed in Chapters III, IV, and V. Additional information on the methods and data used are also provided in Chapters III, IV, and V.

CHAPTER II

2 Data and Methods

2.1 Introduction

This research work aims to improve our understanding of the key processes involved in the maintenance and variability of the SHL. Specifically I investigate mean state and the variability of heat and moisture budget of the SHL during summertime, the roles of water vapour and dust in controlling the energy budget of the SHL, and the contribution of the mesoscale convective activities in transporting of water vapour into the SHL. To this end I use different dataset sources: model output, satellite observations, and ground measurements. In this chapter I provide complete list of datasets used and description of the methodology I implement. Additional information on the data used are also provided in each chapter.

2.2 Data

2.2.1 In-situ Observations

The Fennec project has produced a detailed observational data set in the scarcely observed remote locations of the Sahara desert during 2011 and 2012 (Washington et al., 2012). The project comprises of aircraft and ground based observations of meteorological dataset. A total of 20 aircraft flights were conducted during 2011 and 2012, where on board in-situ instruments measured meteorological fields, radiation flux, and quantities related to cloud and aerosol properties. A detailed instrumentation and flight patterns can be found in (Ryder et al., 2015). The ground based data includes measurements made during the intensive observation period (IOP) at two sites, SS1 at BBM, Southern Algeria (Marsham et al., 2013b), and SS2 at Zouerate, central Mauritania (Todd et al., 2013) and network of automatic weather stations (AWS) spread over Sahara (Hobby et al., 2013). Fennec AWS data available for 2011 and 2012 which constitutes a network of eight stations installed across the Sahara desert providing measurements of atmospheric variables including temperature, moisture, pressure, wind speed and direction, shortwave and longwave flux. Detailed description of the FENNEC AWS is provided in (Hobby et al., 2013).

The AErosol RObotic NETwork (AERONET) is a global network of ground based photometers which provides aerosol optical, micro-physical and radiative properties. We use data from a particular station located at Bordj Badji Mokhtar (BBM). The CIMEL Electronique CE-318 radiometer is implemented to make automatic tracking of the sun with a 1.2^0 field of view width (Holben et al., 1998). AOD measurements are made every 15 minutes at multiple channels from UV to IR (340nm, 380nm, 440nm, 500nm, 675nm, 870nm, 940nm, and 1020nm) for three quality data levels. For this study I use the Level-2 data at BBM which is cloud screened and quality assured data. Since dust AOD at 550nm is not available for june 2011, I derive it from AOD at 500 using the relation:

$$\alpha = \frac{log\frac{\tau_{\lambda_1}}{\tau_{\lambda_2}}}{log\frac{\lambda_1}{\lambda_2}} \tag{2.1}$$

where α is angustum exponent $\tau_{\lambda_1}$and $\tau_{\lambda_2}$are optical depths at wavelengths $\lambda_1$and $\lambda_2$respectively.

2.2.2 Reanalysis

Reanalysis is systematic approach through which climate model output is combined with observation data (data assimilation) that produce outputs with better representation of the state of the atmosphere. In spite of limitations and biases (Roberts et al., 2015), reanalysis products are useful component of the earth system science giving the opportunity to better understand the physical processes and variability on various temporal and spatial scales of the global climate system. There are many reanalysis outputs available for research purpose. Here I use data from three widely used reanalysis products, namely the European Centre for Medium-Range Weather Forecasts (ECMWF) Interim Reanalysis (ERA-I, Dee et al. (2011)), the National Centre for Environmental Prediction Reanalysis 2 (NCEP II, Kanamitsu et al. (2002)), and Modern-Era Retrospective analysis for Research and Application (MERRA, Rienecker et al. (2011)). The specific atmospheric and surface variables data used which are appropriate for each of my research questions are provided in chapters II - IV.

2.2.3 Satellite

Satellite observation has increasingly become an integral part of climate monitoring, hazard warning, and research. Instruments carried aboard satellites collect useful data of the state and composition of the atmosphere. In this research work, I use various satellite measurements of radiation and dust profile. Here I present a brief description of the satellite instruments, measurements of which I use in this research. More information on the specific measurements that I use are provided in the relevant chapters.

2.2.3.1 CERES

The Cloud and the Earth Radiant Energy System (CERES) provides measurement of top of atmosphere radiation budget. The CERES instruments carried aboard the National Aeronautics and Space Administration (NASA) Aqua satellite have three channels for radiance measurements: total channel (0.4 to 200μm), shortwave channel (0.4 to 4.5μm), and narrow thermal infrared channel (8.1 to 11.8μm). Since there is no longwave-only channel on CERES, daytime longwave radiances are determined from the difference between the total and shortwave channel radiances. For this research I use The CERES Level-3 SSF1deg_Hour TERRA footprint gridded data (CERES - footprint) instantaneous which has twice daily measurements with 1.0^0 resolution. In addition energy balanced and filled (EBAF) data is provided that spatially interpolates and files non-observed regions where the global net TOA flux is constrained to ocean heat storage term (Loeb et al., 2009).

2.2.3.2 GERB

The Geostationary Earth Radiation Budget (GERB) is one of the instruments along with SEVIRI telescopes aboard the Meteosat Second Generation (MSG) satellite in a geostationary orbit. The GERB instrument, which is aimed at carrying out atmospheric physics and meteorology researches, measures total emitted and surface reflected radiances over the Earth area as seen by MSG with a nominal resolution at nadir of 50 km and temporal sampling of 5 minutes. GERB level 2 products of Averaged Rectified Geolocated (ARG) fluxes at approximately 17 minute time and 50

km spatial (at nadir) resolution, with spectral ranges 0.32 to 4μm in the shortwave and 4 to 100 μm in the longwave (Harries et al., 2005). GERB does not provide a separate channel for longwave measurements. It is rather calculated as difference of total radiance and shortwave radiance measurements.

2.2.3.3 SEVIRI

The Spinning and Enhanced Visible and Infra-Red Imager (SEVIRI), aboard the Meteosat Second Generation (MSG) satellite orbiting in a geostationary orbit located at 3.5^0 W over the equator, provides observations every 15 min at a horizontal resolution 3X3 km at nadir (Schmetz et al., 2002). The SEVIRI instrument measures radiances at 11 spectral channels covering the visible and IR spectra between 0.6 - 3.4 μm and one high resolution visible (HVR) channel. A highlight of dust in the atmosphere is produced by combination of three brightness temperatures at 8.7 μm, 10.8μm, and 12 μm which is then applied to red-green-blue imagery. (Brindley et al., 2012) provided assessment of SEVIRI thermal infrared red-green-blue imagery to identify dust events. Due to the different spectral behaviours images of atmospheric particles, clouds, and surface characteristics in the above wavelength appear as different colours. In SEVIRI imagery Cold, thick high-level cloud appears in red, mid-level cloud in green, high moisture at low levels in blue and dust in pink (the more intense the emission, the brighter the pink). The signature of dust in SEVIRI is complicated by a number of factors such as; high water vapour (the largest influence), a strong near surface temperature inversion, the height of the dust layer, characteristics of the underlying surface (emissivity), mineralogical composition of dust, and the size distribution of particles (Brindley et al., 2012). An important advantage of this method using the IR spectrum is ability to detect dust emission at night. However the resulting changes in thermal emissivity of surface and atmospheric dust due to change in temperature at night makes the images complicated and difficult to interpret (Banks and Brindley, 2013).

2.2.3.4 CALIOP

The Cloud Aerosol Lidar with Orthogonal Polarization (CALIOP) is an active lidar instrument that gives quasi-insatantaneous view of the vertical structure and properties of cloud and aerosol. CALIOP is the main instrument on the Cloud Aerosol LIDAR Infrared Pathfinder Satellite Observations (CALIPSO) satellite, which is one of the Afternoon Constellation of Earth observing satellites in sun synchronous orbit,

providing observations for advanced studies on clouds and aerosols. CALIOP sends a frequency doubled simultaneous laser pulses down through the atmosphere and collects and measures the light that is backscattered from the laser pulse. Aerosol backscatter and extinction coefficient are measured at the wavelengths 532 and 1064 nm respectively (Vaughan et al., 2004;Winker et al., 2009) overpassing the Sahara twice a day at night and day (at ~01:30 and 13:30 local time) and gives global coverage in 16 days. The Calipso lidar level 3 aerosol data produces optical properties of aerosols on uniform spatial grid at altitudes below 12km. In this study I used dust vertical extinction profile. Details on production of vertical profiles of dust extinction I used are presented in Chapter IV.

2.3 Methodology

Detailed descriptions of methods implemented to answer each research questions are presented separately in chapters III, IV, and V. I present here a brief summary of the methodology.

The mean position of the SHL during JJA season is determined using the method of (Lavaysse et al., 2009) based on low level atmospheric thickness (LLAT): the difference in geopotential height between the 700 hPa and 925 hPa levels. Heat and moisture budgets are derived from thermodynamic energy equation (Chan and Nigam, 2009) and continuity equation (Trenberth and Guillemot, 1995;Wu, 1993) respectively.

The radiative effect of dust and water vapour are determined through simulations of radiative transfer model. It is a common practice using radiative transfer codes to study radiative effects of atmospheric gaseous molecules and particles. Radiative transfer codes can be run integrated with climate models or offline as stand alone models. When integrated within climate models, inputs required for radiative transfer calculations are provided from land surface and atmosphere modules while in stand-alone simulations inputs are provided externally. Here I use fennec observations complemented by reanalysis outputs to carry out radiative transfer calculations.. For this research I use SOCRATES (Suite Of Community Radiative Transfer codes based on Edwards and Slingo) model (Edwards and Slingo, 1996;Randles et al., 2013). Detailed description of SOCRATES and the experiments conducted to quantify the radiative effect of dust and water vapour are provided in Chapter IV.

Arrival of cold pool is typically associated with gust of air carrying moisture and lowering the surrounding temperature as a consequence. Changes in wind speed and humidity are therefore used as primary selection criteria for cold pool events. I develop a unique method for detection of cold pools using specific threshold of changes in atmospheric variables complemented with satellite imagery. That is once cold pools are identified by the magnitude of change in wind speed and moisture, they will be further confirmed against satellite imagery for possible nearby signs of dust and/or deep convection. Details of the algorithm used in the identification of cold pools is presented in chapter IV.

CHAPTER III

3 Heat and Moisture Budget of the Saharan Heat Low

(The main results of this chapter are in review for Publication)

3.1 Introduction

The Saharan Heat Low extends over a vast sector the central Sahara, is known for its unique extreme features: high surface temperature (or equivalently low surface pressure) with little or no precipitation and being largest source of dust on the planet. It is a key component of the West African Climate System. Over the annual cycle the SHL core migrates from a position south of the Darfur mountains (centred on ~6N, 20E) in winter to central western Sahara (centred on ~23N,3W) in summer(fig. 1.3), when it covers much of northern Mauritania, Mali and Niger and Southern Algeria and is characterized by extremely high surface temperature (Lavaysse et al., 2009;Messager et al., 2010b) and thick PBL, often extending up to ~4 to 5 km (Marsham et al., 2013b).

During summertime, SHL is broadly co-located with the maximum dust aerosols location (fig. 1.3) (Knippertz and Todd, 2012). The large-scale cyclonic low level circulation into the SHL includes the summer West African Monsoon (WAM) flow such that variability in SHL intensity modulates moisture transport and convective activity within the WAM (Lavaysse et al, 2010). As such the SHL has been implicated in WAM variability across a range of timescales, including (i) the synoptic (Couvreaux et al., 2009; Chauvin et al., 2010) to intraseasonal (Parker et al, 2005) (ii) mean seasonal (Thorncroft and Blackburn 1999; Sultan and Janicot, 2003; Peyrillé and Lafore 2007; Xue et al., 2010) (iii) Inter-annual and decadal through to future climate change in the WAM (Martin et al., 2014; Martin and Thorncroft 2014). Although climate model projections for the 21st century link changes in SHL intensity with Sahel precipitation (Biasutti et al., 2009) uncertainty in representation of the mean state of the SHL in models is high (Evan et al., 2014). Therefore, improved understanding of dynamics and thermodynamics of the SHL is required.

The physical processes by which the SHL develops and is maintained are not fully understood, not least due to the relative lack of observations in this remote region. The most comprehensive set of observations come from the recent field campaign ‘Fennec: The Saharan climate system’ (Washington et al, 2012) which is providing new

insights into the SHL radiation budget (Banks et al., 2014;Marsham et al., 2016) and processes within the SHL core (Engelstaedter et al., 2015).

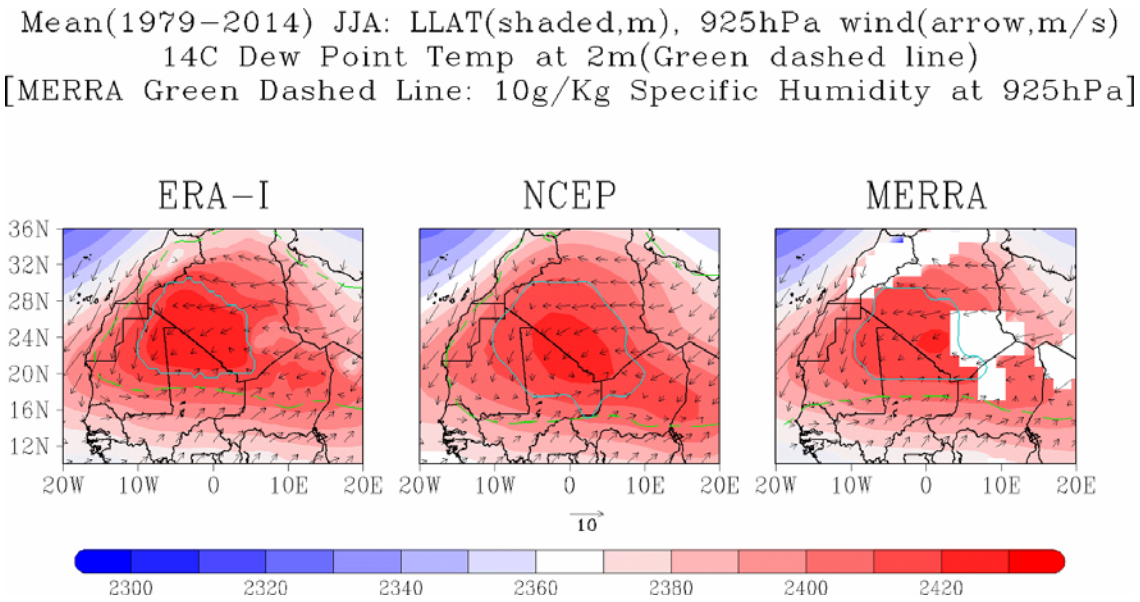

Figure 3.1 Climatology of SHL from ERA-I (left), NCEP (middle) and MERRA (right) re-analyses for 1979-2014. Mean JJA low level atmospheric thickness (LLAT) (m, shaded), 925 hpa winds and 2m 14 ^{0}C dew point temperature (green dashed line, for MERRA 10g/kg 925 hPa specific humidity). SHL core heat low region (cyan line, see methods for explanation)

Radiation budget over the Saharan heat low region plays a key role in controlling the dynamics of the region. The net balance of shortwave and longwave radiative fluxes at the top of atmosphere, within the atmosphere and at the surface are modulated primarily by clouds, dust aerosols and water vapour (Banks et al., 2014;Marsham et al., 2016;Yang et al., 2009). TOA net radiation is generally weakly positive in the summer months, +26 W m^{-2} for JJA averaged over SHL (+26 W m^{-2} for June 2011 and 2012, Marsham et al., 2016). At the surface the large net radiation surplus, 76 W m^{-2} for JJA averaged over SHL (~100 W m^{-2}, Marsham et al. (2016)) in summertime is converted to sensible heat, which controls the development and evolution of the mixed layer. Driven by net surface radiation, SHF shows seasonal variability with maximum SHF observed during summer, average JJA net sensible heat flux is ~68 W m^{-2}. The Saharan boundary layer, which is primarily controlled by convergence of surface SHF, exhibits a strong diurnal (Marsham et al., 2013b;Todd et al., 2013) and seasonal variability (Cuesta et al., 2008). During summer time convective boundary layer is formed in the daytime primarily driven by solar heating

which becomes fully developed in the afternoon, typically reaching depths of ~4 km and on some days when the SHL is intense up to 5 km (Marsham et al, 2013b) based on data from the Fennec supersite 1.

The dynamics of the heat low region characterized by low level cyclonic circulation and mid-level anticyclonic circulations (Racz and Smith, 1999). This basic structure is influenced bytopographic configuration and land-ocean boundaries resulting in a complex circulation pattern of horizontal temperature and moisture advection, with pronounced zonal and meridional gradients. The low pressure over the SHL drives both the low level North-easterly hot dry flow (harmattan) and the South-westerly cool moist air monsoon flow (Lafore et al., 2010), converging along the ITD to the south of the SHL (fig. 3.1). The SHL experiences strong temperature and moisture advection (termed 'ventilation' by Chou et al. (2001)) around its peripheries. Notably, maritime air from the Eastern Atlantic at the western SHL boundary (Grams et al., 2010), from the Mediterranean on the northeastern boundary (Lavaysse et al., 2010b;Vizy and Cook, 2009) and from the monsoon at the southern boundary (Parker et al., 2005;Sultan et al., 2003). These circulations have a strong diurnal cycles and intra-seasonal variability (Grams et al 2009; Marsham et al., 2013; Parker et al., 2005; Todd et al., 2013). Vertical advective heating through the descending Hadley cell branch may also be important. The relative magnitude of these processes at various spatial/temporal scale remains to be resolved fully.

Others have documented variability in the SHL and associations with the WAM at timescales from the synoptic (Bounoua and Krishnamurti, 1991) to intraseasonal (Chauvin et al., 2010;Roehrig et al., 2013), through to long terms decadal (Evan et al., 2015). Evan et al. (2015) suggested that the intensification of the SHL to be associated with increased moisture advected from the monsoon flow which has also a positive feedback of further intensifying the SHL due to the greenhouse effect of water vapour. In a more recent work Martin et al., 2017 investigated the 3-D distribution of diabatic heating using CMIP5 over the North Africa region and studied its role on the WAM circulations. Despite presenting the different components of diabatic heating (eddy flux convergence, radiative heating, and latent heating), they haven't provided the mean and transient advective processes which will effectively transport and balance the extra heating from diabatic source. There still remains a gap in our understanding particularly inter-annual variability and it is not known processes driving SHL variability at these timescales.

The main objective of this chapter is to provide a comprehensive analysis of the SHL heat and moisture budgets from reanalysis data and thus determine the important processes responsible for its structure and maintenance. The 3D spatial distributions of

the long term mean heat and moisture budget will be analysed. I derive the different advective terms resulting from the mean and transient flows (deviations from the mean) responsible for the transport of temperature and moisture and determine the relative importance of each term in the heat budget of the SHL, from which I derive the diabatic heating as a residual. I extend this to investigate the variability of the SHL region and its association with diabatic heating of the region. I establish degree of uncertainty in heat budget estimates by comparisons across a range of available reanalysis products. Further I aim to quantify inter-annual variability in the SHL intensity and the associated heat budgets to determine the drivers of such variability. To the best of my knowledge this hasn't been done previously. The chapter is composed of 4 sections. In section 3.2 a description datasets used and the methodology are presented. The results of my SHL heat budget analysis are presented in Section 3.3 covering both the mean state and analysis of variability. A discussion of the results and conclusions are provided in Section 3.4.

3.2 Datasets and Methodology

3.2.1 Data

Heat and moisture budgets are derived using data from reanalysis products for the common period 1979-2014. For comparison I use three widely used reanalyses, namely the European Centre for Medium-Range Weather Forecasts (ECMWF) Interim Reanalysis (ERA-I, Dee et al. (2011)), the National Centre for Environmental Prediction Reanalysis 2 (NCEP II, Kanamitsu et al. (2002)), and Modern-Era Retrospective analysis for Research and Application (MERRA, Rienecker et al. (2011)). Horizontal resolutions are 0.5^0X0.5^0, 1.25^0X1.25^0, and 2.5X2.5^0 for ERA-I, MERRA, and NCEP respectively. I use data on standard pressure levels, with ERA-I and MERRA available on 23 pressure levels up to 200 hPa and NCEP on 10 levels. I ignore the lowest levels below what is the approximate mean surface pressure over the SHL core region: ~965 hPa in reanalyses and in observations at Bordj Badj Mokthar (21.4N, 0.9E, elevation 400m a.m.s.l., Marsham et al. (2013b)), the synoptic weather station closest to the SHL core. I use temperature and wind fields to derive the heat budget terms in Eq. 2.3. I also use satellite measurements of TOA radiation from CERES monthly mean Energy Balanced and Filled (EBAF) product at 1-degree resolution (Loeb et al., 2009). Unless stated, results presented are calculated using ERA-I dataset.

3.2.2 Definition and location of the Saharan Heat Low

The location of the heat low is determined using the method of (Lavaysse et al., 2009) based on low level atmospheric thickness (LLAT): the difference in geopotential height between the 700 hPa and 925 hPa levels. The heat-induced dilation of Low Level atmospheric Thickness (LLAT) between the P_1=925 hPa and P_2= 700 hPa pressure levels can be expressed mathematically by combining the equation of state and hydrostatic balance as:

$$LLAT = \frac{R}{G}\int_{p1}^{p2} T\, d\big(ln(p)\big) \tag{3.1}$$

where R is universal gas constant, g is acceleration due to gravity, T is temperature and P is pressure. The LLAT varies depending on the heat contained within of the lower atmosphere and thus is a good indicator of presence of heat low. The long term (1979-2014) mean field of LLAT is derived (from the 06:00 slot only), and the core heat low area is defined as the region of highest LLAT, specifically the upper decile of LLAT over the domain 10^0 - 36^0N, 20^0E -20^0 W. The reason for using the 06:00 time slot only for derivation of the heat low location is to avoid other perturbations which are not directly associated with the formation of the heat low (Lavaysse et al., 2009). Figure 3.1 displays the long term (1979-2014) mean position of the core heat low region (inside the cyan line). SHL is defined as the upper decile of LLAT over the domain 10^0 - 36^0N, 20^0E -20^0 W. This SHL core region is centred on the Mali-Algeria border region in all reanalysis datasets but the centre of gravity is slightly further northwest (close to the triple point of Mauritania, Mali and Algeria at ~25^0 N, 5^0 W) in ERA-I relative to NCEP (~23^0 N, 1^0 E) and MERRA (~23^0 N, 0^0 E).

Inter-annual variability of heat and moisture budget is examined based on samples of composite of three strongest (warmest) and three weakest (coolest) SHL summer periods. Each of the strongest and weakest SHL years constitute 10% of the study period. Composite analysis is a standard technique in climate science commonly practised to study variability. For instance (Evan, Flamant, et al., 2015) considered ten warmest and ten coolest years to study the cause of warming trend in SHL. Here I use three years for each extreme case to maximize the signal causing the changes. I use time series of LLAT to identify three warmest and three coolest years. I use student t-test to measure statistical significance of differences between weak and strong heat low periods. From the time series of SHL LLAT (fig. 3.2), there is considerable agreement between the different reanalyses on what are the weakest SHL years but less agreement in the strongest years. Here I consider three common weakest SHL

years (1984, 1986, and 1992) and strongest SHL years (2002, 2010, and 2012) among the three reanalysis. There is a significant positive trend in LLAT in MERRA (0.3 m year^{-1}) and NCEP (0.3 m year^{-1}) assessed in (Evan et al., 2015) but less pronounced in ERA-I (0.2 m year^{-1}). The positive trends evidence of the intensification (warming) of the SHL also suggested by recent works (Cook and Vizy, 2015; Evan et al., 2015; Wei et al., 2017).

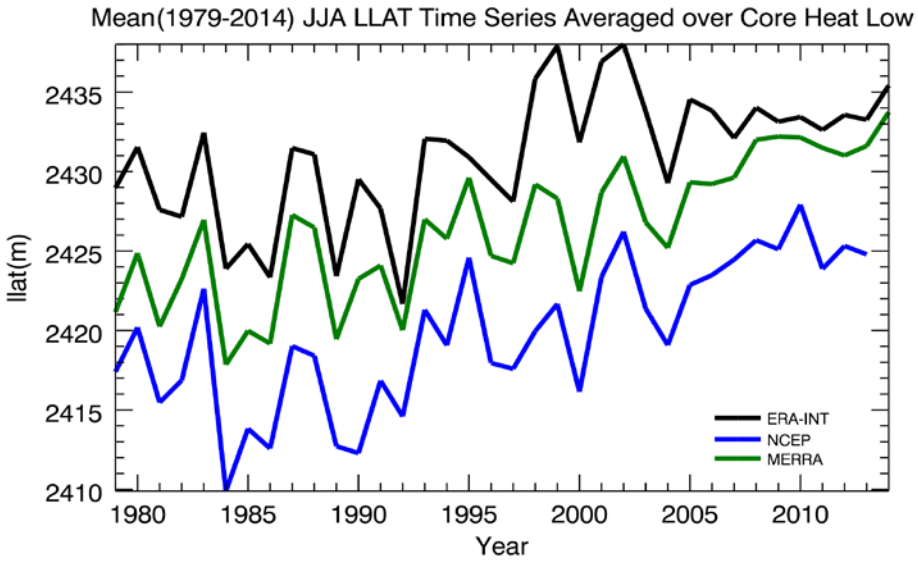

Figure 3.2 Time Series of LLAT averaged over the core SHL region (Region inside the cyan line in Fig. 1) during JJA

3.2.3 Derivation of heat and moisture budget

The different tendency terms in heat budget are derived from the thermodynamic energy equation (Chan and Nigam, 2009):

$$\frac{\partial T}{\partial t} = -\acute{v} \cdot \nabla \acute{T} - \acute{\omega}\left(\frac{p}{p_0}\right)^{\kappa}\left(\frac{\partial \acute{\theta}}{\partial p}\right) - \nabla \cdot (v'T') - \left(\frac{p}{p_0}\right)^{\kappa}\frac{\partial}{\partial p}\left(\omega'\theta'\right) + Q \qquad (3.2)$$

where is Q the diabatic heating rate, T is temperature, V is horizontal wind velocity, ω is vertical velocity, P is pressure, θ is potential temperature, $\kappa = \frac{R_d}{C_p}$ where R_d is gas constant, C_p is specific heat at constant pressure, and ∇ is the horizontal gradient operator. The primed quantities represent deviations from the monthly mean values and over bars show monthly mean. The local temperature tendency is calculated as the difference between 6 hour (or 3 hourly depending on data availability) interval of the

re-analysis data. The horizontal advection terms are calculated using centred difference method. The vertical derivatives at a given pressure level of mean and transient vertical temperature advection (2nd and 5th terms respectively on right hand side of eq. 3.2) are made by first calculating the mean of each variable between two pressure levels and then taking the difference.

The term on the left hand side of eq. 3.2 is the local temperature tendency. On the right hand side the first term is the monthly mean horizontal temperature advection term; the second term represents the mean vertical temperature advection (adiabatic heating and vertical advection); the fifth term is diabatic heating (derived as a residual) and the third and fourth terms are the transient horizontal and vertical advection respectively resulting from deviations from the monthly mean.

Diabatic heating rate that includes the shortwave and longwave radiative heating, latent heating, and sensible heat flux (SHF) transported from the surface into the boundary layer through turbulence is derived as a residual from eq. 3.2. I estimate the temperature tendency due to turbulent component of diabatic heating ($\frac{\partial T_{SH}}{\partial t}$) by converting the reanalysis surface SHF into a heating rate in K day^{-1} using:

$$\frac{\partial T_{SH}}{\partial t} = \left(\frac{g}{C_p}\right)\frac{\Delta F_{SH}}{\Delta P} \tag{3.3}$$

where ΔF_{SH} is the convergence of sensible heat flux in a given pressure layer ΔP. We approximate the sensible heat flux to be distributed uniformly through the depth of the PBL. Over the SHL in summer, I assume net latent heating to be negligible, although there is still differential heating rates through the atmosphere due to the unbalanced heating and cooling rates of evaporation and condensation at different vertical levels. The long mean JJA latent heat flux at the surface over the core heat low region is less than 3 W m^{-2} compared to the sensible heat flux of over 60 W m^{-2} supporting the assumptions made above. If 3 W m^{-2} latent heat from the surface is distributed uniformly through the lowest 200 hPa pressure levels, results in atmospheric heating rate of ~0.1 K day^{-1}. A similar approach is also implemented in the calculation of heat budget over the Arabian heat low (Blake et al., 1983; Smith, 1986). Based on these assumptions we are left with only one unknown quantity, the radiative heating rate, which is evaluated as residual from the diabatic heating rate diagnosed using equation 3.2 and the estimated sensible heating rate. At levels above the PBL top I assume all diabatic heating to be radiative.

Moisture budget is derived from continuity (Trenberth and Guillemot, 1995;Wu, 1993) given by:

$$\frac{\partial \acute{q}}{\partial t} = -\acute{v} \cdot \nabla \acute{q} - \acute{\omega} \frac{\partial \acute{q}}{\partial p} - \nabla \cdot \left(\acute{q}' v'\right) - \frac{\partial}{\partial t}\left(q' \acute{\omega}'\right) + (E - C) \qquad (3.4)$$

where q is specific humidity, E is evaporation, and C is condensation. The definition of primed and overbar quantities is similar to the definitions given in eq. 3.2. The left hand side of eq. 3.4 represents the tendency of moisture. On the right hand side of eq. 3.4 the first and second terms represent the rate of advection of moisture by mean horizontal and vertical flows respectively while the third and fourth terms represent the rate of moisture advection by transient horizontal and vertical flows respectively. The last term on the right hand side of equation 2 represents the rate of change of moisture from physical processes (evaporation and condensation). Similar procedures are used for the vertical and horizontal derivatives as in heat budget calculations.

The heat and moisture budgets are derived for each summer month and then averaged over the individual years and all data (1979-2014) to obtain the long term climatological mean. The diurnal cycle in the low level circulation and radiative fluxes is pronounced over the Sahara so that I need to ensure the mean diurnal cycle actually contributes to the mean advective not the transient components. To this end I derive the monthly heat/moisture budgets separately for each time step and then average the resulting quantities. For long time mean conditions, (Section 3.3) I present results averaged over the peak SHL season of JJA. In considering inter-annual variation (Section 3.4) I consider the longer spring-summer season AMJJA as I seek to explain differences in the evolution of the SHL and in particular the temperature tendency term, which is close to zero over JJA. For moisture budget calculations, the mean flow and transient flow horizontal advection of moisture are considered. Vertical advection of moisture is small since the extreme hot conditions of the SHL, the net vertical transport of moisture due to evaporation and precipitation is negligibly small, and therefore horizontal advection of moisture is the dominant factor that brings water vapor into the heat low region, vertical moisture advection is not treated here (Evan et al., 2015). Heat and moisture budgets are unavailable in the publically accessible reanalyses output(with exception to MERRA), and thus I developed codes using Interactive Data Language (IDL) to derive each term in equations 3.2 and 3.4.

3.3 Results of Heat and moisture budget analysis over SHL

The fundamental structure of the long term mean summertime SHL heat and moisture budgets is common between the various reanalysis products although the

magnitudes of heating/drying rates varies considerably. Over the Sahara the net balance of shortwave and longwave radiative fluxes at the top of atmosphere, within the atmosphere and at the surface are modulated primarily by clouds, dust aerosols, water vapour and surface albedo (Banks et al., 2014;Marsham et al., 2016;Yang et al., 2009). TOA net radiation is generally weakly positive in the summer months 26 (16, 15) $W.m^{-2}$ for JJA averaged over SHL from ERAI, (NCEP and MERRA). This makes the SHL a weak net heat sink. At the surface the large net radiation surplus 76 (33, 69) W m^{-2} in summertime is largely converted to sensible heat ~68 (19, 60) W m^{-2} which controls the development of the PBL. Atmospheric radiative convergence i.e. the difference in net radiation between the TOA and surface is -50 (-17, -53) W m^{-2} such that the atmosphere as a whole experiences cooling, balanced of course by the sensible heat flux from the surface. I used the CERES Edition 2.8 energy balanced and filled top of atmosphere flux (Loeb et al., 2009) to compare with reanalysis TOA flux. The 16 year (2000-2015) climatological (JJA) averages of all-sky TOA fluxes over the core of heat low (7^0W-4^0E, 20^0N-28^0N) is 13 W m^{-2}. The TOA net flux is overestimated in ERA-I compared to NCEP and MERRA which both have closer agreement with CERES observation. There is a wide range of differences in the surface and TOA radiative flux and sensible heat flux among reanalyses products. Note that NCEP surface radiative and sensible heat fluxes are under half those of the other reanalyses. This difference could be due to differences in model physics (cloud representation), surface properties, and importantly data assimilation, however it needs a further investigation to clearly identify the reason for the discrepancy.

The differences in heat and moisture budget among the three reanalyses products is presented below. I have already pointed out position of the core heat low is determined using the thickness of the geopotential height between 925 hPa and 700 hPa. This layer has a typical representative of the heat contained in the heat low region (Lavaysse et al., 2009) and thus I discuss here vertically averaged diabatic heating rate between 925 hPa and 700 hPa. Figure 3.3 displays the mean 1979 - 2014, summertime (JJA) diabatic heating rate vertically averaged between 925 hPa and 700 hPa for the three reanalysis products and their mean. There is a distinction in the heating rate (notably in ERA-I) north of ITD mainly from convergence of turbulent heat flux into the atmosphere and south of ITD from release of latent heat associated with monsoon rainfall. In all the three reanalysis products there is a stronger diabatic heating (up to ~2 K Day^{-1}) which is centered to the west of the core heat low (fig. 3.3). In the lowest levels diabatic heating is primarily controlled by convergence of sensible heat flux which is relatively smaller in the core heat low area. Maximum JJA mean sensible heat flux is located over the borders of North and Northwest Africa (not

shown). Weaker Vertical temperature gradient in the deep mixed boundary layer of central Sahara and smaller surface wind speed, which affect magnitude of sensible

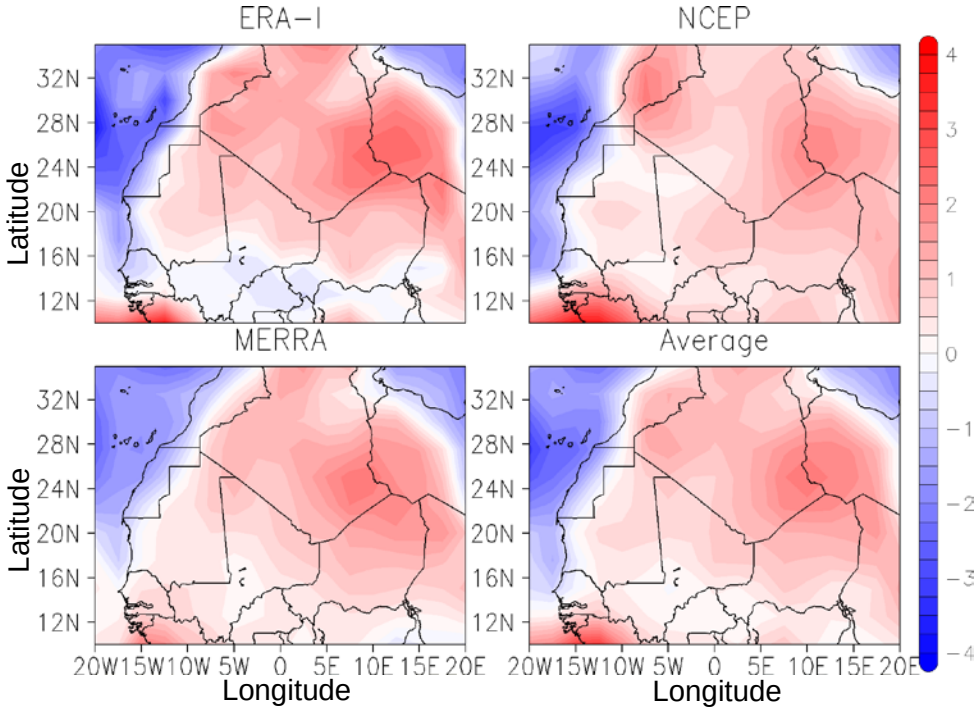

Figure 3.3 Diabatic Heating Rate (K Day^{-1}) vertically averaged between 925 and 700 hPa for JJA, 1979 - 2014. Top plots: left-ERA-I, right-NCEP and bottom plots: left-MERRA, and Right-mean of all

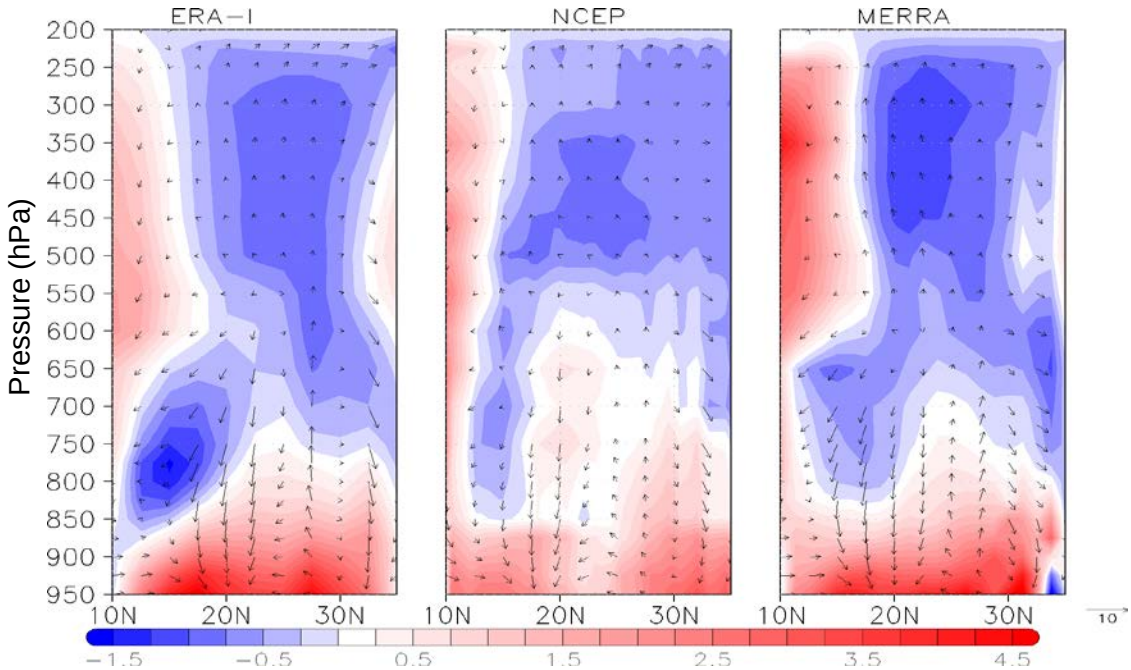

Figure 3.4 Zonal average (10W-5E) Vertical Profile of long mean (1979-2014) diabatic heating (shade) and Hadley Circulation (arrow),[zonal mean(10W-5E) meridional wind (m.s^{-1}) and vertical wind times 100 (m.s^{-1})]

heat flux convergence into the atmosphere, are possible reasons for the smaller sensible heat flux in the SHL core. Near the surface the strong diabatic heating is partly cancelled by the radiative cooling. In the layer between 925 hPa and 700 hPa, radiative cooling is relatively smaller and thus heating is primarily controlled by sensible heat flux. The strong diabatic heating rate of up to ~3 K Day^{-1} in the south west of the domain is from the latent heat release of convective rain from the Northern edge of the West African monsoon rainband (7^0N-12^0N). Meridional cross section of zonal averaged(10^0W-5^0E) vertical profile diabatic heating rate (fig. 3.4) shows this clearly, heating in the lower levels (~ 800 hPa) from convergence of sensible heat flux and cooling aloft due to radiative (longwave) emission. The heating up to ~4.5 K day^{-1} from deep convection in the WAM rainbandbetwee ~700 and 200 hPa is evident on the southern end of the domain (on left side of each plot, fig. 3.4). The main features of the vertical heating profile is similar among the three reanalyses despite their differences in the magnitude of heating (or cooling) rates. The radiative cooling dominates above the dry convective layer. NCEP has weaker heating rate with deeper dry convective layer compared with ERA-I and MERRA. A consistent result of the mean diabatic heating profile is given in (Martin et al., 2017), figure 5a.

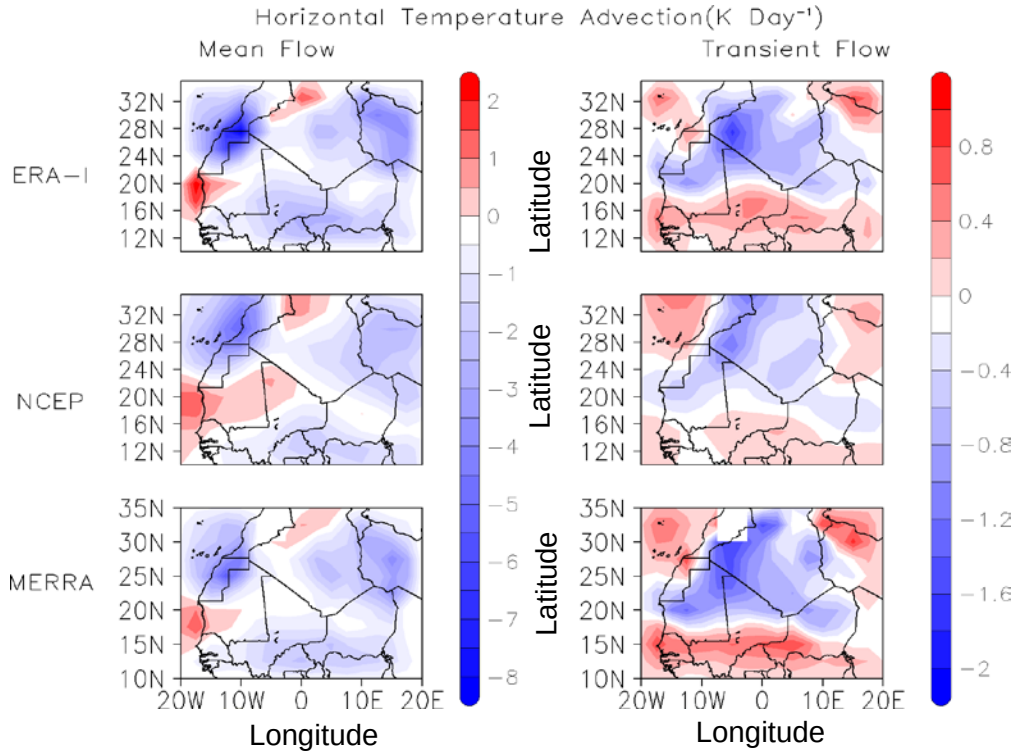

Figure 3.5 Horizontal Advection of Temperature (K Day^{-1}) from mean (left column) and transient (right column) circulations vertically averaged between 950 and 850 hPa for JJA, 1979-2015. Top plots: ERA-I, middle plots: NCEP and bottom plots: MERRA

The strong diabatic heating in the lower levels is primarily balanced by cold advection from the surrounding areas. The low level convergence flow extends from surface to ~850 hPa and thus I use this layer to present the results of temperature advection over my domain (fig. 3.5). The spatial structure of horizontal low level temperature advection over the wider North-West Africa indicates that ventilation by the mean circulation, which includes the mean diurnal cycle that occur primarily around the peripheries of the SHL core region. Specifically, in order of magnitude, the Atlantic inflow (Grams et al, 2011; Todd et al., 2013) at the western boundary of the SHL (locally ~-8 K day^{-1}), advection from the Mediterranean at northeastern boundary (diverted around the northern flank of the Hoggar massif) (locally ~-3 K Day^{-1}), and the monsoon flow along the southern boundary (locally ~-3 K day^{-1}). This ventilation by the mean circulation is primarily a nocturnal phenomenon associated with the deep inland penetration of the nocturnal low level jets (LLJs) in the Atlantic inflow (Grams et al, 2011), harmattan and monsoon circulations (Schepanski et al., 2017). The SHL core is co-located with a minimum in ventilation by the mean horizontal circulation. Horizontal transient flows cool the core heat low region by up to 2 K day^{-1}. On the whole domain, the transient flows appear to oppose the cooling from the advection of temperature due to mean horizontal wind flows. However as one might expect, the magnitude of the heating rate from the transient horizontal flows is small compared to that of the mean horizontal wind. Once more the three reanalyses have captured the main picture of advective heating/cooling over the region.

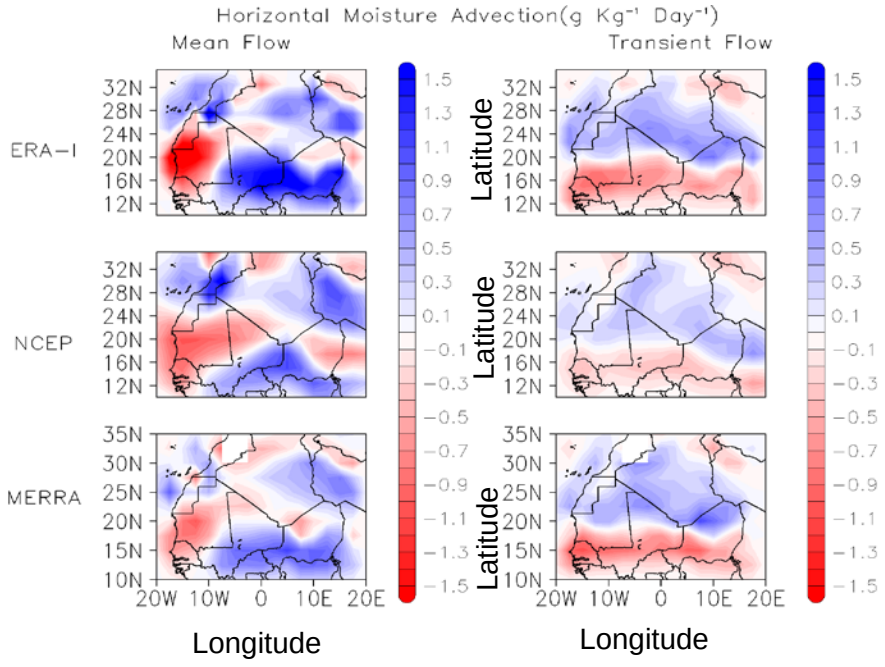

Figure 3.6 Similar to Figure 3.5 except for moisture advection (g Kg^{-1} Day^{-1}). Blue shades represent moistening and red shades represent drying.

Consistent with the horizontal temperature advection results (fig. 3.5), there is net moistening of SHL from the surrounding peripheries (fig. 3.6). The moisture advection from the monsoon flow is relatively stronger in ERA-I (up to 1.5 g Kg^{-1} Day^{-1}) compared with NCEP and MERRA (~1.0 g Kg^{-1} Day^{-1}). Central heat low region is moistened by up to 0.7 g Kg^{-1} Day^{-1} from the transient flows (left panel on fig. 3.6). There is meridional distinction in the moisture advection of transient flows with drying tendency up to -1 g Kg^{-1} Day^{-1} below 20^0 N and above ~30^0N and moistening of up to 1 g Kg^{-1} Day^{-1} the region between ~20^0N to ~30^0N. There is an agreement in the spatial representation of the moisture advection among the reanalyses. NCEP produced the smallest tendency compared with ERA-I and MERRA. Notably the contribution of moisture advection by the monsoon is stronger in ERA-I compared with NCEP and MERRA.

As my primary focus here is to investigate the processes taking place in the SHL core, I next present the vertical profile heating rates of the thermodynamic energy equation terms in Eq. 3.2. Figure 3.7 shows the heating rate terms averaged over the core heat low region (region inside the cyan line in fig. 3.1). The horizontal lines on the plots indicate variability (standard deviation) of the mean heat budget terms vertical profile. The main result in the vertical profile plots are low level cooling from horizontal mean and transient flows and vertical transient flow, warming from mean vertical flow. The diabatic heating derived as residual from E.q. 3.2 has two main structures. Heating primarily from dry convection extending from surface up to ~700 hPa and radiative cooling aloft. The structure of residual diabatic heating profile calculated by Martin et al., 2017(Figure 7g) over the Sahara (10W-10E, 20-30N) are consistent with what I found here.

The distinct vertical structure of horizontal wind divergence (not shown here) leads us to consider the heat budget profile as structured into three broad vertical sections with characteristic heating processes, namely lowest levels(950 – 850 hPa), mid-levels (850 – 600 hPa), and upper levels (600 – 200 hPa). The heat budget terms vertically integrated over these three levels are provided in Table 3.1, and 3.2. Overall, as the SHL is well established in JJA temperature tendencies over the JJA period are close to zero so that I am effectively concerned with quantifying various and opposing heating processes which maintain quasi equilibrium. There is agreement both in magnitude and structure of heating rate profile between ERA-I and MERRA in contrast to that of NCEP which shows notable difference particularly in the lower atmosphere below 600hPa (fig. 3.7). The advective heating rate terms in NCEP are under half of the respective terms in ERA-I or MERRA. NCEP data has 11 pressure levels up to 200 hPa compared with 23 pressure levels of ERA-I and MERRA. For this reason I do not

include vertically integrated heat and moisture budgets over the three vertical sections mentioned above. I thus present results of vertically averaged heat and moisture budget for ERA-I and in bracket MERRA.

(i) Lowest Levels (950-850 hPa)

On average the lower troposphere is cooled by a combination of all the advective terms but substantially by the horizontal rather than vertical terms. The mean horizontal component has the largest maximum, peaking at almost -1.3 K day^{-1} (-0.7 K day^{-1}) at 950 hPa for ERA-I (MERRA). When integrated over the lowest layers (950 to 850 hPa) the mean and transient horizontal components contribute at -0.9 K day^{-1} (-0.5 K day^{-1}) and -0.8 K day^{-1} (-1.0 K day^{-1}), respectively (Tables 3.1 and 3.2). Together the

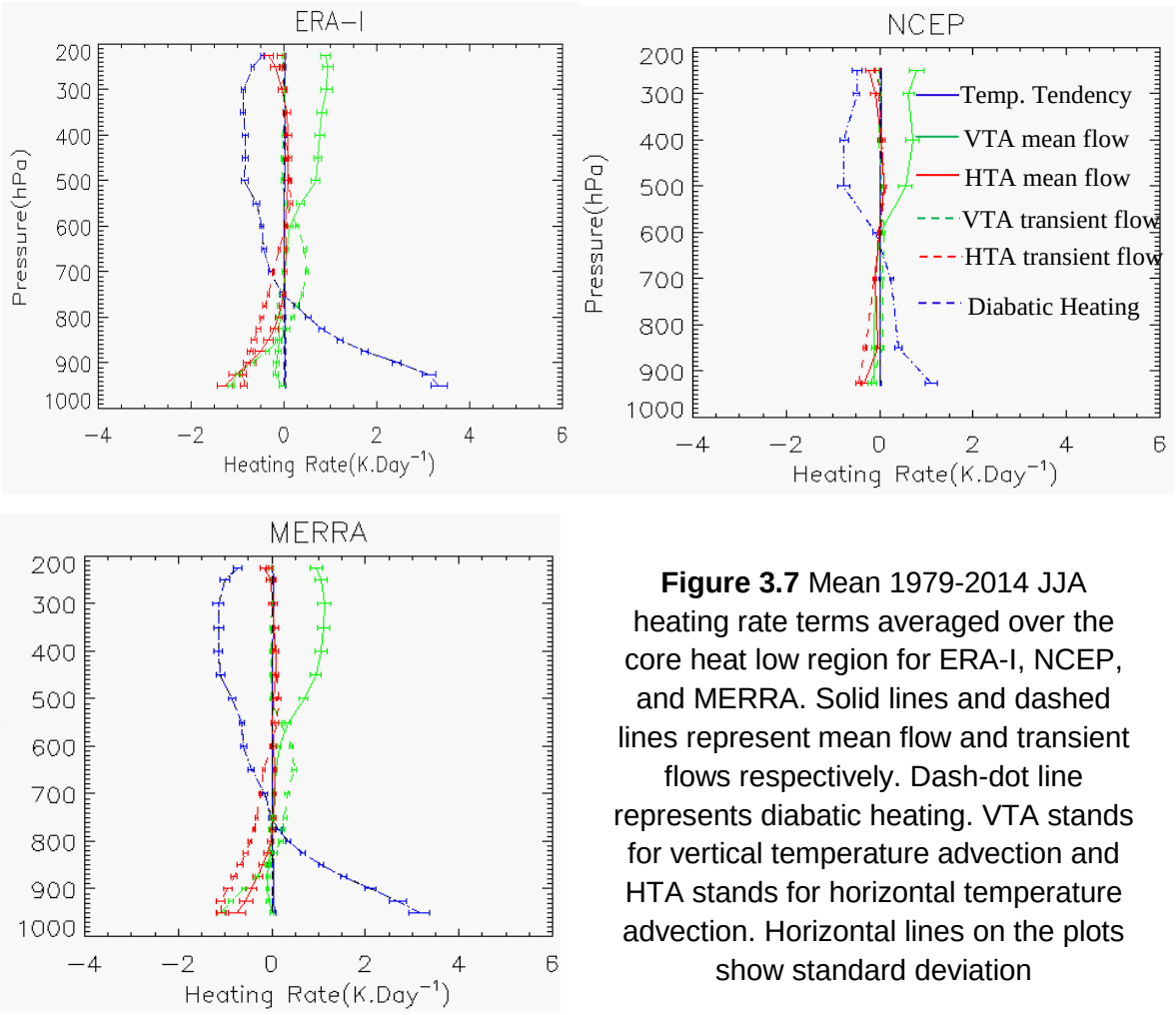

Figure 3.7 Mean 1979-2014 JJA heating rate terms averaged over the core heat low region for ERA-I, NCEP, and MERRA. Solid lines and dashed lines represent mean flow and transient flows respectively. Dash-dot line represents diabatic heating. VTA stands for vertical temperature advection and HTA stands for horizontal temperature advection. Horizontal lines on the plots show standard deviation

mean and transient horizontal advection drive a substantial ventilation of the SHL through the low level convergent circulation into the SHL described further below. Ventilation by horizontal transient component (fig. 3.5) is focussed over the core SHL

region itself (locally up to ~-2 K day^{-1}). Indeed, transients appear to warm the SHL peripheries suggesting that they act to weaken the mean circulation. The diurnal cycle in the transient term is far smaller than that for the mean term. Vertical temperature advection also act to cool the lower atmosphere over the SHL, notably the transient flow which cools to ~800 hpa at a peak rate of 1.1 K day^{-1} near the surface. Averaged over the lowest levels 950 to 850 hPa, the vertical transient flows contribute cooling of -0.8 K day^{-1} (-0.7 K day^{-1}). This suggests that transients invoke a net upward heat flux over the SHL. This occurs mostly at night (not shown). The mean vertical motion involves a marginal cooling of 0.1 K Day^{-1} (Table 3.1).

Mean Vertical profile wetting/drying rates are displayed in fig. 3.8. Once again the horizontal lines on the plots represent year to year variability (standard deviation) of moisture advection. As one would expect year to year variability in the upper atmosphere is smaller compared with the lower levels. Total horizontal moisture advection (fig. 3.8) shows substantial net moistening of lowest layers up to ~850 hPa (peaking at 0.8 g kg^{-1} day^{-1} (0.6 g kg^{-1} day^{-1}) for ERA-I (MERRA). Horizontal moisture advection from the transient flow is the dominant mechanism in the moistening of the lower levels over the core heat low region. There is a notable difference in the low level moisture advection rate from the mean flow among the three reanalyses products: moistening in ERA-I opposed to both NCEP and MERRA which have net drying when averaged over the core heat low region.

Table 3.1 Heating Rate (K Day^{-1}) for terms in equation 3.2 averaged over the core heat low 1979-2014 from ERA-I data. Vertical averaging is mass weighted mean for each layer considered.

Layer	period	VTA mean flow	HTA mean flow	VTA transt. flow	HTA transt. flow	diabtic heating
950-850	AMJJA	0.1	-1.3	-0.9	-0.9	3.1
	JJA	-0.1	-0.9	-0.8	-0.8	2.7
850-600	AMJJA	0.3	-0.2	0.4	-0.5	0.1
	JJA	-0.0	-0.1	0.3	-0.4	0.3
600-200	AMJJA	0.6	0.2	0.1	-0.1	-0.8
	JJA	0.7	0.0	0.1	0.0	-0.8
925-700	AMJJA	0.2	-0.6	0.0	-0.7	1.2
	JJA	-0.1	-0.3	-0.1	-0.6	1.1
950-200	AMJJA	0.4	-0.1	0.0	-0.3	0.0
	JJA	0.3	-0.1	0.0	-0.2	0.0

The low level cooling from horizontal and vertical advection is countered by diabatic warming up to 3.4 K day^{-1} (3.2 K day^{-1}) at the lowest level and 2.7 K day^{-1} (2.4 K day^{-1}) averaged from 950 to 850 hPa layer (Table 3.1 and Table 3.2). Diabatic heating acts to warm the SHL up to about 700 hPa and over this layer the sensible heat flux (1.95 K day^{-1} for ERA-I) exceeds total diabatic heating (1.34 K day^{-1} for ERA-I) such that there is a net radiative cooling to 700 hPa of 0.62 K day^{-1}. My estimates derived using distribution of sensible heat flux uniformly through the PBL are consistent with those directly obtained from MERRA reanalysis outputs (not shown). Horizontal temperature advection from mean flow in the lowest levels averaged over the months AMJJA becomes stronger, -1.3 K day^{-1} (-0.9 K day^{-1}) compared with that of JJA, -0.9 K day^{-1} (-0.5 K day^{-1}) showing on April and May there is strong advection. A possible reason for this could be during the later summer months (July and August) the SHL region will be established and the horizontal temperature gradient will be smaller and thus reducing mean horizontal temperature advection.

Table 3.2 Same as Table 3.1 except for MERRA data

Layer	period	VTA mean flow	HTA mean flow	VTA transt. flow	HTA transt. flow	diabtic heating
950-850	AMJJA	0.1	-0.9	-0.8	-1.0	2.8
	JJA	-0.1	-0.5	-0.7	-1.0	2.4
850-600	AMJJA	0.4	-0.1	0.3	-0.5	-0.0
	JJA	0.0	-0.0	0.2	-0.4	0.1
600-200	AMJJA	0.9	0.1	0.1	-0.0	-1.0
	JJA	0.9	0.0	0.1	0.1	-1.0
925-700	AMJJA	0.2	-0.4	-0.0	-0.7	0.9
	JJA	-0.0	-0.2	-0.1	-0.6	0.9
950-200	AMJJA	0.6	-0.1	0.0	-0.3	-0.2
	JJA	0.5	-0.1	0.0	-0.2	-0.1

(ii) Mid-level (~850-600 hPa)

In the mid troposphere between ~850 to ~600 hPa there is warming from vertical advection, primarily from transient flow, up to 0.6 K day^{-1}. As such transient vertical flow drives descent in this mid layer (and ascent in the lowest layers). This is offset by cooling from the diabatic component (presumably radiative, above 750 hPa). In the mid layer the role of horizontal advection declines rapidly. The mean moisture

tendency (fig. 3.8) show substantial net drying by the mean horizontal circulation, consistent with the vertical structure of convergent/divergent inflow/outflow. The drying from the transient flow is smaller in magnitude compared to the mean flow and starts at upper level ~750 hPa (~800 hPa) in ERA-I (MERRA). The vertical temperature advection from mean flow changes from 0.0 K day^{-1} in JJA to considerable warming of 0.4 K day^{-1} in AMJJA. This due to the adiabatic warming from surface to ~600 hPa during April and May will decrease which further becomes cooling later in summer.

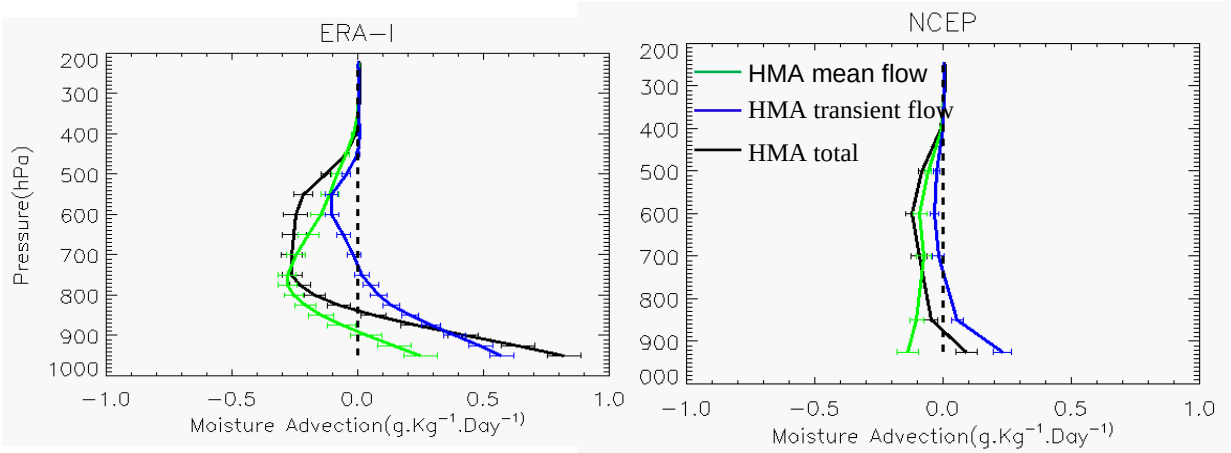

Figure 3.8 Mean 1979-2014 JJA moisture advection averaged over the core heat low region for ERA-I, NCEP, and MERRA. Blue, green, and black lines represent moisture advection tendency from mean flow, transient flow, and total respectively. HMA stands for horizontal moisture advection. Negative numbers show drying and positive numbers show moistening. Horizontal lines on plots show standard deviation

(iii) Upper level (~600-200 hPa)

Horizontal temperature advection plays little(or zero) role in this layer. In the upper troposphere above ~600 hPa to the first order there is a quasi-equilibrium between radiative cooling and warming from mean vertical advection (fig. 3.7), associated with mean subsidence in the descending limb of the Hadley circulation. It is interesting to note that the transient terms vanish above about 600 hPa justifying that there is insignificant variation from the mean flow in the upper part of the atmosphere.

Overall, the mean state atmosphere in the lower layers of SHL shows characteristics of a highly damped system in that there are strong opposing forces. The SHL itself drives a mean circulation which strongly cools the system, which is offset by turbulent transfer of sensible heat flux. As such the SHL caused by strong low level heating is essentially regulated by horizontal ventilation and radiative cooling processes. However the magnitude of the heat budget terms differs substantially between the three reanalyses products with NCEP values less than half those of the ERA-I and MERRA.

3.4 Inter-annual variability in the SHL and heat budget

Having presented the long mean state of the Saharan heat low, next I investigate the inter-annual variability based on heat budget and moisture budget. I have already shown that there is positive trend in LLAT (fig 3.2), and thus warming of the Saharan heat low region. The three weakest and three strongest years are not the same for the reanalyses products (fig 3.2). I have made test analysis of heat and moisture budget for different three weakest and three strongest years for each reanalyses and the results are consistent with those of common weak and strong years for all the reanalyses. Therefore, to be consistent, I use here the common weakest three years and common strongest three SHL years. Composites of LLAT time series for the three strong and weak years show the difference in SHL intensity between samples occurs primarily early in the summer season during May and June (fig. 3.9), and subsequently maintained through the summer season. During AMJJA the difference in mean LLAT between the weak and strong years is 8 m which is statistically significant with p value < 0.01. The distinction between the strong and weak heat low years is more evident starting from mid-june (fig. 3.9) after which heat low is fully developed. This pattern is consistent across all the observations in the two samples. The composite heat and moisture budget analysis for the weak and strong SHL years is presented (fig. 3.10, fig. 3.11, fig. 3.12, and fig. 3.13) over summer. The spring (April and May) period results are also used to identify the processes determining variability in SHL intensity. That is to understand the details of these processes in the SHL, I consider the tendency terms for each month in April to August. Over the earlier period (April to June) temperature tendency is non-zero reflecting inter-annual differences in temperature and thus LLAT.

There is a clear difference in the low level (950 hPa - 850 hPa) specific humidity between the strong and weak SHL periods (Figure 3.10). That is strong (weak) heat low years are moister (drier) by up to 2 g Kg^{-1} compared with the long mean (1979-2014). All reanalysis products consistently reproduce anomalous moistening (drying) of

central Sahara locally up to ~0.4 g Kg^{-1} (1.0 g Kg^{-1}) during the strong (weak). Monsoon flow has significant contribution to the increase in moisture which in turn is a result of the enhanced meridional circulation due to the high SHL temperature (Thorncroft et al., 2011) during the strong years. NCEP shows the strongest anomalous moisture both during the strong and the weak SHL periods while the differences between the two contrasting periods in ERA-I is not as pronounced. This is consistent with the weaker trend in LLAT in ERA-I have already shown in Figure 3.2. Regardless of the varying magnitude, the difference in moisture between strong and weak years is statistically

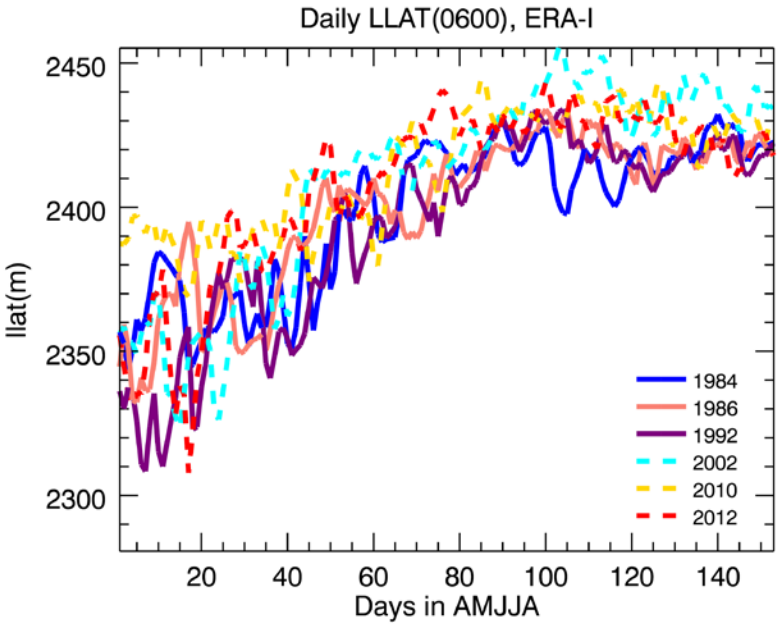

Figure 3.9 Daily LLAT over the summer season during strong and weak SHL years.

significant in all reanalyses output (p value < 0.01). There is no notable difference in low level diabatic heating between the strong and weak heat low years in the three reanalysis products (fig. 3.11). This consistent with the results of sensible heat and surface longwave flux discussed above. The diabatic heating difference between the strong and weak heat low years is slightly larger in NCEP compared with ERA-I and MERRA. Despite the smaller magnitudes of heating/moistening rates calculated so far with NCEP fields, it has a better representation of variability in heat and moisture budget. This is clearly seen in the moisture difference between the contrasting years and to a lesser extent but consistent in diabatic heating. ERA-I has weak signals in capturing the differences in moisture and heat budget between the two contrasting periods. The disparity in the magnitude diabatic heating among the reanalyses could be because of differences in the core dynamical processes and way in which data is assimilated and differences in models simulation of these prognostic variables.

In spite of the strong heat low period being hotter by up to 3 K compared with the weak years, there is small difference (up to ~1 W m^{-2}) in sensible heat flux between the two extreme conditions of the SHL(Table 3.3). Additional analysis is required to estimate warming of the atmosphere due to increased sensible heat flux however from the above results it can be suggested that feedback of increased sensible heat flux due to the warming of the SHL is too small to be detect in reanalyses calculations. It is also important to note that there could be bias in calculation of sensible heat flux in

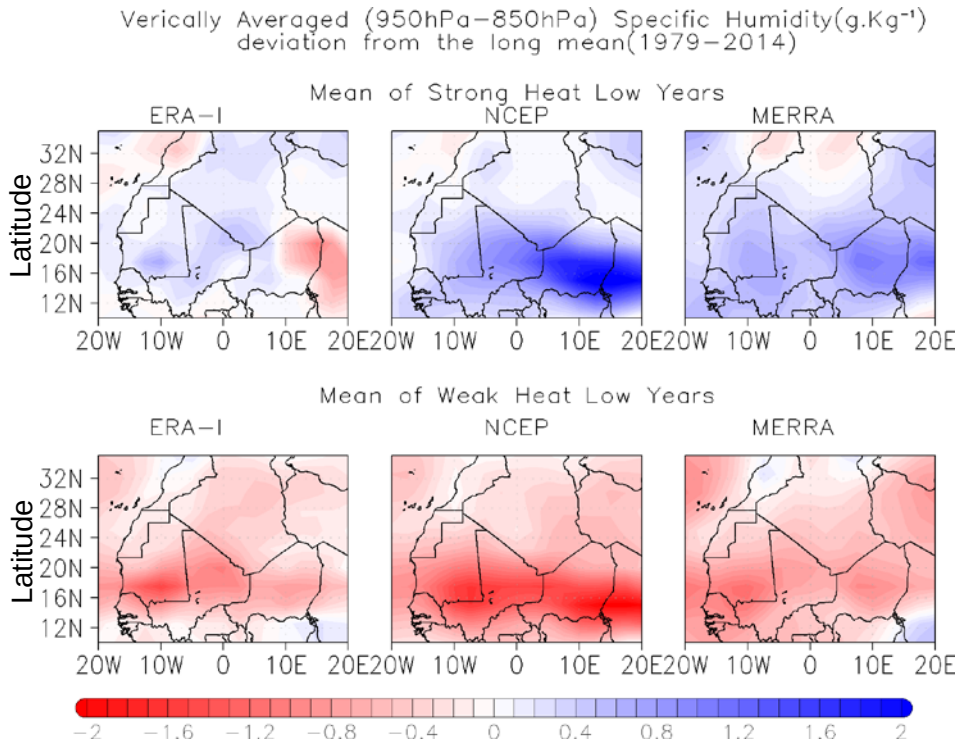

Figure 3.10 Figure 3.12 Mean JJA vertically averaged specific humidity (g Kg^{-1}) (950 hPa - 850 hPa) difference, q (mean strong years) minus q (long mean, 1979-2014): top plots and difference, q (mean weak years) minus q (long mean, 1979-2014): bottom plots, Left: ERA-I, Middle: NCEP, and Right: MERRA

reanalyses. Further reinforcing the above results, time series of 1979-2014 mean JJA net surface longwave flux averaged over SHL region (not shown) does not reveal any notable increase during the strong heat low years compared with the weak heat low years. This is in contrast to the findings of Evan, Flamant, et al. (2015) that suggest strong change in net surface longwave flux in the range 1.0 - 3.0 W m^{-2} as a result of increase in a kg m^{-2} column integrated moisture in the atmosphere. However Evan et al., 2015 results are for the period from 2001 to 2010 calculated at night-time hours

only during which the longwave flux forcing is strongest. The disparity between the magnitudes of sensible heat flux between reanalyses results (Table 3.3) are large.

The vertical profile of tendency terms for composites of strong and weak SHL years is shown in figs. 3.12, 3.13, and 3.14. The time May to June is the period when the temperature tendency term is positive and relatively larger while during July to August, temperature tendency is close to zero. The reason for very small temperature tendency during the peak JJA period is because the heat low is already established during the late spring time (see the inter-annual differences in LLAT) such that after this there is no further intensification rather it is maintained before it starts weakening after August. Therefore, the change in temperature during JJA is effectively close to zero in both strong and weak SHL composites. This makes it difficult to see the difference in temperature tendency between the composite weak and composite strong SHL years.

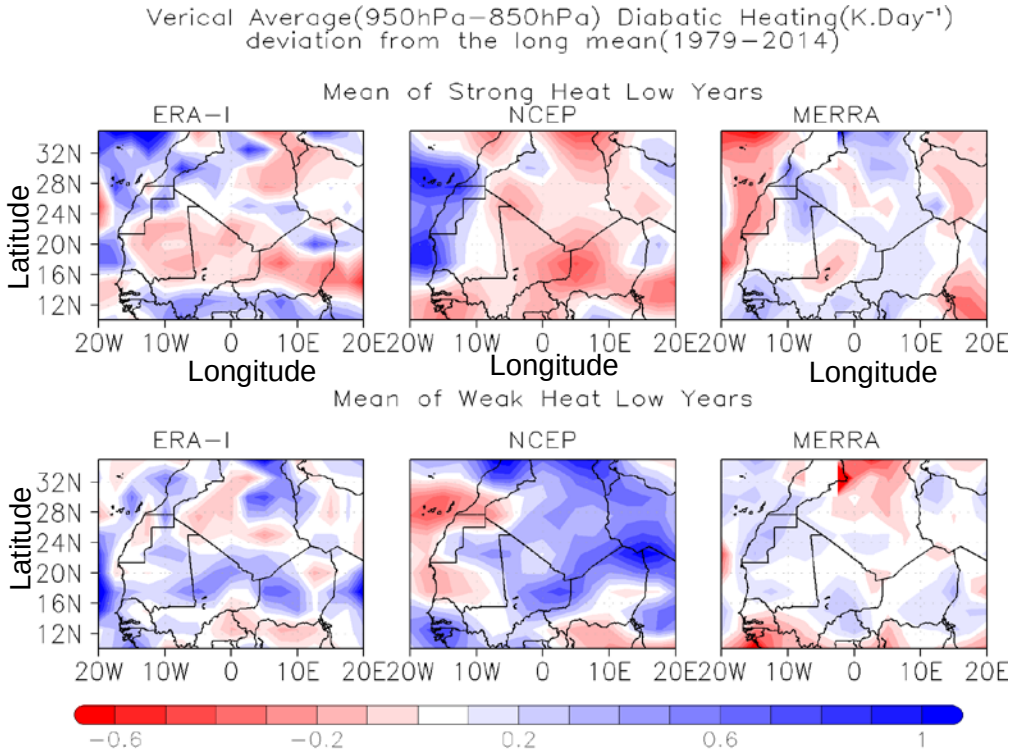

Figure 3.11 Same as Figure 3.10 except for diabatic heating (K day^{-1})

TABLE 3.3 JJA skin temperature (SKT) and sensible heat flux (SHF) averaged for weak and strong heat low years.

	Weak Heat Low Years mean			**Strong Heat Low Years mean**		
	ERA-I	**NCEP**	**MERRA**	**ERA-I**	**NCEP**	**MERRA**
SKT (K)	310	303	312	312	306	313
SHF(W m^{-2})	58	23	62	59	21	61

The tendency terms from advection, notably from the horizontal component, has a relatively bigger difference between the two contrasting periods. The weak years have stronger low level mean JJA advective cooling from the mean circulation than the strong years -1.6 K day^{-1} (-1.3 K day^{-1}) and -1.2 K day^{-1} (-0.8 K day^{-1}) respectively for ERA-I(MERRA) in the lowest level.On average despite the stronger low level circulation during the strong years, horizontal advection is smaller compared with results of the weak years. This can be understood by noting that horizontal advection is a product of wind and change in temperature and advection by itself would lead to temperature differences of about - 30 K (40 K) in ERA-I (MERRA) over the ~100 day spring-summer period. The actual difference in temperature tendency in the SHL layer between the composites is ~1 - 2 K. The transient horizontal flow has less but opposing effect to the mean flow in the lower levels, less cooling during the weak years. The stronger advective cooling in weak SHL is substantially compensated by the combined effects of, in decreasing order of importance, stronger warming from the mean vertical circulation (perhaps directly resulting from the greater horizontal convergence), weaker transient horizontal cooling and slightly greater diabatic heating (figs. 3.12 - 3.14). In general horizontal temperature advection from the mean flow is strongest during the months April to June after which its magnitude starts declining. It is also in this particular time (April to June) the difference between mean horizontal temperature advection between strong and weak years is notable. This difference is smaller during the months July and August.

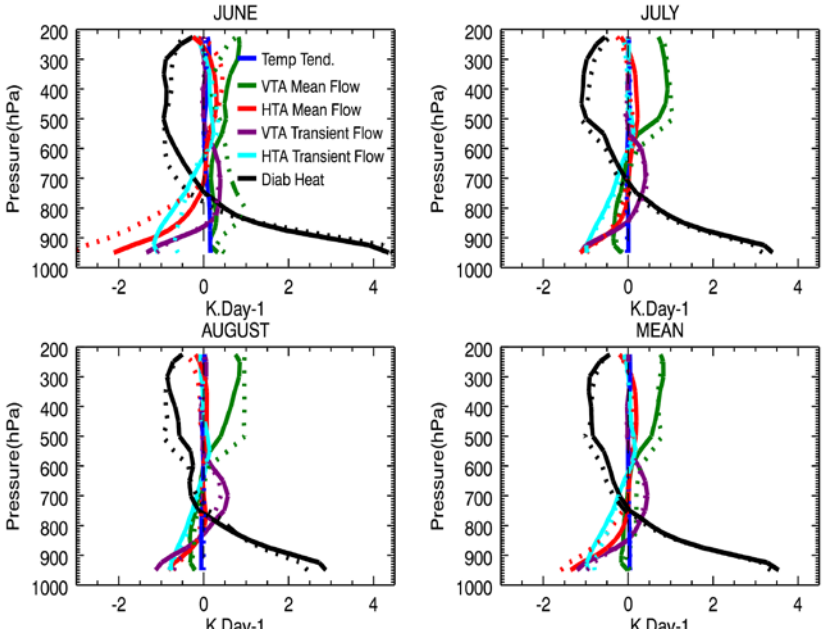

Figure 3.12 Mean temperature advection and diabatic heating rates (K Day^{-1}) for the weak SHL years (dashed lines) and strong SHL years (solid lines) from ERA-I data.

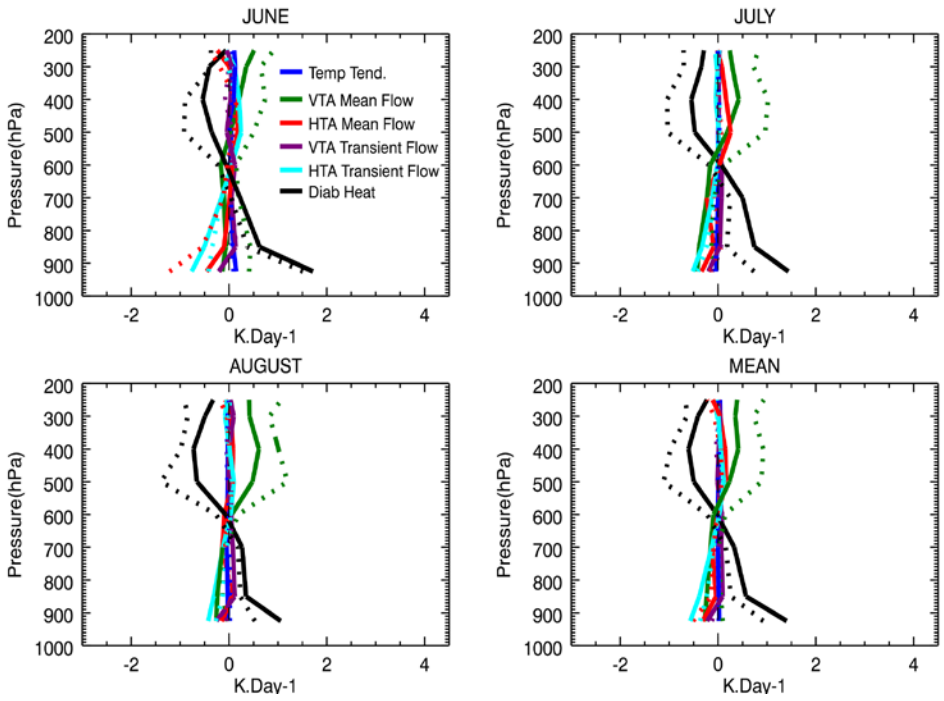

Figure 3.13 Same as fig. 3.12 except for NCEP

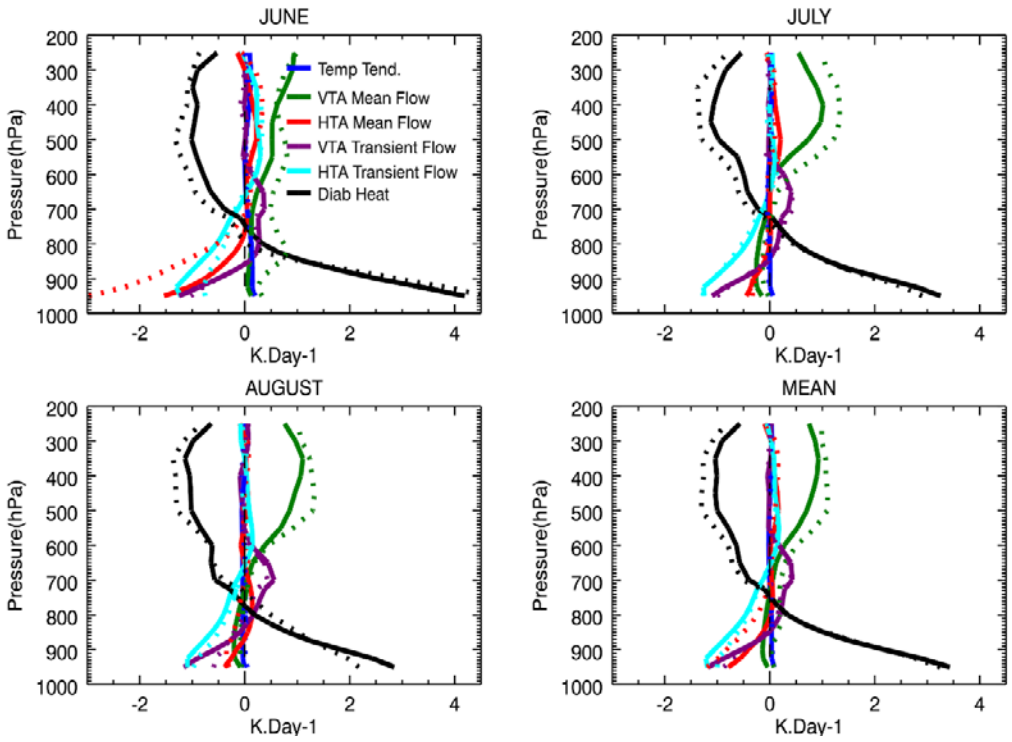

Figure 3.14 Same as fig. 3.12 except for MERRA data.

There is notable change in the structure of vertical temperature advection from the mean flow as time progresses from April to August. During April and May warming from surface to ~600 hPa, cooling from 600 to ~300 hPa, and warming aloft.

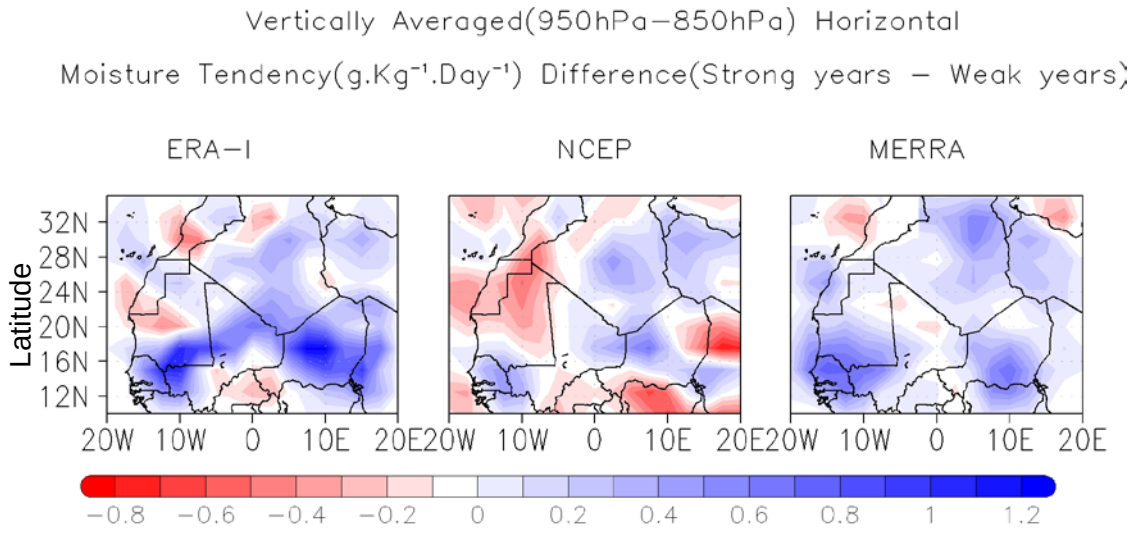

Figure 3.15 Difference of total horizontal moisture advection tendency (g Kg^{-1} day^{-1}) between strong and weak years. Positive values show larger moisture tendency during the strong years compared with the weak years.

This vertical profile heating rate is changed in summer months during which the warming from surface to ~600 hPa decreases in June and becomes cooling in July and August. Furthermore the cooling from 600 hPa to 300 hPa becomes warming in June which then increases in magnitude during July and August. The main difference in the vertical temperature advection between the strong and weak years is that there is more cooling in the low levels and more warming in the upper levels during the weak than the strong SHL years. There is no significant difference in the vertical temperature advection from transient flows between the strong and weak years.

Consistent with the increase in the low level specific humidity in the strong heat low years, more moisture is advected at a rate up to 1.2 g Kg^{-1} day^{-1} (although not statistically significant) in much of the North Africa domain during the strong heat low period compared with the weak years (fig. 3.15) further confirming net moistening of the SHL during the strong SHL years. Vertical profile of total moisture advection by horizontal wind (figs. 3.16, 3.17, 3.18) shows a net moistening in the lower levels (~950 hPa - ~800 hPa) peaking near surface up to 1 g Kg^{-1} day^{-1} (0.5 g Kg^{-1} day^{-1}) in ERA-I (MERRA) and drying in mid-levels (~800 hPa - ~400 hPa) with peak values 0.25 g Kg day^{-1} (0.35 g Kg day^{-1}) around 600 hPa (750 hPa) in ERA-I (MERRA). In the late spring

to early summer period changes in the vertical profile of circulation pattern results in modified moisture advection profile. This comes primarily due to the convergence of moisture from the mean flow in the mid layer around ~700 hPa - ~500 hPa. In general there is net moistening of the atmospheric column (more moistening in the lower levels) and less drying in the mid-levels (figs. 3.14 - 3.16) during the strong heat low years compared with the weak years.

In summary during the strong SHL years the net effect of horizontal temperature advection is less cooling while the net effect of vertical temperature advection is less warming compared with the weak SHL years. There is no clear or significant difference in mean JJA surface sensible heat flux (table 3.3) between the weak years, 58 $W.m^{-2}$ (23 $W.m^{-2}$, and 62 $W.m^{-2}$) and the strong years, 59 $W.m^{-2}$ (21 $W.m^{-2}$, and 61 $W.m^{-2}$) from ERA-I (NCEP, and MERRA) confirming the assertion I made based on the results I found above that the variability in the Saharan Heat low intensity is not directly correlated with variability in the diabatic heating. However there is a consistent temperature increase of ~2 K in the strong years compared with the weak years (Table 3.3) in all reanalyses. This is in contrast to what one might expect

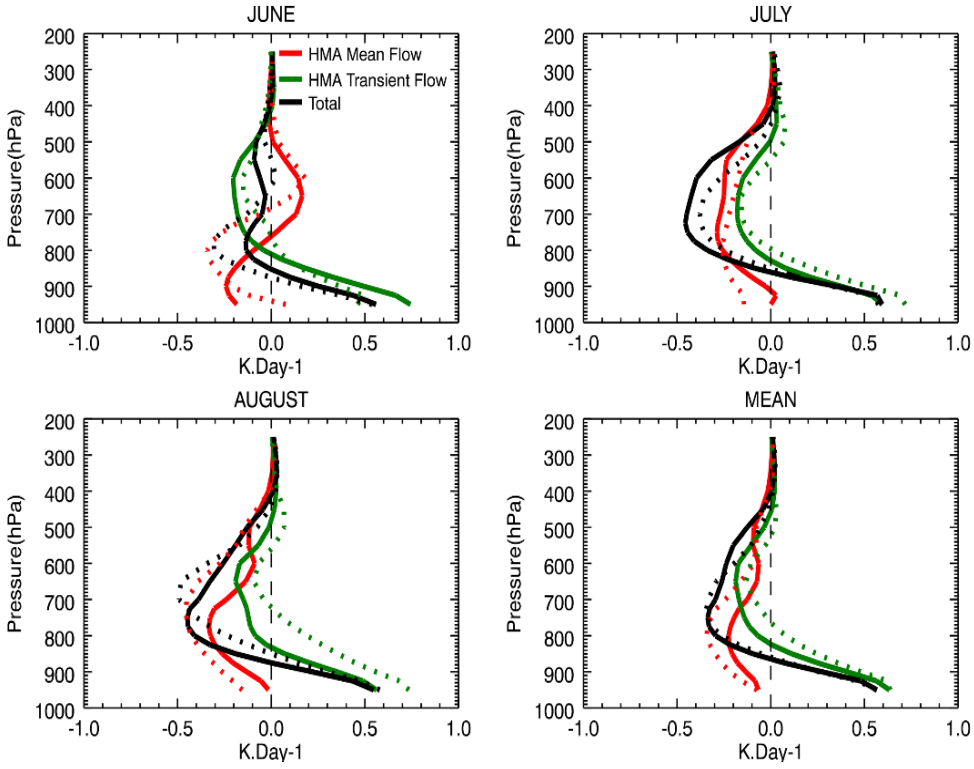

Figure 3.16 Mean horizontal moisture advection (HMA) for the weak SHL years (dashed lines) and strong SHL years (solid lines) from ERA-I data. Red, green, and black lines denote mean moisture advection from mean flow, transient flow and total respectively.

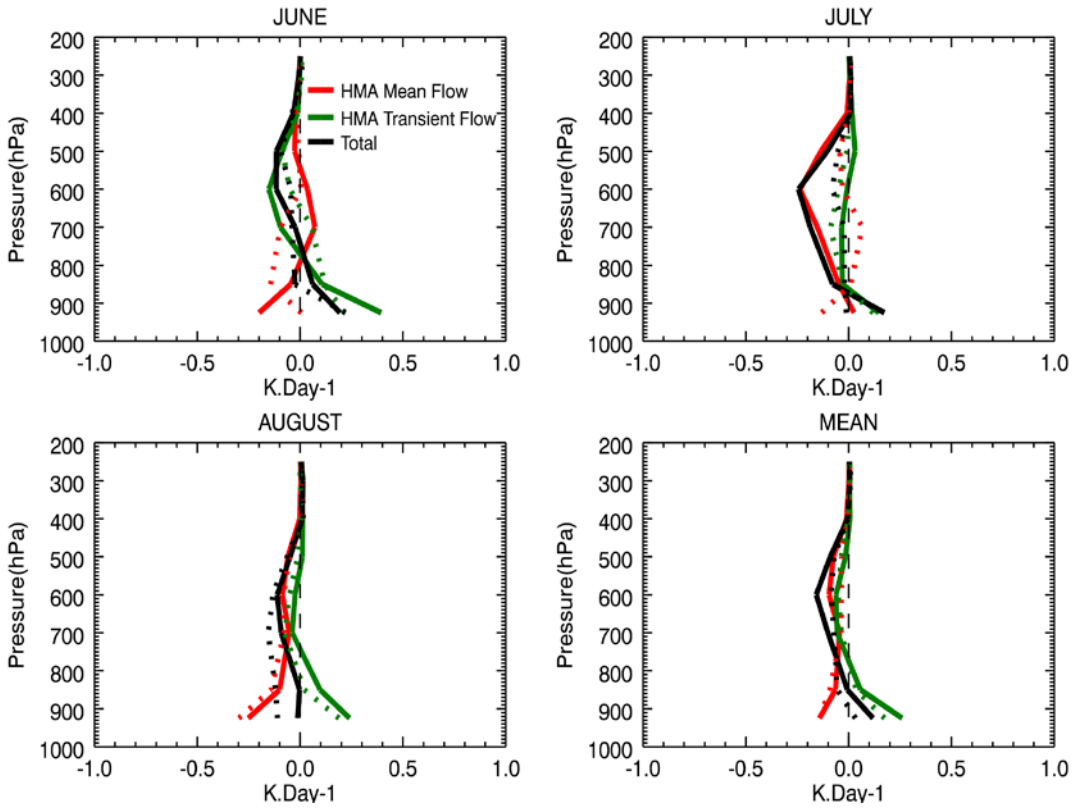

Figure 3.17 Same as fig. 3.16 except for NCEP

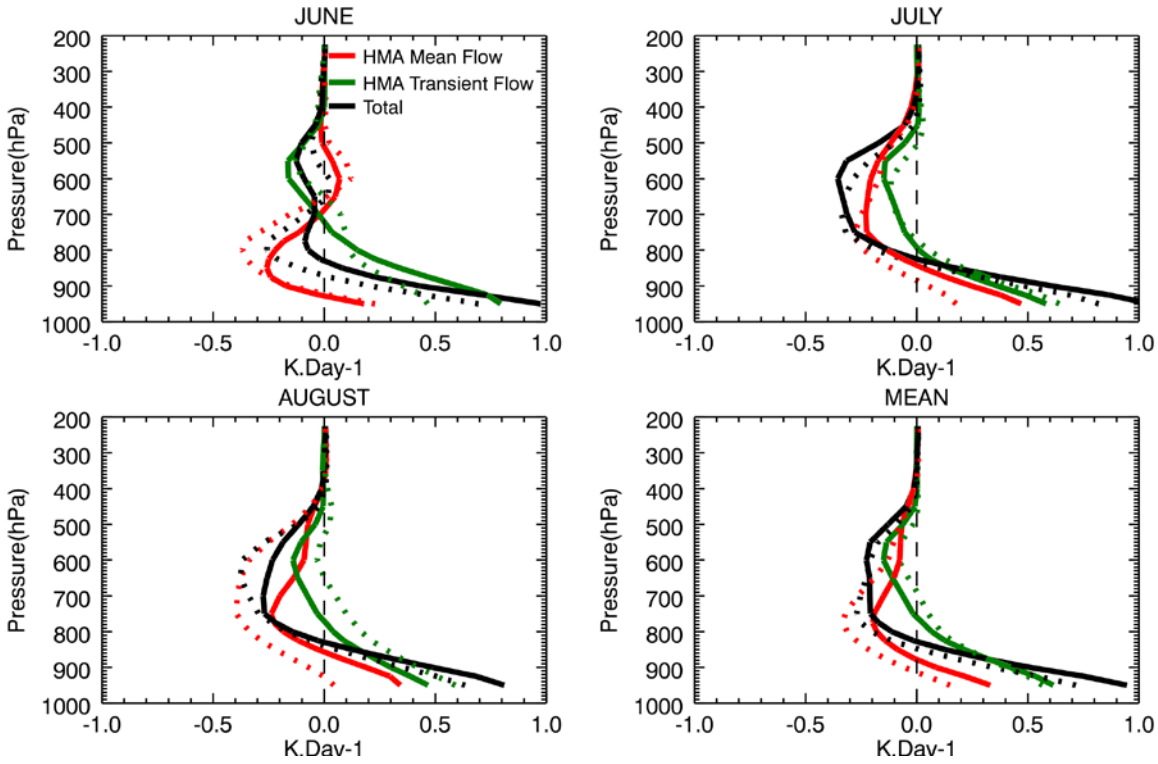

Figure 3.18 Same as fig. 3.17 except for MERRA

as a result of intensification of the SHL leading to larger sensible heat flux convergence into the atmosphere. My results here contrasts what has been suggested in Evan et al., 2015 that year to year changes in diabatic heating of the SHL is strongly correlated with surface sensible heat fluxes. A possible reason for models lack of consistency in reproducing the inter-annual variability in energy budget could be under representation of moisture and dust which are known to play a key role in the heat budget of the heat low region. This will be further investigated in the next chapter.

3.5 Conclusions and Discussions

The Saharan Heat Low is an important feature of the North African climate and driver of the West African Monsoon. As such it is important that climate prediction models are able to replicate the mean state and variability in the SHL over all timescales. However, the processes governing the mean state and variability in the SHL are not well understood. To this end this chapter provided an analysis of the atmospheric heat and moisture budget from reanalysis to resolve the drivers of the SHL. I use the low level atmospheric thickness as an indicator for the heat content of the lower atmosphere as a proxy metric to locate the SHL core for summertime seasonal mean conditions. I then determined the various components of the heat and moisture budget from the thermodynamic equation and moisture conservation equation. Diabatic heating is giagnosed as a residual of the thermodynamic equation and is then decomposed into the radiative and sensible heat terms. The summertime long mean and extreme (warmest and coolest) periods of heat and moisture budget are quantified from three reanalyses products namely ERA-I, NCEP, and MERRA.

The lower troposphere in the SHL region gains energy through, in rank order of magnitude, sensible heat flux, radiative heating and adiabatic subsidence warming. This is compensated for by cooling from horizontal advection in which the transient component dominates over the mean circulation over the core heat low. As such the results are in agreement with previous analyses (Peyrille and Lafore, Evan, Couvreaux) indicating that within the SHL, diabatic heating of the atmosphere is to a first-order approximation controlled by the surface turbulent heat fluxes, which is balanced by horizontal heat flux divergence. Pertinent to the convergent low level circulation, transport of moisture to the central Sahara from around the peripheries is an important component of the SHL system. Here I further discuss the roles and present implications of each process involved.

Diabatic heating, more importantly convergence of sensible heat flux into atmosphere, is an important component of the SHL energy budget. Vertical and

horizontal distribution of diabatic heating influences the physical processes that could affect regional circulations (Martin et al., 2017). Over SHL diabatic heating warms lower layers and more than compensates for the advective terms. Diabatic heating is slightly greater in the strong SHL years compared to the weaker year. This leads us to conclude that variability in the intensity of SHL is not strongly related to variability in diabatic heating. In contrast to this, based on reanalysis data Evan et al. (2015) highlight the role of water vapour in SHL trends. The extreme strong SHL has TCWV about 3 kg m^{-2} higher than the weak SHL. From the dependence of TOA net radiation on TCWV in Fennec observations at supersite 1 (Alamirew et al., 2018) this would cause a 4 W m^{-2} radiative warming of the atmosphere which equates to a 0.12 K day^{-1} warming which is close to the difference in radiative heating between the strong and weak SHL years of 0.1 K day^{-1} (but this is much smaller than the values for the 1000 hPa-700hPa layer)

Horizontal temperature advection from the mean flow is the dominant heating/cooling mechanism on a larger scale: primarily the nocturnal Atlantic inflow and WAM circulations, however over the core SHL the transient flows have a nearly equal effect. This cooling is actually smaller in magnitude during the strong SHL years compared to weaker years. The transient fluctuations can be associated with depressions including the SHL itself and longer-lived migrating cyclones (Fiedler et al., 2013). The SHL exhibits variability at intraseasonal scales (Lavaysse et al., 2010) with pronounced horizontal migrations across the Sahara occurring over a matter of a few days (Marsham et al., 2013b, Todd et al., 2013). During summer the dominant synoptic scale weather systems over summertime West Africa are African Easterly Waves (AEWs) which can feature cool and moist advection at low levels if the surface trough is pronounced (Thorncroft and Hodges, 2001). These are most frequent over Northern Mauritania and Mali often enhanced in the lee of the Air and Hoggar mountains (Fiedler et al., 2013) and will act drive cool advection into the southern SHL core region. Cyclonic systems over North Africa and the Mediterranean can also advect cool midlatitude air into the Sahara but are infrequent in the summer months (Fiedler et al., 2013). Cooling from transients is greater in the strong SHL year. However transient circulation typically involve the coincidence of negative temperature advection and moistening of the atmosphere, the latter leading to radiative warming (Todd et al., 2013, Marsham, et al, 2016). Therefore at short timescales the advective and radiative terms will tend to counteract each other. Marsham et al., 2016 estimate a lag time of a few days for radiative re-warming following advective cooling monsoon surge events. A major difference of horizontal temperature advection between the weak and strong

years is that the mean cooling in the lowest levels is larger (notably may and june) and warming in the mid layer(~800 hPa to 300 hPa) is weaker in the former.

Vertical temperature advection from the mean flow has a small cooling effect from surface to ~600 hPa and more significantly warming in the upper levels above ~600 hPa (Lavaysse et al., 2009) which is a result of the subsidence in the Northern branch of sub-tropical Hadley circulation (Figure 3.5). The net effect of vertical temperature advection over the entire column is warming by 0.3 K day^{-1}. It should be however noted that vertical temperature advection has a strong seasonal variability which is linked with the changes in the vertical profile atmospheric circulation as time proceeds from spring to summer.

Although the sign and vertical structure and inter-annual variability of heating/drying rates are consistent between the reanalyses, magnitudes differ substantially. Roberts et al. (2015) note considerable differences between the various reanalyses products in the representation of low level moisture, associated with differences in underlying model physics and assimilation methods. These differences reduced substantially in field campaign periods when the density and coverage of upper air observations for assimilation increased, pointing to lack of data assimilation as a key source of reanalysis bias. Pertinent to this, reanalysis products have good representation the inter-annual variability of measureable atmospheric variables (q, T...). However this appear to be less the case with variables which are derived diagnostically using measured quantities. On a larger spatial scale there is agreement on the moisture and heat budget of the North Africa region. But this agreement will deviate on smaller regional scale such as the Saharan heat low region. This may not be unexpected that global scale models which are expected to struggle in representing dynamics and thermodynamics of a relatively smaller domain.

Overall my main findings of the heat and moisture budget analysis over the SHL can be summarized with the following points.

- The mean and transient horizontal flows contribute to the cooling of the lower atmospheric levels. Despite its small magnitude, the transient term plays of equal role with in the core heat low region.
- The weak Saharan heat low years have stronger horizontal advection of temperature compared with the strong years.
- There is no significant difference in the diabatic heating between the strong and weak years. This is further confirmed with the sensible heat flux which has no clear trend. That is I find there is no strong correlation of sensible heat flux with variability of intensity of the Saharan heat low.

- More moisture is advected during the strong heat low year possibly explaining the cause for the two contrasting periods of the SHL.
- The climatology of the heat low heat and moisture budget spatial distribution is well reproduced by all the reanalysis outputs. However there is notable difference in the magnitude of heating and drying rates among the different reanalysis outputs when averaged over core heat low region. In particular models tend to deviate from each other in their representation of the inter-seasonal variability.

There is a clear change in the climate of the Saharan region. However the changes are not evident from the diabatic heating rate differences. There is no clear or noticeable change in the surface sensible heat flux between the strong and weak heat low years. There is small change in surface temperature up to 2 K between the strong and weak years. While the changes in the atmosphere is more evident (trend in llat) and also bigger changes in boundary layer thickness. I believe this change is partly related to the increased advection of moisture into the heat low region. However models underestimate the anomalous moisture advection into the SHL, particularly from mesoscale convective processes (Engelstaedter et al., 2015). The model error in moisture will have consequences in the simulation of heat budget and dynamics of SHL. In Chapter IV I will show that surface longwave flux per unit change in standard deviation change in column integrated water vapour (5.5 Kg m^{-2} at BBM for June 2011) is ~8 W Kg^{-1}. It is therefore likely that models will miss the heating from anomalous moisture at least partly explaining the absence of trend in diabatic heating between the contrasting periods. I will also show in Chapter IV cloud has a net cooling effect at the surface which has a contrasting effect to atmospheric moisture. This means that underestimated cloud in models will result in warming of the surface.

In this chapter, I investigated the heat and moisture budget of SHL derived using primarily temperature, wind, and moisture fields. Despite the fact that reanalyses products provide improved representation of state of the atmosphere, however these fields still have their respective varying uncertainity. These errors will be propagated upon calculation of heat and moisture budgets. As a consequence my results will have errors which is larger than the errors of the variables used to derive each term in Eqs. 3.2 and 3.4. This is clearly one of the limitations of this work. At the start of this work we planned to use FENNEC observational atmospheric data to calculate heat and moisture budgets for one season. A similar approach has been implemented in the Arabian peninsula (Blake et al., 1983; Smith, 1986). However the way FENNEC campaign was designed and carried out does not allow for heat and budget calculations. A more complete observational atmospheric data designed gathered in a

similar way as that of the Arabian Peninsula in the 1980's is thus imperative to get a better result for heat and moisture budget which is a possible future work.

To clearly envisage the long term inter-annual variability it is necessary to study seasonal effects, for instance increased anomalous temperature occurred during early spring will be evident during manifested in late summer time. That is what I found in deriving the heat and moisture budget variability during spring-summer time. Therefore a complete investigation of inter seasonal variability of the heat and moisture budgets is necessary to better understand the long term inter-annual variability of the SHL. Further there is a need to understand the resulting feedback on the circulation, particularly on the WAM, due to the intensification of the heat low (Martin et al., 2017). This will provide a complete understanding of the cause and effect of different thermodynamical and dynamical components. These are possible future study.

CHAPTER IV

4. Role of Dust and Water Vapour on radiative Budget of the Saharan Heat Low

(The main results of this chapter are published on Alamirew et al., 2017)

4.1 Introduction

In the previous chapter I have presented the heat and moisture budget of the SHL using reanalysis outputs of atmospheric variables. The results show no clear link between diabatic heating (sensible heating plus radiative heaing) in causing variability of the SHL. It was suggested that this could be due to the models' lack of representation of amount of dust and water vapour. I have also shown in Chapter-III that there is a net advection of moisture (dominantly from the monsoon flow) to the Saharan heat low during summer time. However there is discrepancy in the models' representation of moisture (Engelstaedter et al., 2015;Roberts et al., 2015) which leads to subsequent errors in dynamics and associated dust emission. For instance convective triggered cold pool outflows, which are not resolved in models, are attributed for over 40% of dust emission in the Sahara region (Allen et al., 2013;Heinold et al., 2013). Misrepresentation of moisture and dust in the region will have consequences in thermodynamical energy budget of the region.

Dust and water vapour are known to play important role in shaping the energy budget (Marsham et al., 2016;Tegen and Lacis, 1996) and hence the dynamics of the Saharan heat low (Lavaysse et al., 2011). The variability of radiative budget of the Saharan heat low region is shown to be primarily controlled by the combining effect of dust, water vapour, and cloud (Marsham et al., 2016). In Chapter IV I have shown that there is intensification of SHL in recent decades confirming previous results (Evan et al., 2015;Lavaysse et al., 2016). The cause for these trends is debatable. However radiative warming from increasing water vapour is suggested to be possible reason (Dong and Sutton, 2015;Evan et al., 2015) that strengthens the SHL, which subsequently enhances the moist low level monsoon flow driving greater water vapour transport into the SHL and further warming with an implied enhanced West African Monsoon. This indicates water vapour and dust play significant role in determining the radiative and thus heat budget of the Saharan heat low. Therefore there is a need to better quantify their radiative effect.

Previous studies have quantified direct radiative effects (DRE) of dust aerosol at the top of atmosphere (TOA) and surface from in situ observations and satellite data (Ansell et al., 2014;Banks and Brindley, 2013;Yang et al., 2009), whilst Marsham et al., 2016, hereafter M16, extend this empirically to consider water vapour variations, and implicitly cloud, as well as dust. However, there remain important gaps in our understanding. First, there are substantial uncertainties in the magnitudes of radiative fluxes (and other heat budget terms) across both the various reanalyses and observations. Second, separating the radiative effects of water vapour from both its and associated clouds and from dust aerosol is challenging, given the strong co-variability of dust and total column water vapour (TCWV) anomalies in the Sahara associated with monsoon surges and resulting convective cold pool events ('haboobs') which transport water vapour and dust into the central Sahara (Allen et al., 2013;Garcia-Carreras et al., 2013;Heinold et al., 2013;Marsham et al., 2013b). As such, there is a need to quantify more fully the DRE of dust and water vapour, both independently and together, over the Sahara. This information is necessary to resolve the processes that govern the fundamental structure and maintenance and variability of the SHL. Addressing these research gaps is hindered by the acute shortage of routine observations in the region and large discrepancies between models and reanalyses (Evan et al., 2015a; Roberts et al., 2015).

This chapter seeks to address these gaps in our understanding of radiative processes within the SHL during summer. Specifically, to quantify the separate roles of water vapour and dust aerosol in controlling the top of atmosphere, surface, and the vertical profile of the atmospheric column radiative budget. This will be achieved through radiative transfer (RT) model simulations using uniquely detailed observations of atmospheric conditions over the SHL region during summer, including those from the main supersite of the recent Fennec field campaign (Marsham et al., 2013b). Best estimates and associated uncertainty are established through a set of RT model experiments testing the sensitivity of radiative flux and atmospheric heating rates to both water vapour and dust variability and to uncertainties in a set of controlling variables. In this way, I can inform interpretation of hypotheses on drivers of SHL variability and its wider impact on the regional climate. A description of the radiative transfer code is given in section 4.2 followed by list of input data used to run the RT model (section 4.3). The different experiments used towards the optimal model configuration are presented in section 4.4. Results of the mean state and sensitivity RT runs for water vapour and dust are given in section 4.5. The chapter is concluded by presenting the summary and conclusion of my results in section 4.6.

4.2 Data and Methods

4.2.1 Description of the SOCRATES Radiative Transfer (RT) model

Radiative transfer codes are generally used to calculate radiative fluxes in the atmosphere from which heating rates can be derived. RT codes are integral part of general circulation models and other climate models driving the interaction of radiation with surface and atmospheric constituents and thus calculating radiation flux and resulting heating rates. The research questions are addressed through simulations from a column stand-alone RT model. Such models are commonly used for detailing the combined and unique radiative impact of dust aerosol and water vapour (Osborne et al., 2011;Osipov et al., 2015;Otto et al., 2009;Otto et al., 2007;Otto et al., 2011;Slingo et al., 2006). RT models typically comprise a radiative transfer core and a pre-processor to configure the necessary information on the radiatively active atmospheric constituents and surface characteristics. Typically, these include meteorological and gas component profiles from observations, reanalysis products or weather/climate models, spectral aerosol optical property profiles and surface properties.

Here I use SOCRATES (Suite Of Community Radiative Transfer codes based on Edwards and Slingo) (Edwards and Slingo, 1996;Randles et al., 2013) model configured with observed and idealised profiles of water vapour and dust aerosol, as described below. The core code of SOCRATES is used in the Met office's global circulation model (GCM) and Numerical Weather prediction (NWP) forecasts. These are among the best models used for seasonal and weather forecasting and thus reason for my choice of SOCRATES. SOCRATES is a flexible RT model, which calculates the longwave and shortwave radiative fluxes and heating rates throughout the atmosphere given the atmospheric and surface properties of that column, the solar zenith for the location, date and time. SOCRATES is operated via two-stream approximation in which radiation is taken to have two directions, upward or downward. Radiative flux calculations are made for parallel plane atmosphere with spectral resolution ranging over the shortwave and longwave from 0.2 to 10 μm divided in 6 bands and 3.3 μm to 10,000 μm divided 9 bands respectively. Column atmospheric and surface characteristics required to run the RT model are described in sections 4.3.2 and section 4.3.3.

Calculations using radiative transfer codes involve three steps. First spectral information of the active absorbing gases, cloud, and desired aerosols for each band is generated and stored in a spectral file. The radiative transfer codes read this file in the

calculation of fluxes and do not need to be changed for further calculations unless the spectral band or absorption properties are changed. In the second stage of pre-processing atmospheric profile data are prepared and specified to the code. The atmosphere is divided into number of homogeneous layers starting from the top of the atmosphere. Inputs used to run the radiative transfer model typically include active gases, meteorological fields, and aerosol mixing ratios and surface properties. In the last stage the actual code is run to calculate radiances, fluxes, and heating rates in the column atmospheric profile. Figure 4.1 summarises the key steps in radiative transfer calculations. A detailed description of SOCRATES is provided in (Randles et al., 2013).

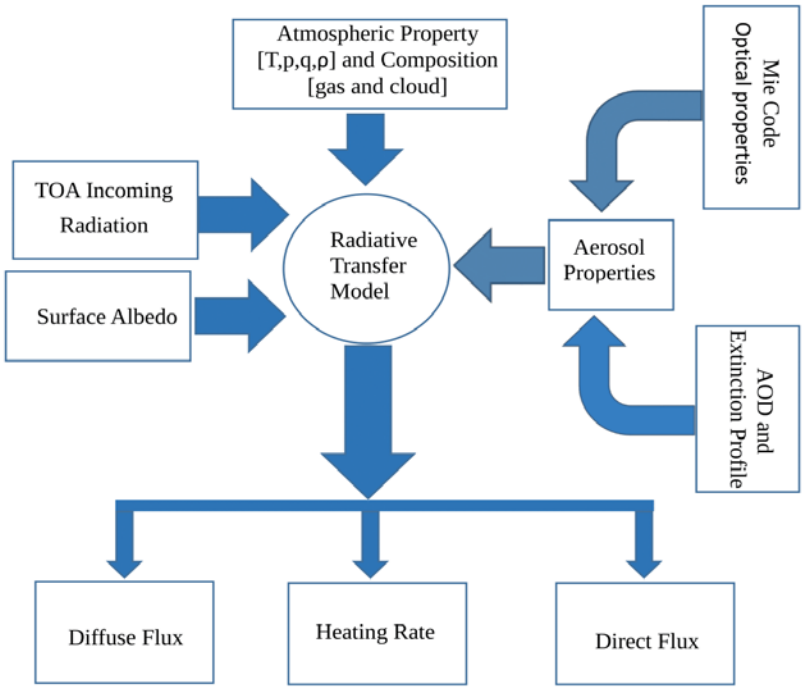

Figure 4.1. A schematic showing the key steps involved in the processes of radiative transfer calculation

4.2.2 Observed top of atmosphere and surface radiation measurements

I use satellite retrievals of TOA radiation from two sources. 1). The EUMETSAT Geostationary Earth Radiation Budget (GERB) (Harries et al., 2005) level 2 products of Averaged Rectified Geolocated (ARG) fluxes at approximately 17 minute time and 50km spatial (at nadir) resolution, with spectral ranges 0.32 to 4μm in the shortwave

and 4 to 100 μm in the longwave. 2). The Clouds and the Earth's Radiant energy System (CERES) (Wielicki, 1996) instrument which has channels that measure total radiance (0.4-200μm) and shortwave radiance (0.4-4.5μm). Since there is no longwave-only channel on CERES, daytime longwave radiances are determined from the difference between the total and shortwave channel radiances. I use two CERES products: (i) the monthly mean Energy Balanced and Filled (EBAF) product at 1-degree resolution. (ii) The CERES Level-3 SSF1deg_Hour TERRA footprint gridded data (CERES-footprint) instantaneous, twice daily with 1-degree resolution.

For our high resolution, pixel based analysis focused on a single location (BBM), cloud screening is notoriously challenging. For GERB data I apply the EUMETSAT cloud mask to derive clear sky and all-sky conditions and for CERES data I use both all sky and clear sky products. MODIS cloud parameters are used to derive CERES cloud free fluxes. However, analysis of GERB all-sky minus clear-sky fluxes at BBM suggests unrealistically small cloud DRE (~2 $W.m^{-2}$ in longwave flux), which suggests that the cloud mask is not robust. I therefore choose only to use GERB all sky fluxes and limit the clear sky-only analysis to the CERES products. For 'validation' of the 'optimum' model configuration(section 4.3), I favour comparison with GERB (all-sky) because the time period of the CERES monthly product is not exactly compatible with the RT simulations of 8-30th June, whilst the CERES footprint data has observations twice daily.

Surface measurements of shortwave and longwave upwelling and downwelling radiation are obtained from Kipp and Zonen CNR4 radiometers situated at 2m height deployed at BBM during the FENNEC campaign (Marsham et al., 2013b). The surface radiometer measure 0.3 to 2.8μm in the shortwave and 4.5 to 42μm in the longwave which is narrower spectral range coverage than both GERB and CERES. Because of the narrower bands, radiometer measurement can miss up to 3.5 W m^{-2} in shortwave atmospheric heating and up to 3.8 W m^{-2} in net longwave (Banks et al., 2014).

4.2.3 Atmospheric profile and surface characteristics

I provide here a detailed list of input data which are used to run the RT model. Inputs for the model include meteorological fields (temperature, specific humidity), cloud mixing ratio and cloud fraction, active radiative gases mixing ratios, surface properties (skin temperature, surface pressure, broadband albedo, and emissivity). To include the effect of aerosols, optical properties and the vertical profile of mass mixing ratio of the required aerosol should be provided.

I specify these inputs as accurately as possible using observations from the recent Fennec field campaign, which obtained unique data from within the SHL region during June 2011 (Ryder et al., 2015). I use observations from ground-based instruments deployed at the Fennec supersite at BBM (Marsham et al., 2013b) and various aircraft flights (see Ryder et al., 2015 for overview) complemented with fields from the ECMWF ERA-I, and MERRA reanalyses where direct observations are inadequate.

Profiles of temperature and water vapour (fig. 4.1) are obtained from radiosonde measurements at BBM for June 8th-30th 2011. The temporal resolution of radiosonde measurements varied from 3-6 hour over the study period. A distinction can be made between the cooler, drier, less dusty Saharan 'maritime' phase from around 8th to 12th June to a hotter, moister, dustier 'heat low' phase from around 13th to 30th June (fig. 4.1a) during which time both synoptic scale monsoon surges and meso-scale convective cold pool events transported both water vapour and dust into the heart of the SHL (see Ryder et al., 2015; Todd et al., 2013b for full details). For comparison, profiles of water vapour from Era-I reanalysis are shown in fig. 4.1b. Despite the good agreement between measurement and model outputs, ERA-I underestimates specific humidity in the lowest level by ~4.9% (MERRA by 4.5%). Note that the error in reanalysis at BBM is relatively small because the Fennec radiosondes data were assimilated. In the subsequent absence of such observational data I expect reanalysis errors to be greater given the known problems of reanalysis model representation of meso-scale convective processes in the region (Garcia-Carreras et al., 2013; Roberts et al., 2015; Todd et al., 2013). Such mesoscale convective 'cold pool' outflows (known locally as 'haboobs') are known to make a significant contribution to moisture advection as well as being the dominant dust emission process (Marsham et al., 2013b; Trzeciak et al., 2017). Red arrows in fig. 4.1a denote major haboob events. Detailed information on the Characteristics and frequency Convective cold pool outflows over the Sahara desert is provided in Chapter V.

Profiles of trace gases needed by the radiative transfer model (CO_2, O_2, N_2O, O_3, and CH_4) are taken from the standard tropical atmosphere (Anderson et al., 1986). Temperature and water vapour profiles beyond the upper maximum height of the radiosonde data (approximately 20 km) are also taken from the standard tropical atmosphere. This is unlikely to affect RT model results significantly since there is little day to day variability in the uppermost part of the atmosphere.

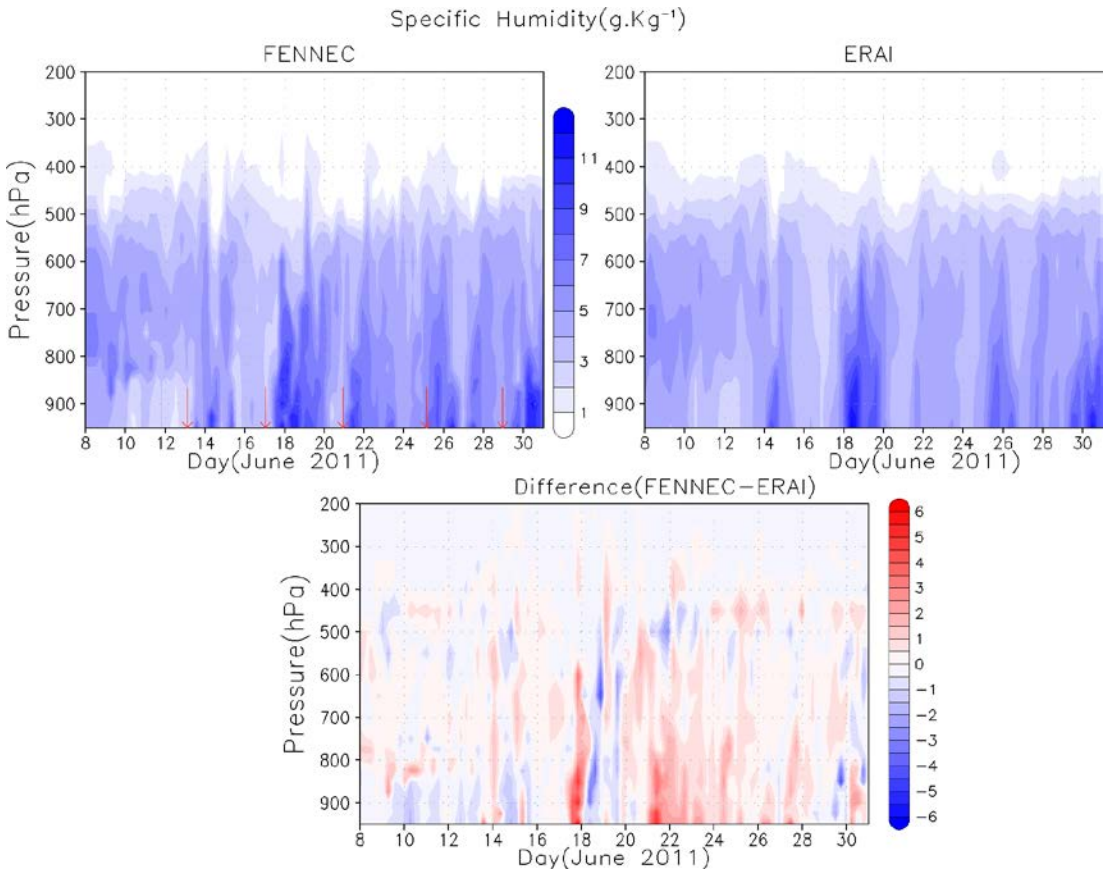

Figure 4.1. Vertical Profile Specific Humidity (a) FENNEC radiosonde measurements (b) ERA -I and (c) Difference between (a) and (b). Red arrows in (a) denote times of major haboob events

Acquiring observations of the vertical structure of clouds of sufficient quality for radiative transfer calculations is always challenging. Here I use the ERA-I and MERRA outputs of cloud fraction, liquid and ice water mixing ratios. Cloud is treated to have maximum overlap in a column where ice and water are mixed homogeneously. During the Fennec period, cloud was characterised by shallow cumulus or altocumulus near the top of the PBL and occasional deep convection. It is likely that the relatively coarse vertical and horizontal resolution of both reanalysis models will have considerable bias and I recognise that this is likely to underestimate the true cloud-related uncertainty. For example, M16 suggest that ERA-I underestimate cloud fraction by a factor of 2.4.

I calculate surface albedo from surface observations of shortwave flux at BBM for the days when good measurement is available (see fig 4.2). During the days where measurements were not good, I use the diurnal average surface albedo of all other days. The mean surface albedo at BBM is 0.36 and shows strong diurnal cycle, varying

with solar zenith angle giving maximum surface shortwave reflection during the morning and evening hours, i.e. when the sun is at high solar zenith angles. This has an impact on the diurnal cycle of dust radiative effect (Ansell et al., 2014;Banks et al., 2014;Osipov et al., 2015). Fennec does not provide measurements of skin temperature and thus I look for alternative best approximates from ERA-I and MERRA. For comparison, I also use the skin temperature product form CERES Level-3 SSF1deg_Hour TERRA footprint data.

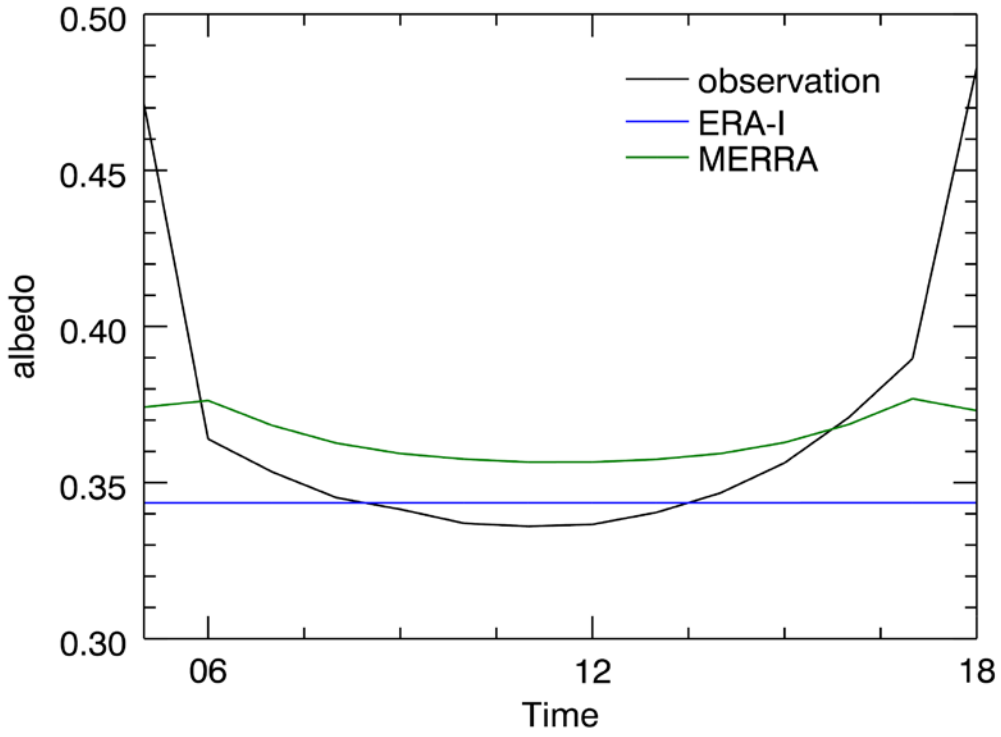

Figure 4.2. Diurnal Cycle of mean Surface Albedo at BBM

4.2.4 Dust Extinction profile and optical properties

No observations of the vertical profile of dust loading at BBM are available from the Fennec instrumentation. Since the model requires the vertical distribution of mass mixing ratio of dust as an input, I use the long term mean extinction coefficient profiles for dust aerosol derived from the Cloud-Aerosol Lidar with Orthogonal Polarization (CALIOP, (Liu et al., 2009;Winker et al., 2009)) satellite instrument. These are then scaled at each model time step to yield the observed column integrated AOD

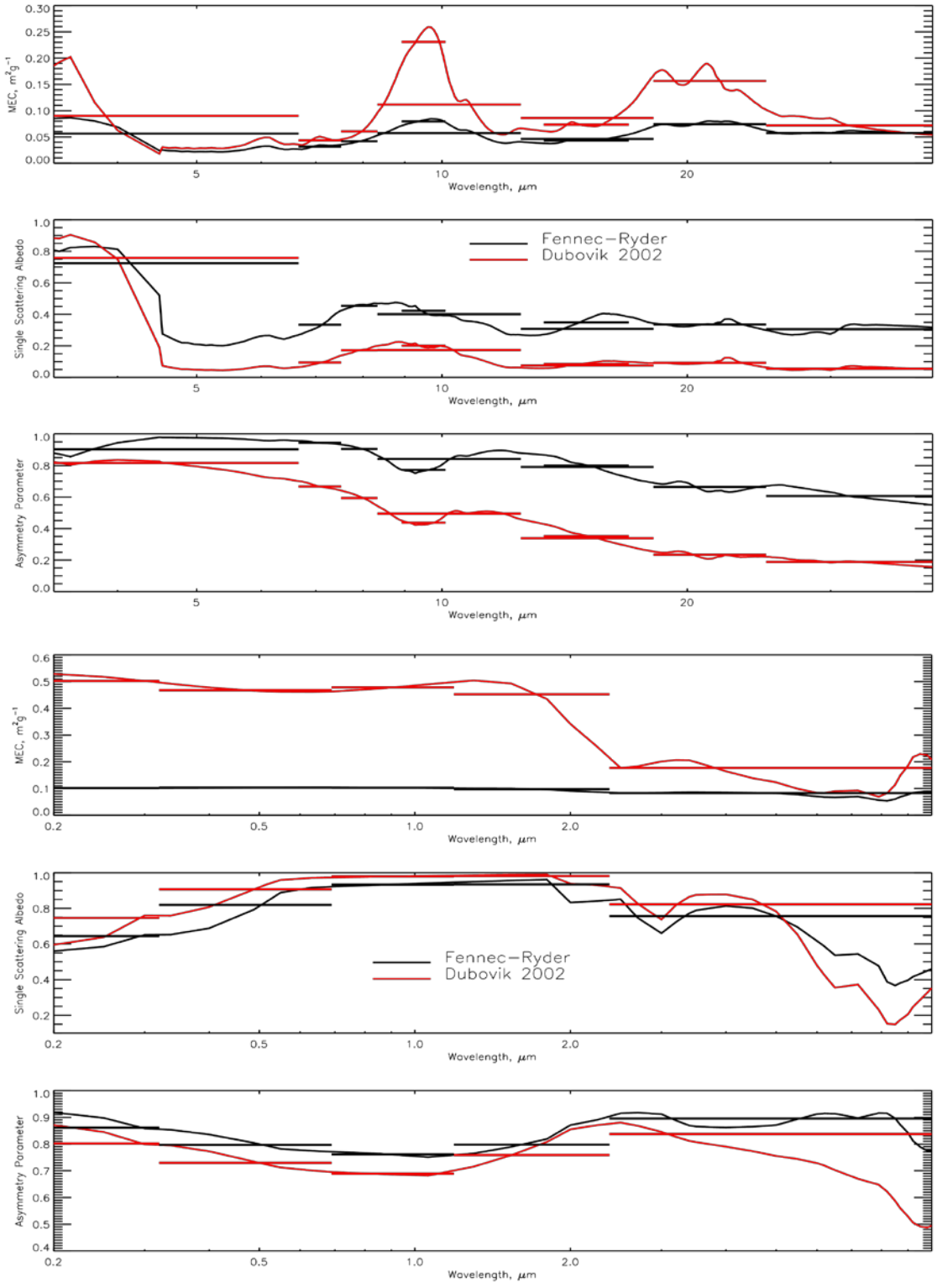

Figure 4.3. Wavelength dependence of optical properties of dust particle for longwave (top three) and shortwave (bottom three panel). The continuous lines are the spectrally resolved optical properties the horizontal lines are the band-averaged data that are used in the RT code.

from the BBM AERONET sun photometer. I then use the mass extinction coefficient (in m^2 Kg^{-1}) to convert dust extinction coefficient (in m^{-1}) to dust mass mixing ratio (kg kg^{-1}) as required by the model (Greed et al., 2008). Mass extinction coefficient is calculated from Mie code (see fig. 4.3). Data from all individual CALIOP satellite orbits over the 2006-14 period were quality controlled and screened to retain dust aerosol only observations using the method described in (Todd and Cavazos-Guerra, 2016), which provides sampling for robust characterisation of aerosol distribution in 3 dimensions (Ridley et al., 2012;Ryder et al., 2013a;Todd and Cavazos-Guerra, 2016;Winker et al., 2009). The long term mean extinction coefficient profile at BBM (fig. 4.4) shows a regular decrease of extinction through the aerosol layer which extends up to about 5 km at the top of the planetary boundary layer, which is also seen in Fennec airborne measurements from 2011 (Ryder et al., 2013b).

AOD data used to scale the mean extinction coefficient profiles are taken from retrievals from the AErosol RObotic NETwork (AERONET) (Holben et al., 1998) instrument at BBM, using Level-2 data, which is cloud screened and quality assured. I compared AERONET AOD with estimates of AOD from the SEVIRI instrument on Meteosat 9 satellite (derived from the 550nm channel using the algorithm of Banks and Brindley (2013)) over the June 2011 study period (fig. 4.5). The more frequent dust events during the latter half of the month (heat low phase) compared to the earlier heat

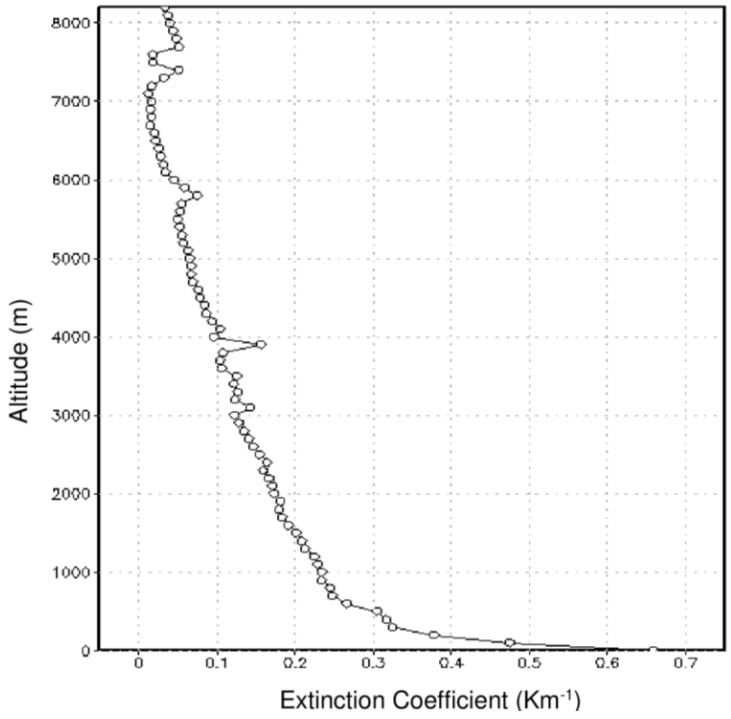

Figure 4.4. Caliop mean Extinction Coefficient profile at BBM 2006-13

maritime phase is apparent, with dust events frequently associated with high water vapour indicative of convective cold pool 'haboob' dust events (see fig. 4.1a). The estimates of mean AOD agree to within 20% and there is a strong correlation between the two estimates of 0.7, despite some apparent dust events apparent in SEVIRI but not AERONET e.g. 13th and 29th June. This is mainly due to AERONET masking dust as cloud particularly in cases when dust and cloud coexist.

Night time dust emission is common during summer in the SHL region, although I expect dust shortwave daytime radiative effect to be dominant (Banks et al., 2014). Estimation of AOD at night is problematic for most passive instruments and I use the following method: estimate AOD from observations of scattering from the nephelometer instrument deployed near the surface at BBM (Rocha-Lima et al., 2017), based on the regression of scattering to column integrated AOD during coincident daytime observations. The nephelometer-based estimates of AOD will account for night time emission of dust due to Haboobs (Marsham et al., 2013b) but since haboobs tend to occupy a shallow layer, than the better mixed daytime dust, this will tend to overestimate AODs estimated at night.

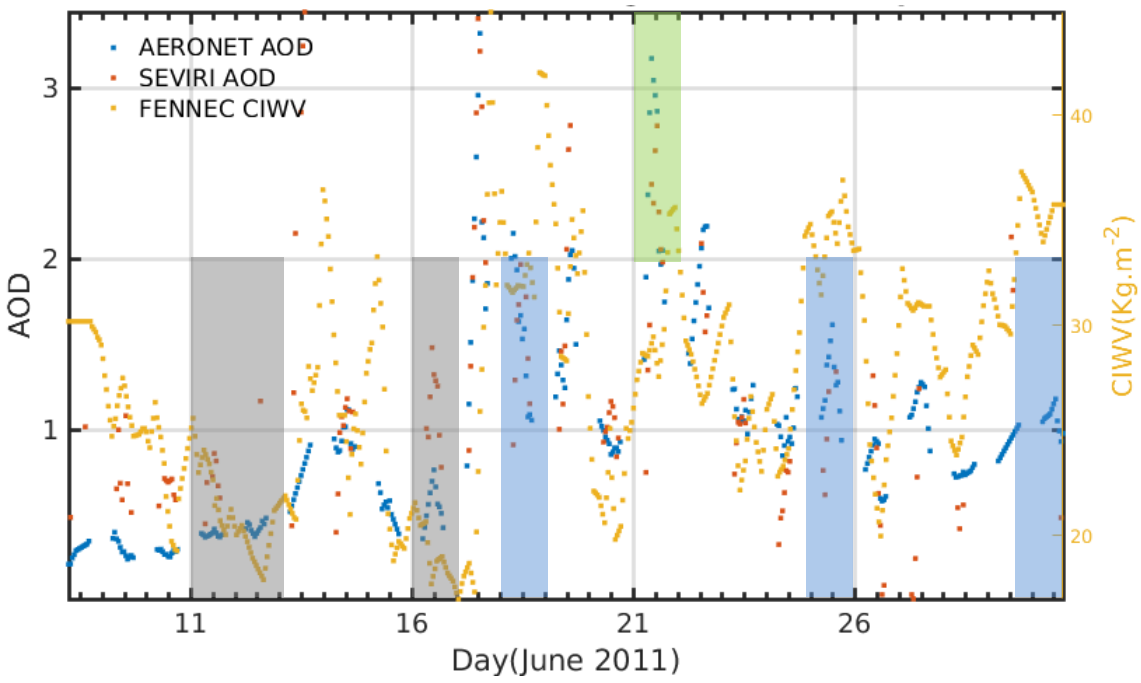

Figure 4.5. AOD from AERONET and SEVIRI, and column integrated water vapour from FENNEC observation.Gray shades show driest (11, 12, and 16), blue shades shows most humid days (18, 25, and 30) Nephelometer measurement and green shade shows a major haboob event occurred on the 21st which resulted in large dust emission

4.3 Description of RT model experiments

I undertake two types of RT experiment in this study (i) model 'configuration mode' in which I test the sensitivity of simulated radiative fluxes to uncertainty in as many of the input variables as possible, described in Section 4.2.1, summarised in Table 4.1, with results provided in Section 4.4. This will result in an acceptably configured model for experimental analysis. (ii) Model 'experiment mode' to specifically address the research questions using the 'optimal' model configuration. The experiments are described in Section 4.3.2, summarised in Table 2, with results described in Section 4.4. These include RT model experiments run for durations from one day to one month (June 2011).

Table 4.1. Summary of model configuration sensitivity analysis

Sensitivity input variable	Source of data for sensitivity run	Sensitivity results	'Optimal configuration choice
surface albedo	Fennec measured quantity ERA-I	Difference of up to 16 W m^{-2} in TOA net SW flux	Surface Albedo calculated from flux measurements
skin temperature	ERA-I MERRA	Difference of 6 W m^{-2} in surface net LW flux MERRA SKT OLR 4 W m^{-2} more than ERA-I	ERA-I skin temperature estimate
Surface emissivity	CERES MERRA	Differences of 2.3 W m^{-2} at TOA LW flux and 5 W m^{-2} at the surface.	MERRA reanalysis estimates
Cloud fraction and mixing ratio	ERA-I MERRA	Difference of 4 W m^{-2} both at TOA and surface net SW flux	ERA-I
dust size distribution	Dubovik FENNEC-Ryder	TOA SW dust DRE -2 W m^{-2} Using Dubovik and 23 W m^{-2} using Ryder-FENNEC TOA net LW Dubovik 7 W m^{-2} more than FENNEC	Dubovik

4.3.1 RT configuration mode experiments towards 'optimal' configuration

For some quantities, I do not have direct observations so I use alternative data from various sources. In the 'configuration mode' I test the uncertainty of the modelled radiative fluxes to uncertainties in these model inputs using the experiments summarised in Table 4.1. Then comparison of TOA fluxes with satellite observation allows us to arrive at what I consider to be an 'optimal' model configuration for the subsequent model 'experiment mode' analysis.

(i) Surface skin temperature. Since there are no complete observations of skin temperature I use reanalysis products as inputs to the RT code and I use both these data to further investigate sensitivity of flux to uncertainty in skin temperature. Figure 4.6 displays the time series of surface skin temperature from ERA-I, MERRA, and CERES footprint data. Root mean square error (RMSE) of the reanalysis products with respect to CERES-footprint data are high (4.5 K and 5.5 K for MERRA and ERA-I, respectively). Despite the higher RMSE of ERA-I skin temperature compared with RMSE of MERRA, the RMSE of ERA-I 2 m air temperature (Figure 4.6) with respect to flux tower measurement is 3.1 K (3.7 K, MERRA). The relatively bigger RMSE in skin temperature could be due to the uncertainty in CERES measurements.

(ii) Surface emissivity. I test the sensitivity of radiative fluxes to uncertainty in estimates of surface emissivity using CERES measurements and MERRA output that have monthly mean values of 0.89 and 0.94 respectively.

(iii) Surface albedo. I noted that in contrast to observations the reanalysis products have weak representation of the diurnal cycle in surface albedo (fig. 4.2). Although I use observed surface albedo throughout all my experiment model RT runs, I also test the sensitivity of TOA shortwave flux to reanalysis surface albedo errors.

(iv) Dust size distribution. Dust radiative effect is known to be influenced by size distribution (Otto et al., 2009; Ryder et al., 2013a, b), which remains uncertain over the Sahara. I test the RT model sensitivity to two different and highly contrasting dust size distributions: (i) derived using AERONET sun photometer inversions from Cape Verde , representative of transported dust (Dubovik et al., 2002), referred to as Dubovik hereafter and (ii) measured directly from aircraft observations during the Fennec campaign (Ryder et al., 2013b) referred to as Fennec-Ryder hereafter, which include a pronounced coarse-mode with effective diameter in the range between 2.3 and 19.4 μm, contrasting with the much finer size distribution of Dubovik from AERONET. In both cases the dust size distributions and the same refractive index are used as inputs to Mie code in the RT pre-processor from which the optical properties of dust are

calculated, specifically the single scattering albedo (ω or SSA), mass extinction coefficient (known as MEC or K_{ext} units $m^2\,Kg^{-1}$), and asymmetry parameter (g), for the relevant spectral bands applied in the RT model. I would like to remind the reader that spherical shape assumption of dust particles in Mie theory could cause some error calculation of optical properties (Mishchenko et al., 1995). However, we will not consider this here as it is neither the objective nor scope of this research. Figure 4.3 displays the wavelength dependence of optical properties for both Dubovik and Fennec-Ryder dust size distributions. The continuous lines are the spectrally resolved optical properties and the horizontal lines are the band-averaged data which are used in the RT code. SSA values in the band covering the spectral range 0.32 to 0.69 μm are 0.82 and 0.91 for Fennec-Ryder and Dubovik respectively. The coarser particles in Fennec-Ryder result in a lower SSA – i.e. more absorbing dust. Note that in the model since AOD is fixed based on measured values, the vertical profile of dust mass mixing ratio is adjusted so that when combined with the MEC shown in fig. 4.3, the AOD is correct. Therefore the differences in MEC between the two datasets shown in figure 4.3 cannot result in differences within the RT model. However, differences in SSA and g are able to exert different impacts on the radiative fluxes within the RT model, as described in section 4.3.

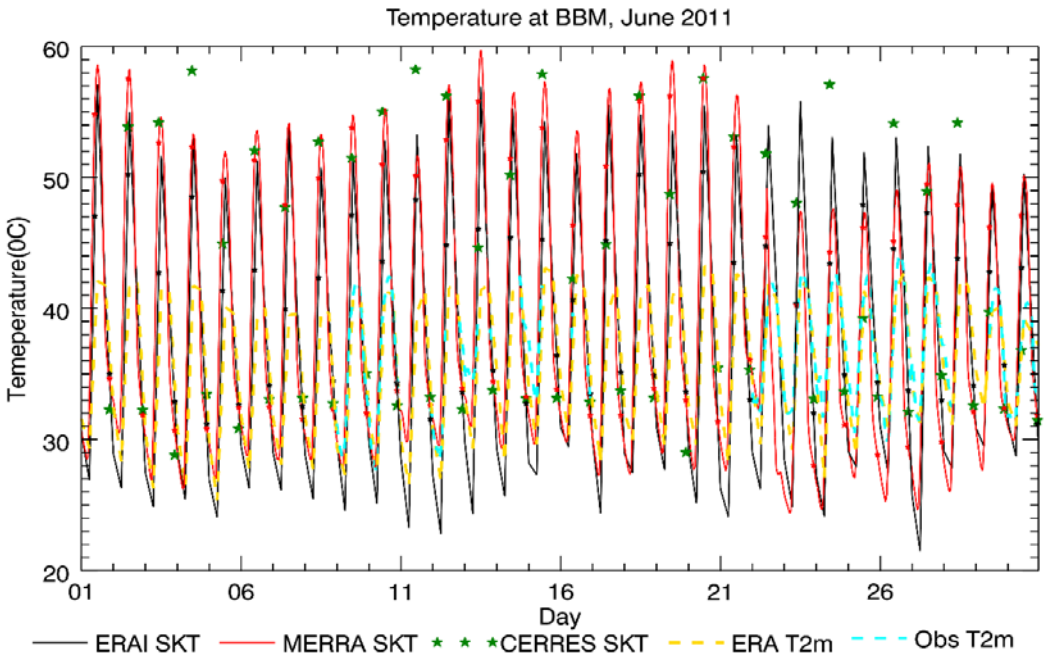

Figure 4.6, Surface skin temperature (SKT) and 2 m air temperature at BBM: Skin Temperature Black: ERAI, Red: MERRA, and Green Star: CERES footprint, 2 m air temperature Gold:ERAI and Cyan: Flux Tower measurement. The black and red stars denote ERAI and MERRA skin temperature at the time steps when there

4.3.2 RT model 'experiment mode' design

Using the suitably configured RT model (Section 4.3.1) I address the research questions, specifically to quantify the combined and separate DRE of water vapour and dust, I undertook a number of experiments summarized in Table 4.2, i.e. the 'experiment mode'. For all the experiments RT calculations are made for each day using the atmospheric profiles at hourly time steps over the diurnal cycle, and the mean flux and heating rates are derived by averaging outputs at each time step. All input data are linearly interpolated to a one-hour temporal resolution.

Table 4.2. Description of the RT 'experiment mode'. Names of different experiments acronyms are defined as 'n' = NO, 'w' = with, 'D' = Dust, 'C' = Cloud, 'WV' = water vapour, and 'sen' = sensitivity

Name	**Description**	**Water vapour**	**Aerosol**	**Cloud**
nDnC	Dust free and Cloud free atmosphere	Observed 8th-30th June 2011	None	None
nDwC	Dust free but cloudy atmosphere	Observed 8th-30th June 2011 diurnal cycle	None	ERAI MERRA
wDnC	Cloud free but dusty atmosphere	Observed 8th-30th June 2011 diurnal cycle	AERONET AOD scaled with CALIOP Extinction	None
wDwC	Dusty and Cloudy Atmosphere	Observed 8th-30th June 2011 diurnal cycle	AERONET AOD scaled with CALIOP Extinction	ERAI MERRA
senDnC	Sensitivity to full range of possible AOD	Mean diurnal WV	Linear increase in AOD 0.0 to 3.0 Constant AOD each time step for a given run	None
senWVwDnC	Sensitivity to full range of possible WV	Linear increase in TCWV from 10 to 40 kg m-2 at 2.5 kg m-2 interval with mean diurnal WV profile	Mean Diurnal AOD	None

For the experiments with (‘w’) and without (‘n’) dust ('D') I simulate the 8th-30th June 2011 period. For the sensitivity (‘sen’) experiments, I simulate linearly increased levels of dust AOD and water vapour. I use runs both with cloud (‘C’) and with no cloud (nC). For dust sensitivity experiment (‘senDnC’), AOD is increased linearly over the range 0 (dust free) to 3 (extremely dusty), while keeping the mean value of water vapour constant. For water vapour sensitivity experiment (‘senWVwDnC’) the mean diurnal profile of water vapour is used but is scaled so that the column integrated water vapour increases from 10 to 40 kg m^{-2} and the mean AOD is used in each case.

DRE of dust is derived by (i) subtracting TOA and surface fluxes of experiment wDnC from nDnC (ii) linear regression of the flux dependence on the range of dust AOD from the dust sensitivity experiments (senDnC), in which a single diurnal cycle is simulated. The results are presented in Section 4.4.2. The impact of water vapour is determined by (i) composites of dry versus humid days from the nDnC experiment (ii) linear regression of the flux dependence on the range of water vapour from the water vapour sensitivity experiments (senWVwDnC).

4.4 Results and discussion

4.4.1 RT model optimum configuration and validation

Prior to testing the main research questions related to the relative roles of dust and water vapour in radiative heating (Section 4.4.2), the RT model was configured based on the ‘configuration mode’ sensitivity analyses (described in Section 4.3.1, Table 4.1) and comparison with observed TOA fluxes from the CERES-EBFA monthly mean product (clear sky in the case of all sensitivity analysis except the cloud sensitivity which I compare to CERES-EBFA all sky).

Sensitivity of RT simulated fluxes to uncertainty in the surface skin temperature and emissivity is low compared to the sensitivity to other factors (Table 4.1) with variations of ~2 W m^{-2} at TOA and 5-6 W m^{-2} at surface. Based on bias with respect to CERES-EBFA observations I use ERA-I skin temperature and MERRA emissivity products for the ‘optimal’ configuration.

Sensitivity to the two contrasting dust size distributions is pronounced. As expected results using Fennec-Ryder dust show much stronger absorption in the shortwave compared with the Dubovik dust distribution, and the resulting TOA net shortwave flux is higher by 25 W m^{-2} in the former. Results of shortwave flux using Fennec-Ryder are not consistent with the GERB/CERES satellite observations (nor with previous estimates of shortwave DRE derived from satellite e.g. Yang et al.

(2009); Ansell et al. (2014)) and I use Dubovik optical properties in the optimum configuration. Recent work suggests that the dust optical properties at BBM in June 2011 were significantly less absorbing than both those measured by the aircraft further west during Fennec, and the Dubovik representation (less absorbing, smaller sized) with SSA values of 0.99 (Rocha-Lima et al., 2017). Therefore, Dubovik optical properties represent intermediate values in terms of SW absorption.

TOA fluxes are not strongly sensitive to the choice of cloud properties with TOA net flux variations of ~4 W m^{-2}. On the basis of bias with respect to observations I select the ERA-I cloud properties.

It is interesting to note that TOA radiative fluxes are quite sensitive to the errors in surface albedo from reanalysis with differences up to 16 W m^{-2} compared to the optimum configuration, which used observed surface albedo. This suggests that it is important to have good observational data, which captures the strong diurnal cycle of surface albedo to achieve accurate radiative fluxes.

The RT model with the above choices of input data is considered to be the 'optimum' configuration, and I validate TOA and surface fluxes with respect to satellite and surface observations, respectively (Tables 4.3 and 4.4) for the most 'realistic' experiment wDwC. The sign convention used here and in the remainder of

Table 4.3. Mean June 08-30, 2011 TOA Radiative flux at BBM (definition of acronyms are given in table 2). Values are in W.m^{-2}. The sign convention is that downward flux is considered as positive while upward flux is negative.

		nDnC	**nDwC**	**wDnC**	**wDwC**
	SOCRATES	328	322	325	321
TOA_SW	GERB	--	--	--	314
	MERRA	312	307	322	317
	ERAI	--	--	336	324
	SOCRATES	-313	-304	-297	-290
TOA_LW	GERB	--	--	--	-276
	MERRA	-314	--	-307	-296
	ERAI	--	--	-309	-294
	SOCRATES	15	18	28	31
TOA_NET	GERB	--	--	--	38
	MERRA	-2	--	15	20
	ERAI	--	--	27	29

the paper is that downward flux is considered as positive while upward radiation is negative. The simulated TOA net shortwave flux is 321 W m^{-2}, compared with 314 W m^{-2} in GERB. It is -290 W m^{-2} for net longwave, with -276 W m^{-2} in GERB, giving 31 W m^{-2} for net radiation, compared with 38 W m^{-2} in GERB, i.e. there is more shortwave heating in the model, with more longwave cooling, giving less net TOA heating. These RT model shortwave/longwave/net (SW/LW/N) biases of 7/-14/-7 W m^{-2} although larger than many of the sensitivity ranges for the input data uncertainties (Table 1) are within the estimated error of the GERB measurements (~10 W m^{-2} for LW and SE flux, Ansell et al., 2014). It is difficult to identify the most important sources of this bias although errors in the reanalysis skin temperature and ERA-I cloud representation included in the wDwC experiment are likely candidates. The DRE of cloud provides a useful comparison and could be considered to be an estimate of the upper limit of cloud-related biases. Cloud DRE (Table 5) is estimated from the difference in fluxes at the TOA between wDnC and wDwC to be -4/7/3 W m^{-2} and from EBFA-CERES to be -15/16/1 W m^{-2}. These results of cloud DRE indicate that the optimum configuration flux biases are within the uncertainties of both observations and cloud effects.

Table 4.4. Same as Table 3 but for surface radiative flux and observation from fennec instrument

		nDnC	**nDwC**	**wDnC**	**wDwC**
	SOCRATES	237	232	192	187
SRF_SW	FENNEC_OBS	--	--	--	180
	MERRA	220	215	190	185
	ERAI	--	--	210	199
	SOCRATES	-138	-134	-106	-103
SRF_LW	FENNEC_OBS	--	--	--	-78
	MERRA	-139	--	-119	-115
	ERAI	--	--	-139	-132
	SOCRATES	99	98	86	84
SRF_NET	FENNEC_OBS	--	--	--	103
	MERRA	82	--	70	70
	ERAI	--	--	71	67

At the surface there is a relatively wider disparity between simulated and observed flux (Table 4). The net shortwave simulated flux, 187 W m^{-2}, is 7 W m^{-2} more than measured surface shortwave flux. Net longwave flux is -103 W m^{-2} compared with that of measurement -78 W m^{-2}, the net effect being more cooling at the surface in the

model than measurement by 25 W m^{-2}. I can again give comparison of cloud related biases between my result and CERES-EBFA product. Cloud SW/LW/N DRE at surface is estimated as -5/3/-2 W m^{-2} from the wDwC-wDnC experiments and -19/11/-8 W m-2 from EBFA-CERES, such that the shortwave bias at least could be explained by cloud but not all the longwave or net radiation bias. The remaining error could be attributable to measurement related errors and uncertainties to other variables such as surface emissivity, skin temperature, and surface albedo. Note also the difference in time averaging periods between the CERES-EBAF data covering whole of June 2011 and the RT experiments wDwC-wDnC covering for 8th-30th June could possibly contribute to part of the differences in the above figures. There is also bias associated with point observation as a representative to a certain grid box given in Satellite measurements which could lead to certain disagreement between in-situ measurements (Schwarz et al., 2017).

Table 4.5. TOA and Surface Direct Radiative Effect of Dust and Cloud

	Dust DRE SOCRATES			**Cloud DRE SOCRATES**			**Cloud DRE EBAF-CERES**		
	SW	LW	NET	SW	LW	NET	SW	LW	NET
TOA	-3	16	13	-4	7	3	-15	16	1
SURFACE	-45	32	-13	-5	3	-2	-19	11	-8

RT model bias in the longwave is larger than that in the shortwave at both TOA and surface. The mean diurnal cycle of flux bias (fig. 4.7) shows that modelled outgoing longwave flux is overestimated at night time. Different factors could be attributed to this difference. Surface skin temperature used in this work is interpolated to 1 hr (Figure 4.6), which could lead to errors in the longwave flux. Satellite observations (see Marsham et al., (2013b)) show over both shallow cumulus cloud at the top of the PBL during late afternoon and occasional moist convection preferentially at night, which may be missed in models given the poor representation of moist convection. This could also contribute to the difference between observed and calculated longwave flux associated with under-representation of cloud in the model.

The RT simulation wDwC captures well the day-to-day variability in radiative fluxes at TOA and surface (fig. 4.8) including the effect of the major synoptic and meso-scale dust/water vapour events e.g. the haboob event of 21st June. However, in the longwave there are significant RT model errors during the night time of 17th and 18th June, which are cases of high dust load following haboob events. Analysis of satellite

imagery shows this anomalous high GERB longwave flux to be coincident with convective cloud development, presumably resulting from the moistening of the Saharan atmosphere, which the RT model, dependent on reanalysis cloud field, cannot capture. This coincidence of dust and cloud is particularly challenging for both GERB cloud screening (which fails in this instance hence my use of all sky observations) and for the RT simulations themselves.

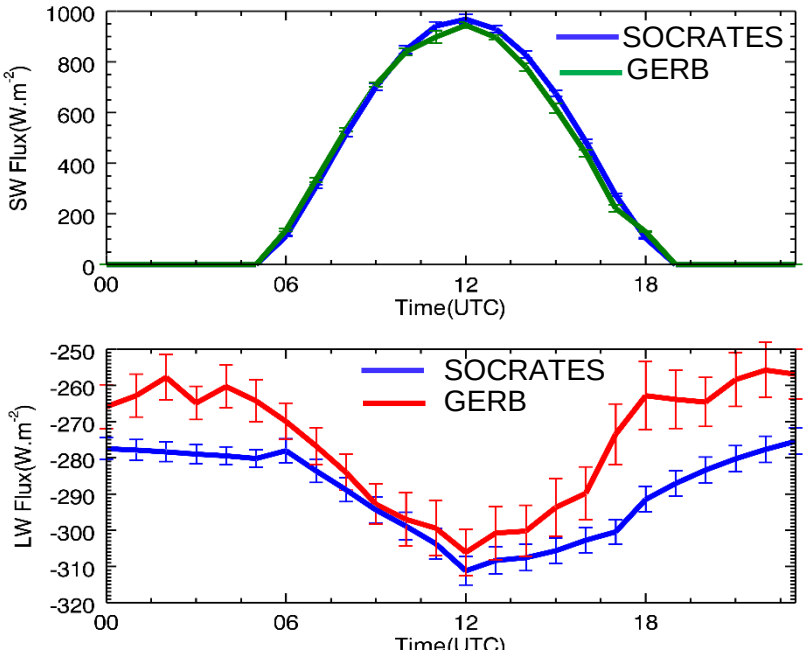

Figure 4.7. Mean Diurnal Cycle of TOA Flux. Blue: SOCRATES wDwC and green: GERB.) The bars show standard error over the diurnal cycle.

I can evaluate my model wDnC experiment results against clear-sky CERES footprint data in which RMSE are 17 W m^{-2} and 12 W m^{-2} for TOA shortwave and longwave fluxes, respectively. The equivalent figures for the model versus GERB (cloud screened using the CERES footprint cloud mask product) at the same times are 22 W m^{-2} and 12 W m^{-2}. These are comparable to and consistent with (i) the individual instrumental errors of CERES/GERB (ii) the inter-sensor uncertainties (CERES vs GERB RMSE = 22 W m^{-2} and 6 W m^{-2} for shortwave and longwave) (iii) previous similar studies (e.g. Osipov et al., 2015).

In summary, RT simulated flux errors of the 'optimum' configuration are comparable to observational uncertainties and those errors introduced by uncertainties in input fields. On this basis I suggest the RT configuration is acceptable for further analysis on the direct radiative effect of dust and water vapour.

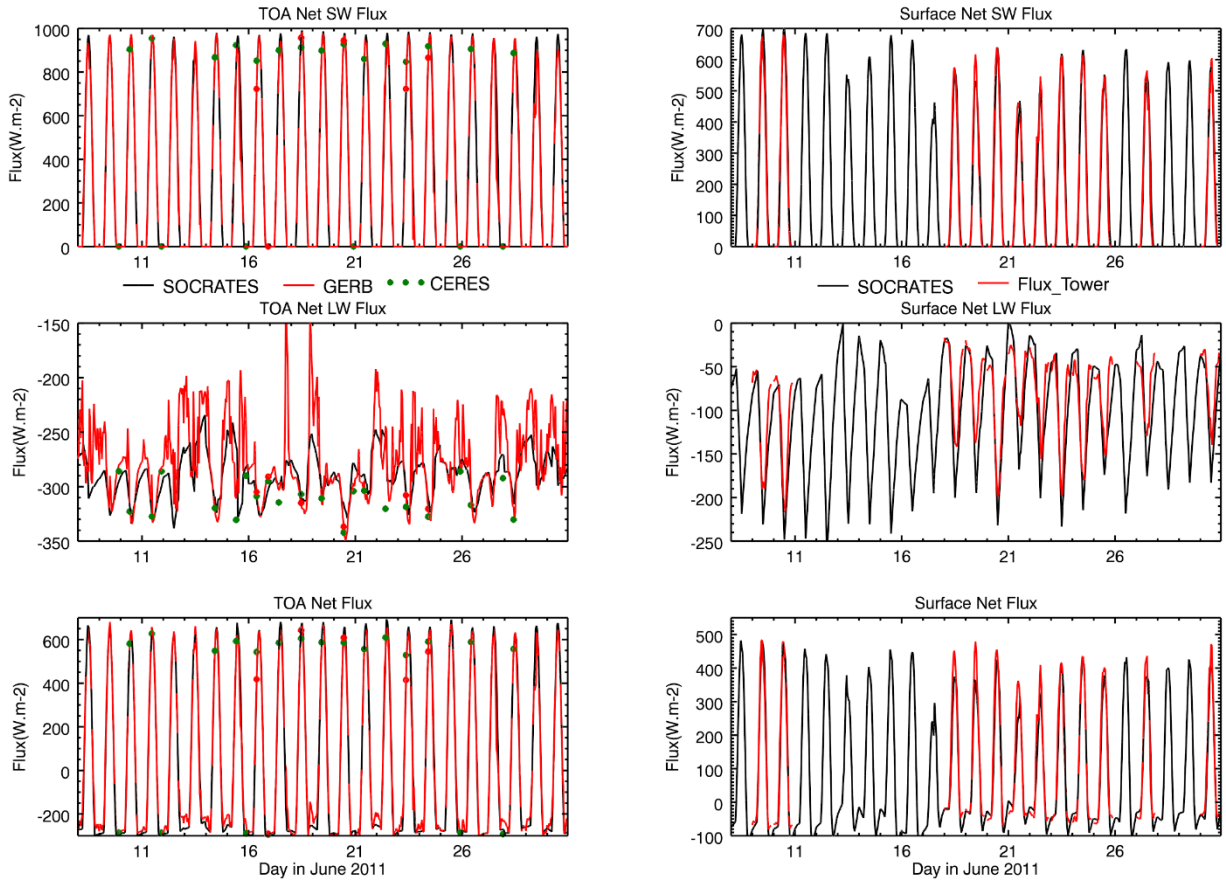

Figure 4.8. Time series of TOA (left column) and Surface (right column) shortwave (SW), longwave (LW), and net Radiative Flux at BBM. Black lines denote SOCRATES outputs, red line denote GERB measurements, green dots denote CERES measurements and red dots denote GERB measurements corresponding to CERES time steps.

4.4.2 The radiative flux and heating effects of dust and water vapour

First, I consider the TOA and surface mean radiative budgets. In the absence of dust and cloud the Saharan atmosphere during summer at BBM shows a positive radiation budget at the surface of 99 W m^{-2} in which shortwave heating of 237 W m^{-2} is offset by longwave cooling of -138 W m^{-2} (Table 4.4). At TOA the shortwave flux of 328 W m^{-2} is not quite offset by longwave losses of 313 W m^{-2} (Table 4.3) leading to a net positive radiation balance of 15 W m^{-2} making the SHL a weak net radiation sink. This strong (weak) radiation surplus at surface (TOA) leads to the atmosphere having a net cooling of 83 W m^{-2} (i.e. radiative divergence), presumably maintained by the transfer

of sensible heat from surface into the atmosphere through turbulent heat transfer (Alamirew et al., submitted).

Both dust and water vapour are known to play an important role in controlling the radiative budget and heating rate of surface and the atmosphere over Sahara. Variability in these two active radiative components is strongly correlated due to the physical processes that govern transport of water vapour and dust emission into the SHL region (Marsham et al., 2013b; M16) such that it is challenging to quantify their separate radiative effects from observations alone. my RT simulations below address this research gap.

4.4.2.1 Dust

Here I determine the DRE of dust using two set of experiments described in Table 4.2. First I compare the simulations of radiative fluxes and heating during June 2011 between the wDnC and nDnC experiments (figs 4.9, 4.10, 4.11, and 4.12 and Tables 4.3 and 4.4). Secondly, I derive the sensitivity of radiative fluxes and heating

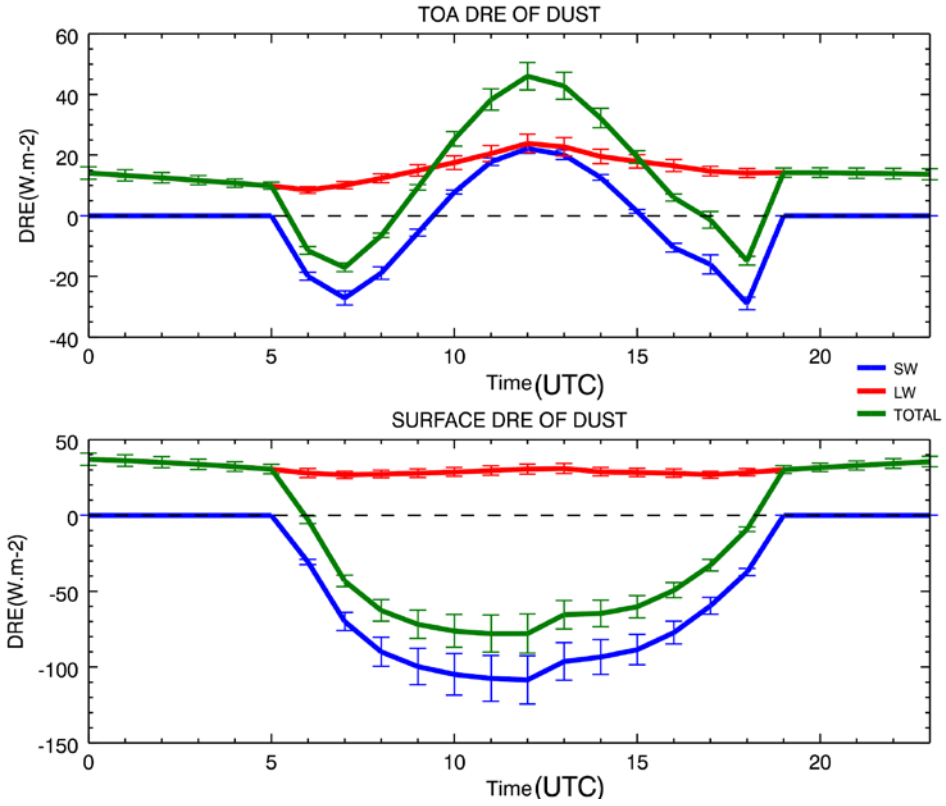

Figure 4.9. Mean Diurnal direct radiative effect of dust averaged for June 08-30, 2016. TOA DRE of Dust (a) and Surface DRE of Dust (b) The bars show standard error over the diurnal cycle.

rates to a wide range of dust AOD using the sensitivity experiments. I then compare my estimates of dust DRE to those from previous studies.

The mean SW/LW/N DRE of dust at TOA for June 2011 estimated from wDnC minus nDnC is -3/16/13 W m^{-2} confirming the net warming effect of dust over the Sahara. This warming comes primarily in the longwave with a peak at ~24 W m^{-2} close to midday (fig. 4.9a). The net shortwave DRE is small, consistent with other estimates (Huang et al., 2014;Yang et al., 2009). However, with a pronounced diurnal structure driven by a semi-diurnal cycle in the shortwave with a cooling effect of up to -29 W m^{-2} after dawn until 10:00 and after ~16:00 until sunset, and a warming effect of up to ~22 W m^{-2} around midday (fig. 4.9a). The diurnal cycle of dust DRE is not strongly dependent on the amount of dust loading in the atmosphere but controlled by solar zenith angle and surface albedo (Ansell et al., 2014; Banks et al., 2014). The phase function also exerts a control on the diurnal cycle of the DRE as its value increases the backscatter fraction of SW radiation at large solar zenith angles. For comparison, the equivalent TOA SW/LW/N DRE of dust for MERRA reanalysis are 10/7/17 W m^{-2} suggesting that although MERRA has a good estimate of net DRE but the apparent shortwave warming effect is not in agreement with observations and the longwave warming is underestimated.

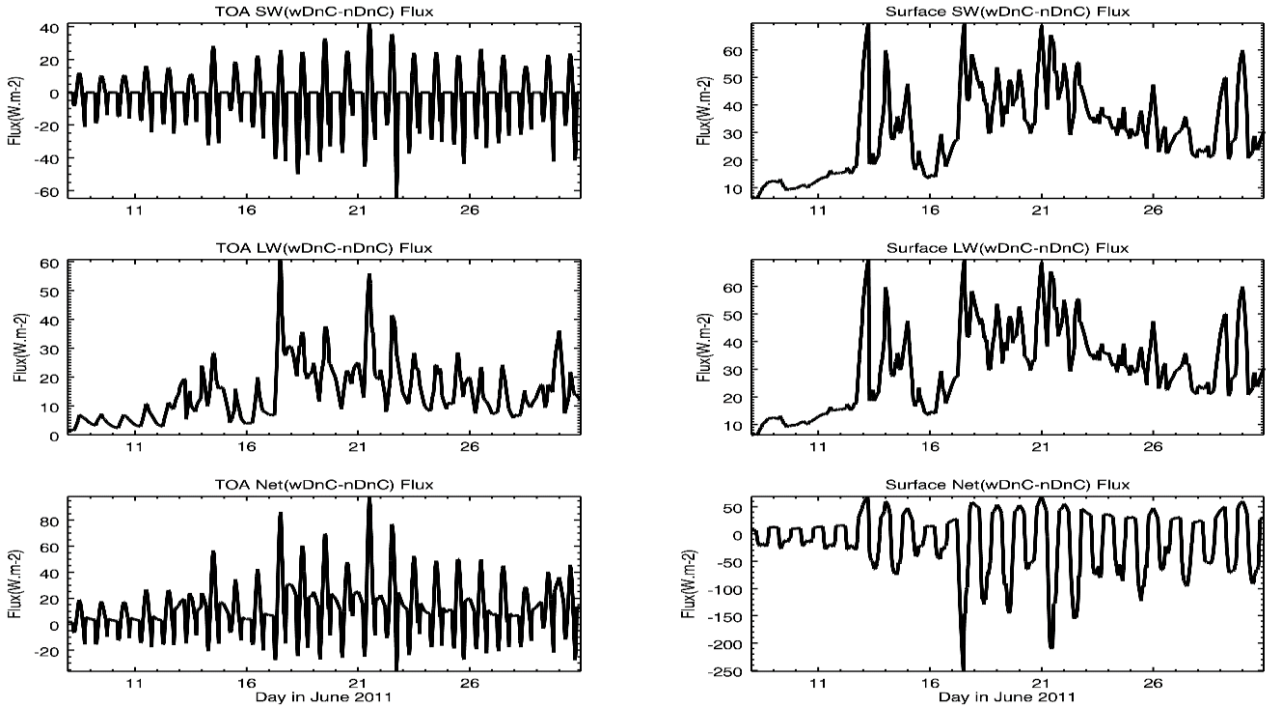

Figure 4.10. DRE due to Dust: time series of TOA shortwave (a), longwave (b), net (c) and surface shortwave (d) longwave (e) and net (f) wdnC-nDnC flux

At surface SW/LW/N DRE of dust is estimated to be -45/32/-13 W m^{-2} for SW/LW/N (Table 4.5). Net cooling is driven by shortwave flux peaking at ~-108 W m^{-2} around noon (fig. 4.9b) partly compensated by a longwave heating effect, 32 Wm^{-2}. MERRA reanalysis DRE at surface is -30/20/-12 W m^{-2} again showing a good estimate of net effects but underestimating the shortwave and longwave components. Time series of shortwave DRE of dust (fig. 4.10a) at TOA further confirms the diurnal cycle discussed above: a midday warming and early morning and late afternoon cooling. The impact of big dust events (e.g. June 17th and 21st) can be clearly seen on the time series of longwave DRE of dust (Figure 4.11b).

The results of sensitivity experiments 'senDnC' are shown in fig. 4.11 and the DRE per unit AOD and per unit standard deviation in AOD is presented in Table 4.6, assuming a linear relationship between flux and AOD. I find the net TOA shortwave

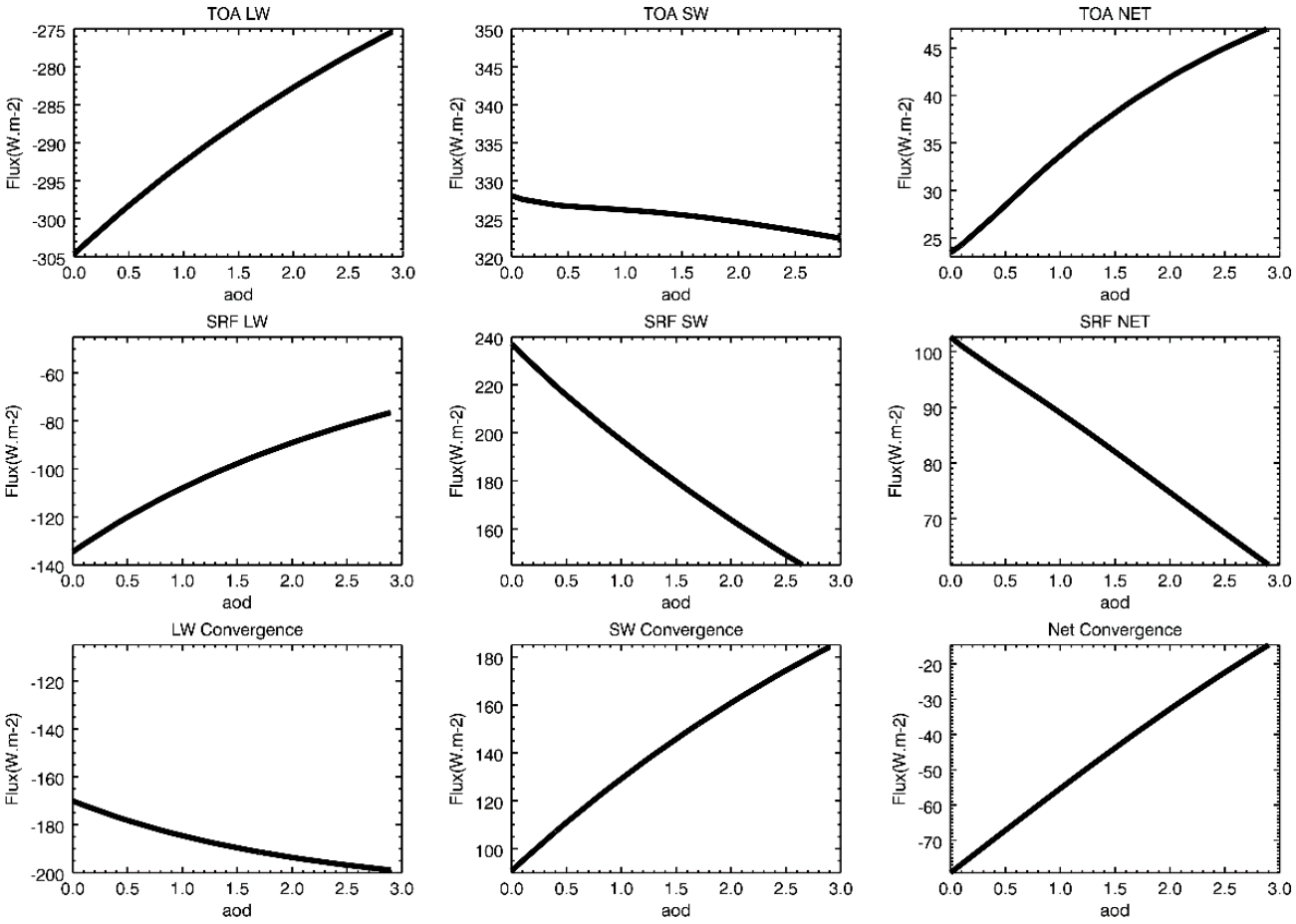

Figure 4.11 Radiative budget as a function of dust AOD. Top row (a, b, c): TOA longwave (a), shortwave (b), and net (c). Second row (d, e, f): similar to top row but for surface. Third Row: atmospheric radiative convergence of longwave (g), shortwave (g), and net (i)

flux to be only weakly sensitive to dust AOD (fig. 4.11d) at -2 W m^{-2} per AOD. This is due to the competing dust effect of (i) increasing albedo which decreases net TOA shortwave and (ii) absorption by dust which increases TOA net shortwave by reducing the upwelling shortwave radiation. My estimates of shortwave dust DRE is less than half the sensitivity reported at BBM by M16, but consistent with the Sahara-wide estimates from satellite of Yang et al., (2009) and those of Ansell et al., (2014).

Dust in the atmosphere acts to reduce the outgoing longwave flux by 10 W m^{-2} per unit increase in AOD (Figure 4.11a), warming the surface, consistent with the observations at BBM of M16 (11 W m^{-2} per AOD increase) and within the Sahara-wide range of Yang et al., (2009). At the surface dust has opposing effect in shortwave and

Table 4.6 Sensitivity of Radiative Flux to Dust AOD and CIWV at selected altitudes. SD*=Standard Deviation (0.8 for AOD and 5.5 g.kg^{-1} for water vapour. Mean AOD = 1.2 and mean column integrated water vapour = 27.8 Kg m^{-2})

Change in Flux		**SW**	**LW**	**NET**
per unit AOD (W m^{-2})	TOA	-1.8	10.0	8.2
	Surface	-33.8	19.8	-14.0
	Convergence	32.1	-9.7	22.4
per unit CIWV (W Kg^{-1})	TOA	0.3	1.1	1.4
	Surface	-0.4	1.6	1.2
	Convergence	0.8	-0.5	0.3
per one AOD SD* (W m^{-2})	TOA	-1.4	8.0	6.6
	500hPa	-6.2	10.6	4.4
	700hPa	-14.8	11.6	-3.2
	Surface	-27.0	15.8	-11.3
	Convergence	25.7	-7.8	17.9
per one CIWV SD*(W Kg^{-1})	TOA	1.7	5.8	7.5
	500hPa	-0.4	9.3	8.9
	700hPa	-1.6	9.4	7.9
	Surface	-2.4	8.3	5.9
	Convergence	4.0	-2.8	1.3

longwave, with shortwave having stronger cooling effect: for every unit increase in AOD there is shortwave reduction of 34W m^{-2} (fig. 4.11e, Table 4.6) compared to increase in longwave (fig. 4.11b) with 20 W m^{-2} the net effect (fig. 4.11h) being cooling of -14 W m^{-2} per AOD increase.

Dust drives radiative convergence in the atmosphere i.e. the difference in TOA minus surface flux, which acts to warm the atmosphere. This occurs through greater shortwave absorption, at a rate of 32 W m-2 per AOD (fig. 4.11f) offset partially by longwave cooling the atmosphere at -10 W m^{-2} per unit AOD increase, leading to a net warming effect of 22 W m^{-2} per unit change in AOD. Overall, the RT estimates of TOA and Surface DRE in the shortwave and longwave and the atmospheric radiative convergence are within a few W m^{-2} of those of M16 derived from observations.

I convert the radiative fluxes to actual heating rates (fig. 4.12a). In the absence of dust (nDnC experiment) the PBL is heated in the shortwave mainly from absorption by O_2 and water vapour peaking up to ~1.3 K day^{-1} at 450 hPa (the water vapour effect is shown in Figure 4.15). Strong longwave cooling throughout the troposphere (up to ~-3 K day^{-1} at ~450 hPa) due to emission from water vapour and other greenhouse gases exceeds this shortwave heating, leading to tropospheric radiative cooling of ~-0.6 K day^{-1} throughout the PBL. This is consistent with the radiative heating I estimated of Chapter III, derived as a residual of the heat budget.

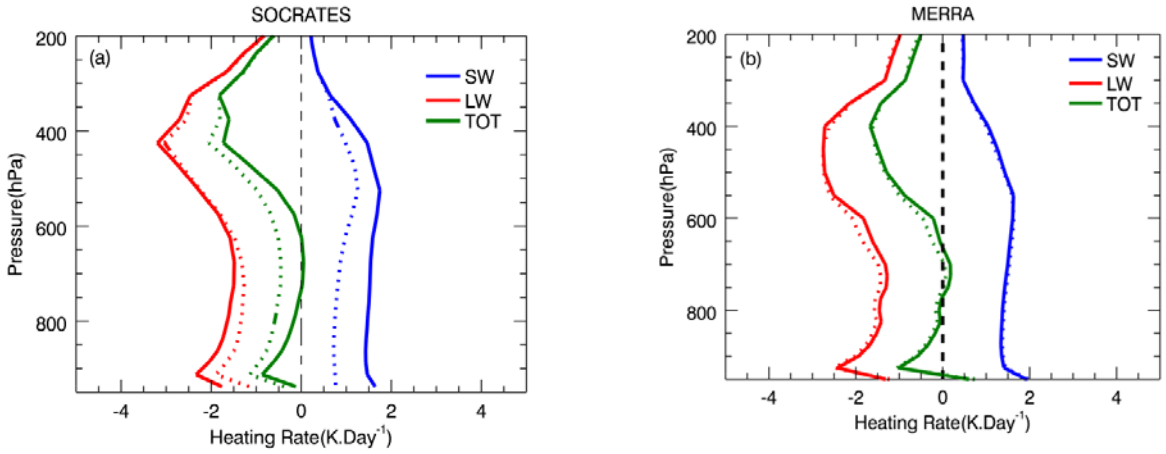

Figure 4.12. Mean Radiative Heating Rate Profile for June (08-30, 2011) at BBM a: Results from nDnC (dashed lines) and wDnC (solid lines) using FENEC profile and b: MERRA Model output for all sky (solid lines) and clear sky (dashed lines) conditions. Blue, red, and green colours represent shortwave, longwave, and total heating rates respectively.

In the lowest near surface layer (below 925 hPa) there is less longwave cooling due to strong radiative flux from the hot desert surfaces in the SHL. Dust acts to modify the vertical structure of this radiative heating/cooling considerably. Absorption of shortwave radiation leads to a strong warming effect in the shortwave (especially in the dusty PBL up to ~0.75 K day^{-1} below ~700 hPa, where dust loadings are the highest), offset only partially by enhanced longwave cooling (up to ~-0.25 K day^{-1}) resulting in a net warming of the atmosphere by up to ~0.5 K day^{-1} at ~700hPa, such that the dusty troposphere above ~600hPa has near zero cooling. For comparison I consider the MERRA reanalysis product mean heating rate (fig. 4.12b), which includes both cloud and climatological dust, is in close agreement with those of the wDwC experiment. However, MERRA does not capture the day-to-day variability in shortwave heating from dust and will not therefore be able to simulate the responses of the SHL atmosphere to variability at these timescales. Further weather/climate model simulations are required to determine the effect this has on the regional circulation and the behaviour of the SHL.

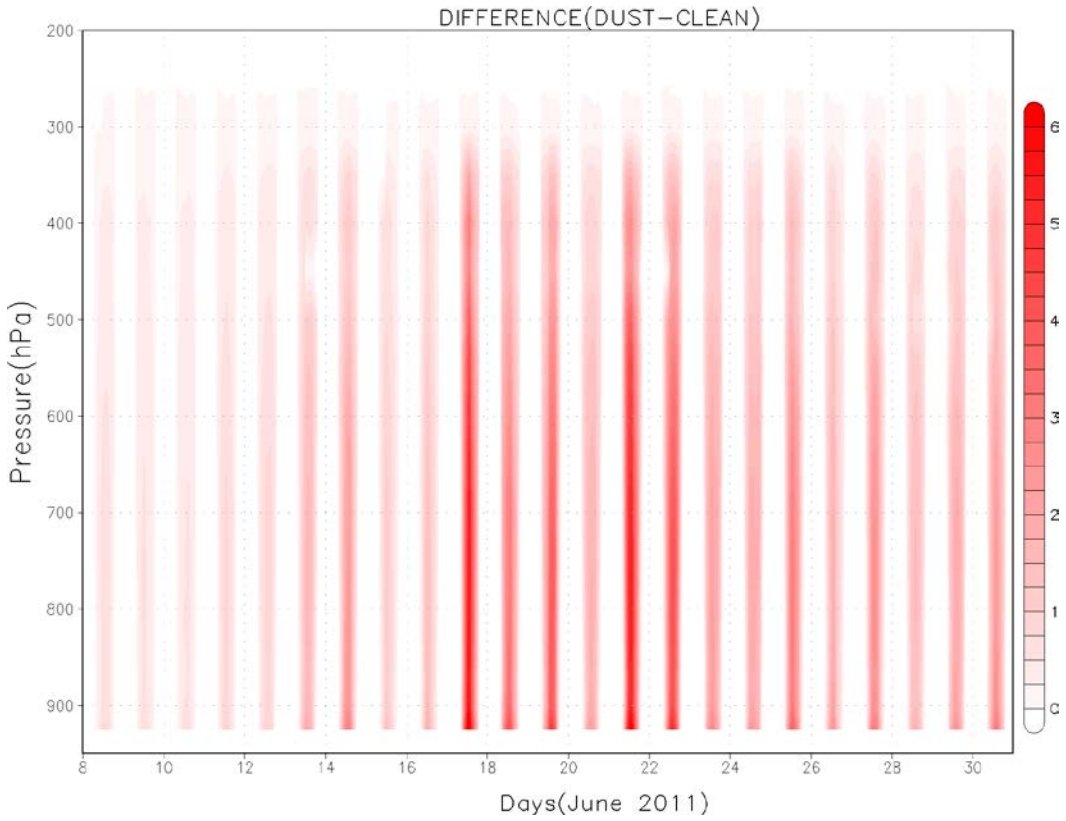

Figure 4.13 Radiative Heating rates (K.Day^{-1}) of dust in the atmosphere (DUST represents wDnC runs and CLEAN represents nDnC runs)

Day-to-day variability in the dominant shortwave net heating rate (fig. 4.13) is pronounced and shows the impact of the synoptic/meso-scale dust events on the SHL atmosphere. During large dust events (e.g. June 17th and 21st) there is strong shortwave heating up to 6 K day^{-1} around midday hours. This will be coincident with reduced surface net radiation and sensible heat flux. Together these processes will act to reduce the vertical temperature gradient, stabilise the atmosphere, reduce dry convection and reduce the depth of the PBL.

4.4.2.2 Water vapour

To estimate the heating rate profiles due to water vapour, I selected from the simulation nDnC three driest days (June 11, 12, and 16) with mean column integrated water vapour of 20.2 Kg m^{-2} and three most humid days (June 18, 25, and 30) with mean column integrated water vapour of 34.7 Kg m^{-2}. The mean heating rate profiles for the two contrasting atmospheric conditions is shown in fig. 4.14. High humidity drives an increase in the shortwave heating rate up to 0.5 K day^{-1} peaking near the surface. This atmospheric warming is counteracted by a slightly bigger cooling in the longwave. Thus there is a net cooling up to -0.25 K day^{-1} in the atmosphere and strong heating up to 2.5 K day^{-1} near the surface as a result of increase in moisture. The atmospheric cooling in the longwave causes surface warming, which is suggested to be linked with the intensification of the Saharan heat low region (Evan et al., 2015b). The reversed heating rate profiles in the layer between 500 hPa and 400 hPa is because of the mean moisture profile in this layer is larger during the dry days and the vice versa (fig. 4.1).

Results from the water vapour sensitivity experiments ‘senWVwDnC’ are presented in fig 4.15 and the linear dependence on fluxes per unit water vapour in Table 4.6. The outgoing longwave radiation (fig. 15a) decreases with increasing of water vapour at a rate 1 W kg^{-1} which is associated with the greenhouse effect of water vapour. This is about a third of that derived by M16 (3 W kg^{-1}). Their result, however includes the effect of water vapour and associated dust and cloud while my result considers sensitivity of radiative flux to changes in water vapour only. The sensitivity of TOA shortwave flux due to water vapour (fig. 15d) is 0.3 W kg^{-1} which warms the atmosphere and to the contrary cools the surface due to the reduction of the shortwave reaching the earth. M16 showed that a reduction in the TOA shortwave radiation with increasing of water vapour, of -0.98 W Kg^{-1} which is contrary to what I find in my results. But this could be related with the impact of cloud on the shortwave radiation

which will reduce the TOA net shortwave radiation. The net flux at TOA increases by to 1.4 W m^{-2} for a unit change in CIWV resulting in a net warming of the TOA.

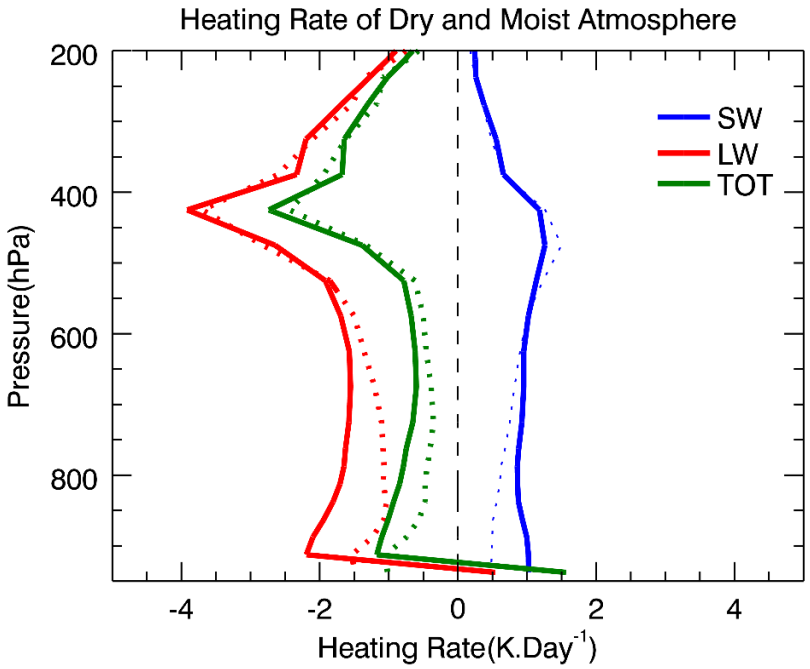

Figure 4.14 Atmospheric heating rate profile for selected dry days, June 11, 12, and 16 (dashed lines) and moist days, June 18, 19, and 25 (solid lines)

The net flux reaching the surface (fig. 15h) is increased at a rate 1.1 W Kg^{-1} which is the counteracting effect of a dominant increase in longwave radiation re-emitted downwards from the atmosphere (1.5 W Kg^{-1}) and a smaller reduction in downwelling solar radiation (-0.4 W Kg^{-1}). The warming effect of water vapour at both the surface and the TOA means that net atmospheric convergence changes relatively little with water vapour (fig. 15i) at 0.1 W Kg^{-1} which is a result of -0.6 W Kg^{-1} in the longwave (fig. 15c) and 0.7 W Kg^{-1} in the shortwave (fig. 15f). In comparison to the observational analysis of M16 I see some important differences, notably I see a greater surface net warming effect of water vapour and as a result negligible, not positive atmospheric radiation convergence. Nevertheless my estimate of the sensitivity of surface longwave radiation to changes in CIWV of 1.1 W Kg^{-1} is at the lower end of the range (1.0-3.6 W Kg^{-1}) estimated by Evan et al., (2015b), from observations and RT simulations, suggesting the role of water vapour in driving longer term inter-annual to decadal heating of the SHL may not be as pronounced as previously suggested.

4.4.2.3 The relative effects of dust versus water vapour

From the sensitivity experiments, I can quantify the DRE of dust and water vapour at TOA and surface per unit change in AOD of dust and kg m^{-2} of ClWV respectively (Table 4.6). By scaling this to observed standard deviation in each variable observed during the Fennec observation period I provide estimates of the relative importance of dust and water vapour to the day-to-day variability in the radiation budget over the SHL.

The resulting normalised dust SW/LW/net DRE per AOD at TOA and surface is -1/8/7 W m^{-2} and -27/16/-11W m^{-2} respectively, where these figures provide a useful way of presenting the variability of dust and water vapour on their radiative effects. The equivalent values for water vapour are 2/6/8 W m^{-2} and -2/8/6 W m^{-2}. As such, the radiative effects of dust and water vapour at TOA are of similar magnitude with net warming of ~7 W m^{-2} per unit variability. Dust and water vapour exert similar control on the total heating of the Earth-atmosphere. This contrasts with M16 who report water effects (from vapour and cloud) as ~3 times more powerful than dust.

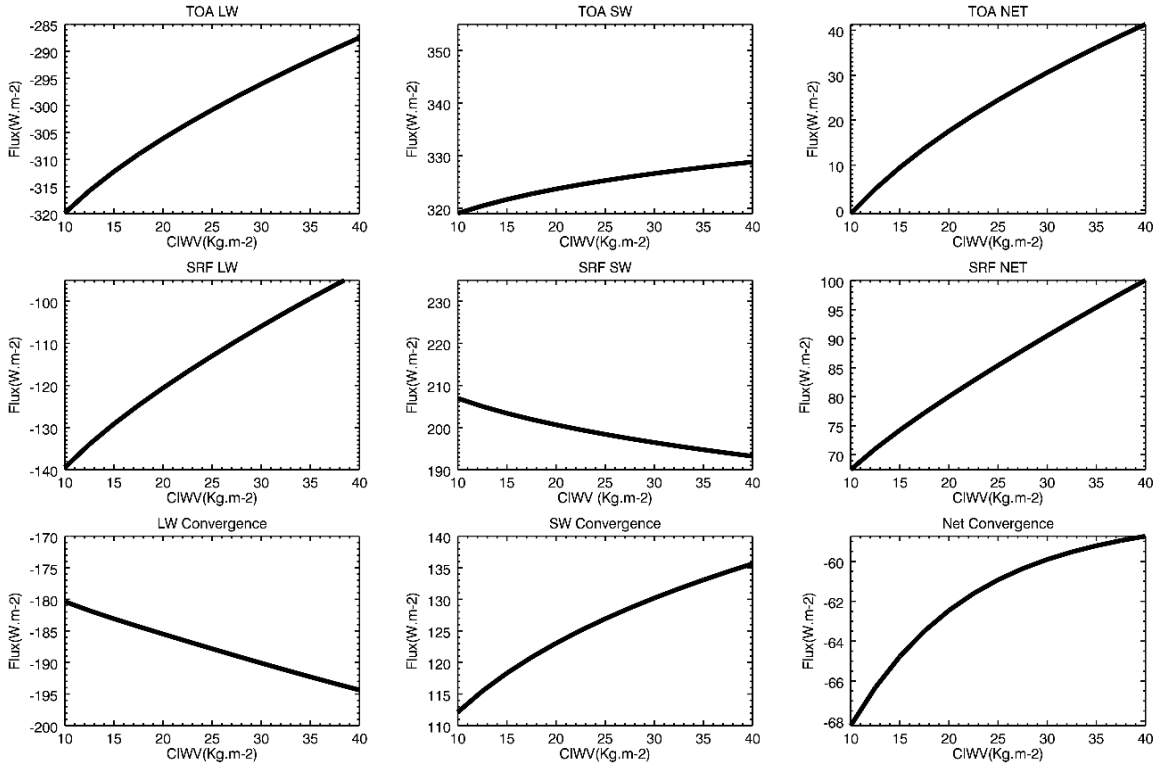

Figure 4.15. Same as **Figure 4.11** except for column integrated water vapour.

At the surface radiative flux is controlled much more strongly by dust than water vapour and with opposite sign: net cooling of -11 W m^{-2} and warming of 6 W m^{-2} per

unit variability respectively. M16 find near zero warming from water (vapour and cloud). In my study the net effect of TOA versus surface is strong atmospheric warming of 18 W m^{-2} per unit variability from dust and negligible warming (1 W m^{-2} per unit variability) from water vapour. In contrast, M16 find almost equal warming from dust and water vapour (of 11-12 W m^{-2} per unit variability). Although this radtiative transfer based analysis of the role of water vapour does not include the cloud that is implicitly included in M16, I suggest that the co-variability of dust and water vapour hinders calculation of their independent effects in the observational analysis of M16.

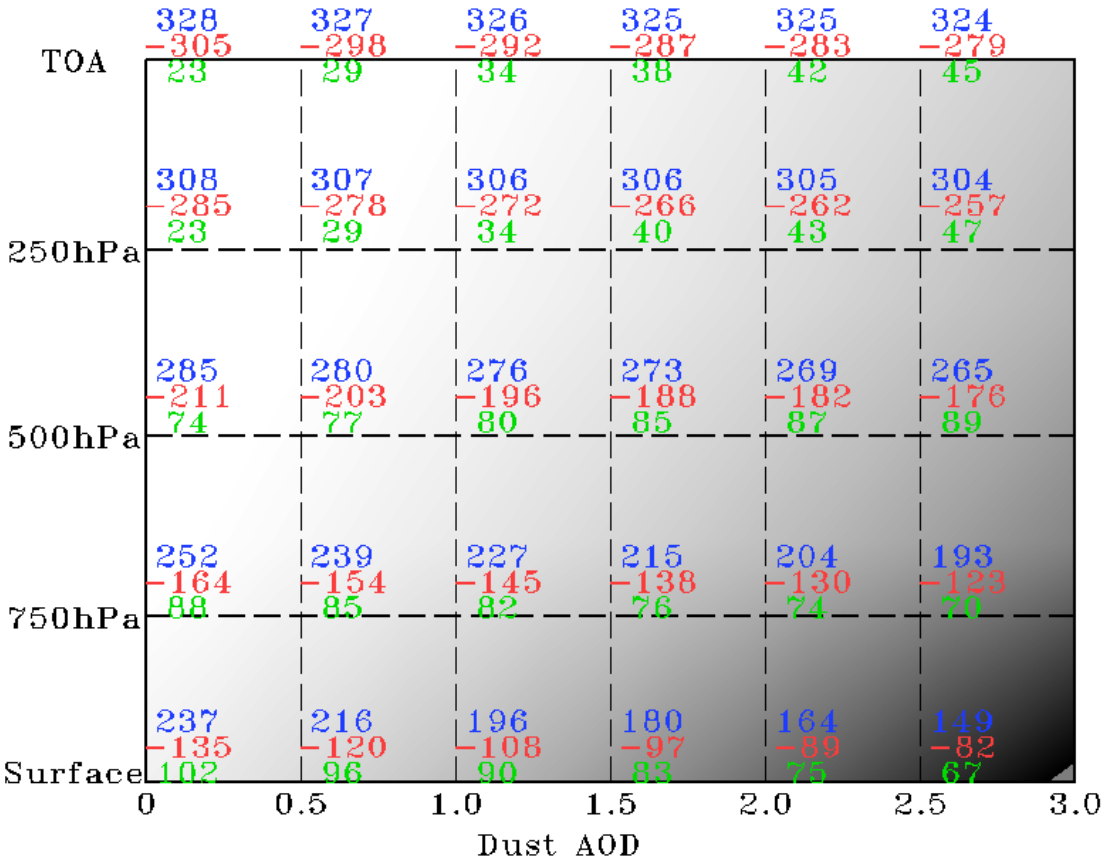

Figure 4.16 Sensitivity of Radiative Flux (W.m^{-2}) to changes in dust AOD. The numbers at each pressure level are downward shortwave (blue), longwave (red), and net (green) flux. The grey shade represents dust and water vapour amount in the atmosphere

In summary I find that dust and water vapour exert a similarly large control on TOA net radiation and therefore total column heating and by implication to the first order similar control on surface pressure in the SHL. However, the vertical structure of radiative heating from dust is far more complex than that for water vapour. The schematic, fig. 16 illustrates the sensitivity of dust and water vapour at different

pressure levels. Dust imposes a strong net cooling at the surface from the SW which declines to zero at ~700hPa, where SW cooling and LW warming balance, with net warming above this (Table 4.6). In contrast water vapour imposes a LW heating effect that varies relatively little from surface to TOA. As such dust is likely to have stronger impact on the structure and processes of the SHL atmosphere than does water vapour.

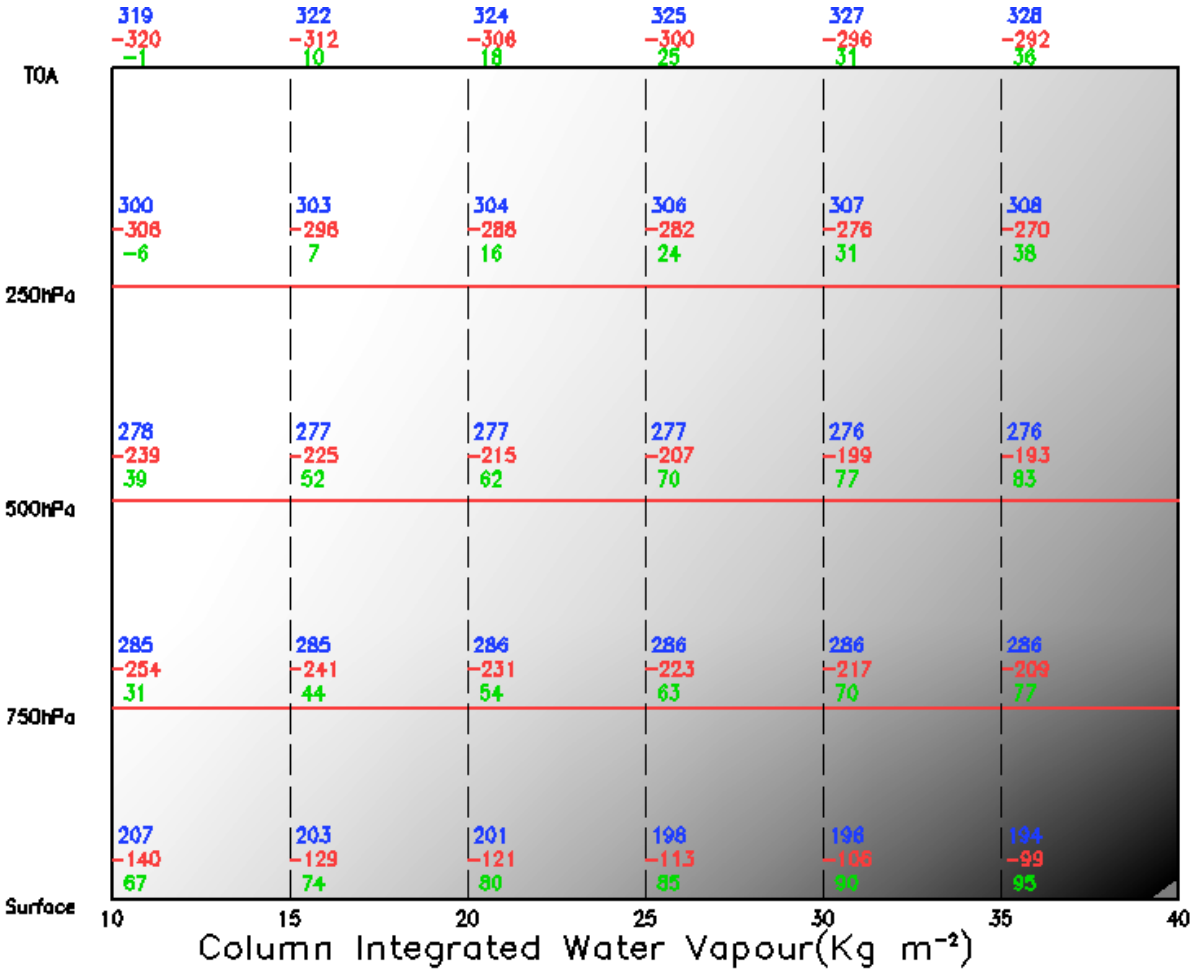

Figure 4.17. Same as fig. 4.16 except for CIWV

4.5 Summary and Conclusions

The summertime Saharan Heat Low feature is of considerable importance to the wider regional climate over West Africa but remains poorly understood. To the first order the SHL is created by strong sensible heat flux from the surface radiative surplus which heats the deep Saharan boundary layer, which is in near balance with advective cooling from the low level convergence circulation (see Chapter III). However, radiative

heating is modulated by water vapour and dust whose variations, at least at short timescales, are correlated. Here, I aim to quantify the independent radiative effects of dust and water vapour, and atmospheric heating rates using an RT model. The model is configured for the location at BBM, close to the heart of the SHL using inputs from Fennec field campaign for June 2011. First, sensitivity to uncertainty in RT model inputs fields is assessed. I find that dust size distribution is the most important source of uncertainty in this case, through its impact on single scattering albedo. The RT model when suitably configured has radiative flux biases at TOA that are within observational uncertainties and input uncertainties. The subsequent RT experiments show:

1. On average the SHL has a large positive radiative surplus at surface of 83 W m-2 , a small surplus at TOA of 31 W m-2 with a net atmospheric radiative divergence of 52 W m-2 presumably approximately balanced by the transfer of sensible heat.

2. The effect of dust is pronounced:

    I. During June 2011 dust had a positive DRE at TOA of 8 W m^{-2} per unit AOD (7 W m^{-2} per unit AOD variability) almost entirely in the longwave, as the effects of shortwave absorption with respect to surface albedo largely balance, acting to warm earth-atmosphere system as a whole, with magnitude consistent with previous studies (Banks et al., 2014; M16; Yang et al., 2009).
    II. Dust has a strong negative DRE at the surface of -14 W m^{-2} per unit AOD (-11 W m^{-2} per unit AOD variability) largely due to reduced shortwave flux from atmospheric absorption.
    III. The net effect of this negative surface DRE and positive TOA DRE is considerable atmospheric radiative convergence of 22 W m^{-2} per unit AOD (18 per unit AOD variability) largely from shortwave absorption. This directly heats the PBL below ~500hPa by ~0.6 K day^{-1}.
    IV. Dust loading is variable and the heating effect of episodic synoptic and meso-scale dust events can be up to 6 K day^{-1}.

3. The effect of water vapour is weaker than dust at the surface and includes:

    I. a positive radiative effect at TOA of 1.4 W m^{-2} per unit column integrated water vapour (8 W m^{-2} per unit water vapour variability) almost entirely a longwave greenhouse effect.
    II. weak positive radiative effect at the surface of 1.2 W m^{-2} per unit column

integrated water vapour (6 W m^{-2} per unit water vapour variability) almost entirely from longwave radiation re-emitted downwards.

III. positive radiative effects at surface and TOA and thus a negligible impact on atmospheric radiative convergence.

A key finding here is that in contrast to previous analysis dust and water vapour are roughly equally important at the TOA, in controlling day-to-day variability in heating the earth-atmosphere system as a whole, (in contrast to M16 who identify water and associated cloud as the key driver), but that dust variability dominates variations in surface and atmospheric radiative heating. The biggest single net radiative effect in this study is the atmospheric radiative convergence from dust. The impact of dust may therefore be greater than previously believed. Recent studies have proposed a water vapour positive-feedback mechanism driving decadal variations in SHL intensity, implicated in the recent recovery of Sahelian rainfall (Evan et al., 2015b). My results are consistent with this but strongly suggest that variability in dust loading should be considered in explaining variability and change in the SHL, reinforcing the need for high quality long term aerosol observations. Additionally dust size distributions, shape and chemical composition are spatially and temporally variable, and the vertical profile of dust will vary with meteorological conditions – thus introducing more variability and uncertainty than has been explored in this study. These variations potentially increase the controls of dust on the radiation budget even further than quantified here.

Therefore, water vapour events in themselves act to heat at the TOA and at the surface and presumably intensify the SHL. In contrast, dust events cool the surface but warm the lower troposphere as a whole, such that the net effect at the top of the Saharan residual layer (about 5km) is a warming which will intensify the SHL. Various climate model experiments also demonstrate this effect (Mulcahy et al., 2014). I can then consider the effects of variability in SHL associated with monsoon surges and haboobs in which dust and water vapour increases are often coincident. Through radiative processes such events act to (i) warm the whole troposphere, almost equally through dust and water vapour longwave effect (ii) strongly cool the surface from dust shortwave effect, and more weakly warm the surface through water vapour longwave effects. Although these counteracting effects mean the net surface radiative flux reduction is actually quite small, the diurnal effects are pronounced with the dust shortwave apparent in daytime and the water vapour effect dominant at night, which will act to reduce the sensible heat flux into the atmosphere limiting the vertical development of the SHL PBL (iii) Substantial radiative heating from dust occurs in the PBL up to 6 K day^{-1} through dust shortwave absorption. This will act to stabilise the

PBL with implications for dry and moist convection, although (Trzeciak et al., 2017) suggest that moistening may often counter this. Such events typically involve an additional advective cooling which can be substantial up to 2-5 K day^{-1} for monsoon surges (Couvreux et al., 2010) but is restricted to the lowest layers (~1 km from surface).

Couvreux et al. (2010) suggested a negative feedback process within the SHL-monsoon systems that may govern preferred 3-5 day timescale of variability in the SHL and monsoon pulses. Strong net radiative heating at the surface intensifies the SHL, enhancing monsoon surges which then, through low level advective cooling, act to weaken the SHL, before solar heating restores the SHL. My results add potentially important detail regarding the radiative role of dust and water vapour that may modify this conceptual understanding. First, the net effect on surface radiation of dust and water vapour together is to further cool the surface and weaken the SHL, in addition to the advective cooling. Second, this weakening of the SHL is offset because the magnitude of dust radiative heating in the lowest layers is comparable to that of advective cooling so that net effect may be small or even positive, but with the dust radiative heating extending throughout the entire PBL above, rather than just the lowest 1km or so. Third, the timescale of re-establishment of the SHL through surface heating and sensible heat flux may be influenced by the rate of dust deposition and export, which, depending on the synoptic context may be 1-2 days, though sometimes dust remains suspended in the SHL for days -weeks. The net effect of these, often competing, processes on the SHL will depend on the precise nature of water vapour, dust and temperature advection during such monsoon surge events. As such, SHL variability will represent a complex interplay of factors rather than a feedback through a single mechanism. There is a clear need for much better spatially extensive and detailed observations of all these variables

I can therefore envisage an inherent tendency for pulsing in the SHL in which an intensifying SHL will lead towards monsoon surges, which act through near surface/low level radiative and advective cooling to weaken the SHL and through dust-radiative heating to stabilise the PBL, until dust deposition and export allow re-warming of the surface to re-invigorate the SHL. Given the radiative effects described above the dynamical effects of dust variability on the low level convergence and mid-level divergence circulations will be greater than those of water vapour and require further model experiments to resolve. Whilst reanalysis models represent well the average radiative and heating effect of dust and water vapour they do not capture dust and water vapour variability well and the subsequent dynamical effects on the larger scale circulation.

The unique observations of the Fennec aircraft campaign suggested that fresh dust is much coarser than previously believed (Ryder et al., 2013b), with corresponding higher absorption, and this has significant impacts on the radiation budget (Kok et al., 2017). My RT model simulations results suggest that such a dominant coarse mode is not consistent with TOA radiative flux observations at BBM. However, if dust is coarser than I assume here then the radiative effects of dust would be even stronger. Further observations on dust size distribution and optical properties are a priority requirement. In addition, further work should consider in much greater detail the radaitive effects of cloud based on detailed observations rather than the rather coarse estimates from reanalysis used here.

It is worth mentioning at this point that spatial and temporal representativeness of satellite observations should be considered when comparing with point surface measurements. Schwarz et al. (2017) showed the correlation between surface measurement and satellite derived surface solar radiation decreases linearly with increasing distance between surface observations leading to errors up to 8 W m^{-2}. I have not taken this into consideration in my results. Radiative flux measurement should however take this into consideration to get results with improved accuracy.

Our results showing the complex interplay of dust and water vapour on surface and PBL radiative heating stress the need for improved modelling of these processes over the SHL region to improve predictions including those for the WAM across timescales (e.g. Evan et al., 2015b). Most models currently struggle in regard to short term variability in water vapour (Birch et al., 2014;Garcia-Carreras et al., 2013;Marsham et al., 2013a;Roberts et al., 2015), (Roehrig et al., 2013;Stein et al., 2015) and dust (Evan et al., 2014), with many dust errors coming from moist convection (Heinold et al., 2013; Marsham et al., 2011). Forecast models typically have mean biases of up to 2 kg m^{-2} in column integrated water vapour (equivalent to change in 2.6 W m^{-2} TOA net flux) and lack variability in dust, and so are expected to poorly represent these couplings. A focus on improved representation of advection of water vapour, clouds and convection in models should be a priority.

CHAPTER V

5. Characterising Cold Pools from Observations and their implication to amount of water vapour over the Saharan Heat Low

5.1 Introduction

Cold pools are prevalent features of the Saharan desert and are important component of the climate system of the region. Cold pools primarily triggered from the WAM in the south (Marsham et al., 2013a) and Atlas Mountains in the north (Knippertz et al., 2009) play significant role in the transport of moisture towards the central Sahara heat low. For instance (Cuesta et al., 2010) discussed the impacts of increase in low level moisture from meso-scale convective cold pools associated with the WAM on the precipitating cloud over the Hoggar. Similarly Marsham et al. (2013a) showed cold pools play significant role in the advection of moisture to the heart of the Saharan desert. It is also indicated that mesoscale convective cold pools over the Sahel has influence in the northward displacement of the ITD (Flamant et al., 2009). Moreover cold pools are shown to play significant role in the emission of dust over Sahara region. Allen et al., 2013 identified a total of 20 cold pool outflow events which are attributed to 45% of dust emission locally at Bordj Badji Mokhtar (BBM) in Algeria during the FENNEC intensive operation period in June 2011. In a related study, (Heinold et al., 2013) used an off line dust emission model applied to convective permitting simulations and showed that cold pools are attributed to 40% of dust emission over the Saharan desert. In a more recent study (Trzeciak et al., 2017) further highlighted the importance cold pools for moisture transport, dust and cloud. Despite their proven significance in the transport of moisture and emission of dust in the Sahara desert, their exact contribution is not well known.

The theoretical framework via which cold pools are formed is well known (Charba, 1974;Simpson, 1969). However it is still challenging to accurately reproduce them in climate models mainly due to models struggle to accurately simulate convection. Relatively coarse resolution models with parametrized convection have limited ability to capture cold pools while models with higher resolution struggle to accurately simulate convective triggered cold pools on the right place and at the right time (Heinold et al., 2013;Knippertz et al., 2009;Marsham et al., 2013a). In order to better represent regional surface and boundary layer processes in models, and thus improve simulation of convection and related processes, it is imperative to understand the characteristics of such convective triggered density currents. A number of

observational analysis have been made to characterise cold pools over different locations: in the United States (Engerer et al., 2008), in the southern Arabian Peninsula (Miller et al., 2008), in the southern foothills of the Atlas mountains (Emmel et al., 2010;Redl et al., 2015), and in Niger, Niamey (Provod et al., 2016). Here I present characteristics of summertime convective triggered cold pools occurring over a wider domain in the Sahara desert. As such I present the occurrence frequency, spatial and seasonal distribution cold pools that occurred in the Sahara desert.. Redl et al. (2015) presented characteristics of cold pools using multi-year AWS data in the southern foothills of Atlas Mountain. To the best of my knowledge there is no such previous studies in the central SHL region. Lack or scarcity of observational data required for a comprehensive characterization and analysis of cold pools in SHL region is partly a problem. Fennec AWS data provides an opportunity to make an in depth study on the properties of these common atmospheric processes over the central Sahara region.

This chapter attempts to give a comprehensive description of characteristics the cold pools using the FENNEC AWS station surface measurements of atmospheric variables. For this I formulate detection method for cold pools occurring in particular in the SHL region based on analysis of available data and previous identification methods applied to other locations. Having identified cold pools I present the mean characteristics of cold pools. The occurrence frequency, spatial distribution, and seasonal variation of cold pools in the SHL region are presented. I further compare surface observation characteristics of selected cold pool events with re-analysis outputs and thus derive the associated bias arising due to lack of resolving these mesoscale processes in models. The remainder of the chapter is organized as follows. Section 5.2 presents the data and methods used in the identification and characterisation of cold pool events. Results are presented in section 5.3. Section 5.4 focuses on comparison of measurements with reanalysis products. Section 5.5 provides summary and conclusion of results.

5.1 Data and Methods

I use data collected with Fennec Automatic Weather Station (AWS) instruments deployed in the Sahara desert (fig. 5.1). This is the most comprehensive set of observations ever obtained across the heart of the SHL region. Despite limitations in these data, they provide the basis for a first detailed analysis of cold pools in the SHL based on direct observation. Each station has identification number and I use these numbers to refer to each station in what follows. The locations of the two super sites (SS1 and SS1) are also shown but I do not use data directly from these stations

because (Allen et al., 2013) has already presented a comprehensive analysis at SS1 and no cold pool were detected at SS2 (Todd et al., 2013). Data are available for years 2011 and 2012 period. Here I limit my analysis to JJAS, the time during which Saharan

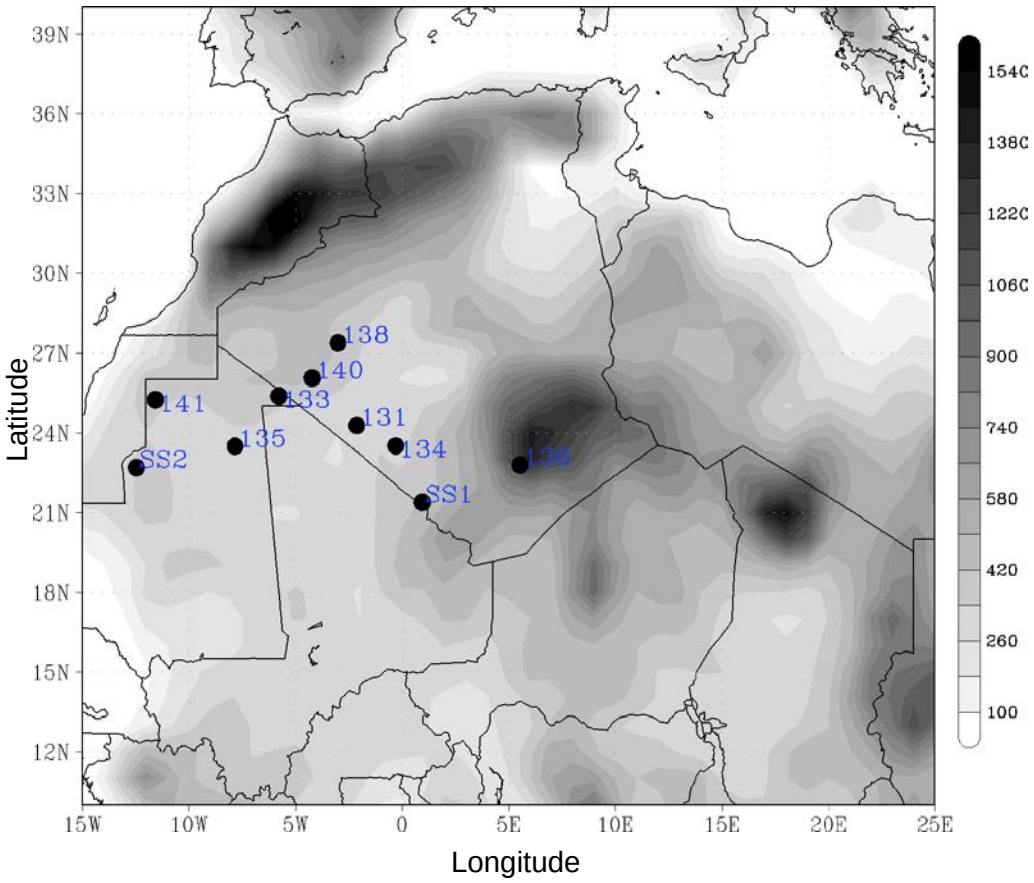

Figure 5.1 Location of the AWS station (dots) with respective identification numbers and elevation in meters (shade)

heat low plays a significant role in the activation and development of the monsoon flow and it is the peak season for moist convection over the Sahel and Sahara and therefore initiating cold pool formation. The list of available data for each station is given in Table 5.1. Measurement is made approximately every three minutes. For detection and characterisation of cold pools I use temperature, pressure, water vapour mixing ratio, wind speed, and wind direction. I also use dew point temperature which is derived using temperature and water vapour mixing ratio using equation 5.1:

$$T_d = \frac{cf}{b-f} - T_0 \tag{5.1}$$

where $c = 243.5, b = 17.67, T_0 = 273.5, RH$ is water vapour mixing ratio and $f = \ln\left(\frac{RH}{100}\right) + b\frac{(T+T_0)}{(c+T+T_0)}$ where T is temperature.

The measured variables have varying degrees of uncertainty due to errors in measurements. Humidity, temperature, and wind speed measurements have uncertainties up to 0.6%, 0.2 ^{0}C, and 0.1 m s^{-1} respectively. SW and LW radiation each have larger measurements uncertainties up to 38 W m^{-2}. A complete description of the AWS instrumental design, measurements, and associated measurement uncertainties of all variables can be found in Hobby et al. (2013). For comparison of measurement with models, I use 2m temperature, wind speed, and mixing ratio from reanalysis products. When 2m wind is not available, I derive it from 10m wind speed using the equation 5.2:

$$v_1 = v_2 \frac{ln\left(\frac{z_1}{z_0}\right)}{ln\left(\frac{z_2}{z_0}\right)} \tag{5.2}$$

where v_1 and v_2 are wind speeds at heights z_1 and z_2 respectively, and z_0 is the roughness length which is computed using the 2m and 10m wind speed from MERRA re-analysis. Further, I use surface longwave flux for comparison with reanalysis products.

For testing my algorithm for detection of cold pools data from AWS station 134 is used. The choice of station 134 is because of availability of relatively more data compared with other stations during JJAS 2011/12 period. The arrival of cold pool outflows at a given location is typically characterised by gusty wind that carry moisture within it ventilating the vicinity area. Therefore cold pool events are in general associated with the increases in moisture, wind speed, pressure, and decrease in temperature. However an increase in moisture and decrease in temperature are not necessary conditions for cold pool identification since depending on the details of their formation, cold pools may carry wetter or dryer air than the surrounding environment (Flamant et al., 2009;Miller et al., 2008). I consider here cases that resulted increase in water vapour mixing ratio only because of the extremely high surface temperature and arid conditions, it is expected mostly cold pools in the SHL moistening of the atmosphere. I use changes in wind speed and humidity (dew point temperature) as primary selection criteria for cold pool events.

Table 5.1. Data availability at AWS stations(C=complete, BD=Bad Data, ND=No Data) Range of numbers show days when data is available

Date	131	133	134	135	136	138	140	141
2011/06	1-8	01-05	C	2-3	7-30	C	1-4	2-3
2011/07	ND	ND	C	ND	1-30*	C	ND	1,2,5-31
2011/08	ND	ND	BD	ND	23-31	02-31	ND	BD
2011/09	ND	ND	BD	ND	1-16, 18-30	C	ND	5-3
2012/06	1-30*	3-30	1-30*	2-30	1-30*	01-30*	BD	14-30
2012/07	1-31*	1-31*	1-11, 13-31	1-31	1-10, 12-31	01-11, 13-31	BD	1-31*
2012/08	1-31*	1-31*	1-31*	ND	1-31*	01-31*	BD	1-24
2012/09	1-30*	1-30*	1-30*	ND	1-30*	01-04	BD	ND

* there are missing time steps in each day data

Satellite images of Spinning Enhanced Visible and Infrared Imager (SEVIRI) are used to verify existence of deep cloud and dust emission (Allen et al., 2013;Karam et al., 2014;Marsham et al., 2013b). On SEVIRI product of false colour composite imagery deep cumulonimbus is shown in dark red and dust is shown in pink colour (Brindley et al., 2012;Lensky and Rosenfeld, 2008). However dust is only visible in the absence of high level cloud and thus some dust events could be missed from the infrared SEVIRI imagery (Ashpole and Washington, 2012). Once all cold pools are clearly identified, I compare surface observations with data from MERRA and Era-I reanalysis model outputs in order to estimate the error in amount of moisture resulting from models' lack of resolving convection. For the details of the satellite and reanalysis model data used, readers are referred to chapter II.

To formulate a robust algorithm which will clearly identify cold pools, I employ the steps described below.

I. Synthesise evidence from literature on the likely 'signature' of cold pools

Previous studies attempted to identify the meteorological signature of cold pools using different methods. A summary of the cold pool identification processes for selected publications is provided in table 5.2. Engerer et al. (2008) studied characteristics of cold pools using surface observations made between 2000 and 2007 in Oklahoma, USA. Arrival of the leading edge of the cold pool outflow is determined from rapid change in wind direction (wind shift). The magnitude of change in

atmospheric variables associated with passage of cold pools is determined by finding the minimum or maximum of a given variable during the 30 min period before and during the 2 h time window after the wind shift occurred. They identified 39 cold pools from mesoscale convective events with mean characteristics of 3.2 - 4.5 hPa rise in surface pressure 5.4 - 9.5 K drop in 2 m air temperature, and mean wind speeds above 15 m s^{-1}. In a similar study Provod et al. (2016) characterised cold pools in the West African Sahel region using measurements from the African Monsoon Multidisciplinary Analysis Special Observing Period (AMMA SOP). They identified cold pool events using the following criteria: at least 30^0 change in wind direction, speed of the gust greater than 1.5 times the mean wind speed within 30 min before arrival, and temperature drop by 1 K. During the study period from June 01 to September 30 ,2006 Provod et al. (2016) identified 42 cold pool events with a mean characteristics of 4 hPa increase in surface pressure, 8 K decrease in temperature, with 12.5 m s^{-1} wind gusts. Note that the difference of identification method in Provod et al. (2016) to that of Engerer et al. (2008) is that the former used a 1 h pre-storm time period to find the minimum or maximum of variables instead of the 30 min used by the later. Emmel et al. (2010) applied different detection algorithm for arrival of cold pools which used increases in mean horizontal wind speed by 4 m s^{-1} and increase in dew point temperature by 4 K within 30 min after the passage of the front. Redl et al. (2015) used a similar method (table 5.2) for the identification of cold pools.

II. Identity candidate cold pool events with minimum threshold conditions

In my work I use change in dew point temperature (ΔT_d) and mean wind speed (U_av) after passage of the front as primary variables for identification of cold pools. Dew point temperature is most appropriate variable for hyper arid environment rather than temperature. Cold pools are identified when change in dew point temperature is greater than 2 K and mean wind speed for 1 h after event is greater than 4 m s^{-1}. In the calculation of change of dew point temperature, mean T_d 30 min before the event and mean T_d 1 h after the event are used. To avoid any outlier due to turbulence associated with arrival of storm and to include cases when change in T_d and wind speed do not occur simultaneously, calculation of change of a given parameter is made outside a 30 min time window, 15 min before and 15 min after arrival of a given cold pool event. In some cases one event could be picked up more than once if at a given time step the criteria for selection of a cold pool are fulfilled. In such cases I take one with largest change in T_d.

Table 5.2. Summary of Cold pools identification methods from previous studies

Paper, location and study time	Variables used in calculation of cold pool characteristics	Cold pool Identification Criteria
Engerer et al., 2008 Oklahoma USA, 2000-2007	• P, T, v, wind direction • Difference of max (or min) of a variable 30 min before the event and 2 h after the event.	• Rapid Change in wind Direction • Convective lines >200km in length • Reflectivity > 50dBz
Provod et al., 2016 Niamey, Niger June 01 - Sept 30, 2006	• P, T,θ_e , WVMR, v , wind direction • Difference of max (or min) of a variable 1 h before the event and 2 h after the event.(P, T) • Mean 1h before and 2h after (θ_e) • Mean 1h before and Minimum 2h after (WVMR) • Max 2 h after (wind)	• Rapid Change in Wind Direction within 5 min by at least 300 • Max Wind speed 2h after passage > 1.5 times mean wind speed 30 min before the passage • Temperature drop by1K • Verified using radar or satellite images for MCS in the vicinity area
Redl et al., 2015 North West Africa, IMPETUS, 2002 – 2006	• Td, V, Precipitation, Satellite brightness temperature • Difference of maximum Td in 30 min after detection and Td during arrival • Mean wind speed 1 h after jump in Td	• Td in 30 min • Mean wind speed 1h after the passage • the average of Td 1 h after the detected jump has to be 2 K larger than the average of Td 1 h before the jump • no precipitation 1 h • An event observed at least in two stations • Verification microwave brightness temp • Distance between a station and convection in SEVIRI image

Wind direction is used as a primary indicator of cold pool passage in Erenger et al. (2008) and Provod et al. (2016). Here I do not use wind direction as an indicator due to error in AWS wind direction data which has a precision of 45^0. Some authors use

decrease in temperature and increase in pressure to identify cold pool events. I have not used both these variables for the following reasons. Temperature does not always decrease while pressure does not always reflect quick response to arrival of cold pools and when there is, it does not always change simultaneously with other variables. Selected cases for increase and decrease of temperature will be presented in the results section. Further in examining a number of cases of known events there was no consistence signal in surface pressure. There are also lots of missing data points of observed pressure which makes it further difficult to use it as detection criteria. However in some ambiguous cases, I use the drop in temperature and rise in pressure as secondary verification criteria. It is important to note that my detection algorithm could miss out some cold pool events with small effects on atmospheric variables. There are some cases with clear signature of arrival of cold pool on SEVIRI images but missed in my identification which are further discussed later in this chapter.

III. Verify all candidate events.

Having identified all events that satisfy the minimum threshold conditions described above, I attempt to verify these using SEVRI imagery. For each event I examine SEVIRI images for some hours before and after to detect cold pool propagation in the area around the AWS site. I look for clear dust plumes and to consider cases where haboobs occur without significant dust I determine the likelihood based on the presence of deep convective cloud in the proximity in the hours before the apparent event. Based on this subjective but informed analysis I am able to identify events where there is little evidence of a haboob occurring and thus drop out all other cases which are not cold pool related. In the identification of cold pools one may encounter cases with large changes in atmospheric variables, sometimes part of diurnal cycle of synoptic variability, fulfilling the selection criteria, however not associated with convective downdraft. Changes in atmospheric variables from such cases is gradual in contrast to many cold pool cases where changes are abrupt. The sudden jumps of atmospheric variables in the plots of time series are used as indicator of cold pool arrival. However abrupt changes are not used as a necessary condition for cold pool identification since there are cold pool arrivals with no clear sudden changes but clearly verified on SEVIRI images.

Table 5.3. Statistical properties for all the verified cold pool events

	ΔT_d (K)	ΔU(m s^{-1})	U_av(m s^{-1})	U_{max}(m s^{-1})
STDEV	4.8	2.7	2.6	2.6
Mean	8.6	4.6	8.0	9.5
Minimum	2.1	-1.1	4.1	4.7
Maximum	23.4	10.8	13.8	15.3
Median	7.8	4.5	7.9	9.5

A total of 146 events are identified on the first stage of identification process, which satisfied the criteria of change of dew point temperature greater than 2 K and mean wind speed after 1 h of event passage greater than 4 m s^{-1} at AWS 134 station, 42 of which are verified using SEVIRI images for convective activity and (or) dust emission. For those events which are verified to be cold pool related, I derive the statistics for change in dew point temperature, change in wind speed, and mean wind speed 1 h after the cold pool passage. The results for the characteristics of the cold pool event signatures is presented in table 5.3.

IV. Refine the thresholds to 'optimise' cold pool detection

The first stage selection criteria is lenient capturing many small scale atmospheric features which are not cold pool related. It is rather cumbersome to carry out similar procedure for all other stations. I refine the thresholds to ensure an acceptable compromise between false alarms and missed events as follows:

- Change in dew point temperature greater than 3 K.
- Change in wind speed greater than 2 m s^{-1} or average wind speed one hour after cold pool passage greater than 4.5 m s^{-1}.
- SEVIRI imagery for nearby convective activity or dust emission in the following hours.

The reason for using change in mean wind speed in addition to average wind speed because I found clear cold pool cases where the mean wind speed is small. This will be further investigated in the results. Once I have arrived at an acceptable algorithm using data from AWS 134 I apply to all other stations.

5.2 Results

Once all the cold pool events are clearly identified for the JJAS 2011/2012 period I characterise the cold pool events over the SHL region and derive occurrence frequency. Then based on the occurrence frequency and comparison of observation with reanalysis I estimate the amount of moisture which is misrepresented from models lack of resolving such meso-scale convective events.

5.1.1 Cold Pool Characteristics

Using the method described above I identified a total of 145 cold pool events across the eight AWS stations during JJAS, 2011 and 2012. The list of identified events and their resulting changes in atmospheric variables are presented in table A1. Characteristics of all identified cold pool events are summarized in the box and whisker

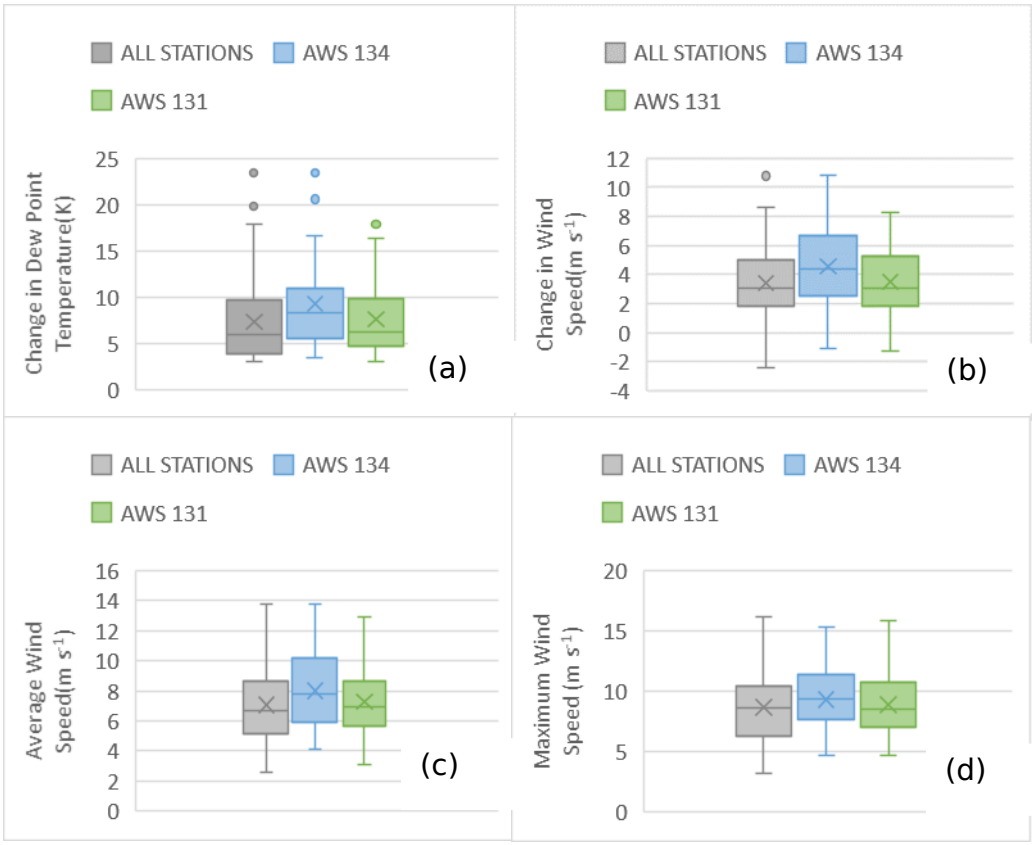

Figure 5.2 Box plot of change in (a) dew point temperature (ΔT_d) in K, (b) change in wind speed (ΔU), (c) average wind speed (U_{av}) and (d) maximum wind speed (U_{max}) in in m s^{-1} associated with cold pools. Boxes represent the interquartile range, whiskers show minimum and maximum values excluding outliers and crosses and lines in the boxes show mean and standard deviation of each variable. Dots above whiskers are outliers

plot, fig. 5.2. The vertical lines at the bottom and top of each box denote the minimum and maximum values respectively whereas the boxes represent the 50% of the values between first quartile (Q_1) and third quartiles (Q_3) or Interquartile range (IQR). All the parameters used to characterize cold pools lie within the upper limit (Q_3+1.5*IQR) and lower limit (Q_1-1.5*IQR) except for change in dew point temperature which has outliers in the upper limit (18.4 K). The change in T_d is greater than 9.7 K in 25% of the total cold pools that is larger than the value (5.3 K) reported in Emmel et al., 2010. Change in wind speed has relatively normal distribution from its mean value 3.4 m s^{-1} with the first quartile 1.8 m s^{-1} and third quartile 5 m s^{-1}. From all the cold pool events I identified, 25% have average wind speed and maximum wind speed greater than 8.6 m s^{-1} and 10.4 m s^{-1} respectively.

Frequency distribution of change in dew point temperature associated with cold pool passage for all stations during 2012 is shown in fig. 5.3. There is a wide range of magnitudes of cold pool signatures resulting in change of dew point temperature from 3 K to over 20 K confirming the results in the box plot, fig. 5.2. The signature of cold pools revealed as changes in atmospheric variables depends in general on the location of a station from starting point of a cold pool and on season (Provod et al., 2016). Cold pools that are detected at AWS 131 have smaller change in magnitude than those at AWS station 134 (fig 5.3a and 5.3b). The mean change in dewpoint temperature is 7.2 K for all stations with maximum change of 23.4 K recorded at station 134 on July 17, 2012 around 03:30, fig. 5.4. I considered here cases with increase in T_d and thus increase in moisture as a result of cold pool arrival. It is important to note the 3 K threshold for change in T_d despite the fact that there are cold pools which are not included in my analysis that resulted in change of T_d as small as 2 K. For instance a cold pool event detected at AWS 134 on June 23, 2012 at ~16:00 has a change in dew point temperature of 2.1 K. This small change in dew point temperature could possibly be due to the cold pool late in the previous day at 22:00 has already moistened atmosphere and was sustained relatively higher because of cloud. Such cases will be presented in later section of this chapter. I find the month July to be the time when strongest magnitude cold pools occurred. Reaffirming this the mean change in T_d for all stations in 2012 is 7.2 K, 8.0 K, 7.1 K, and 5.9 K for June July, August, and September respectively.

Distribution of average wind speed 1 h after cold passage for all stations during 2012 is presented in fig. 5.5. The difference in wind average wind speed frequency (fig 5.5a and fig 5.5b) difference between AWS 131 and AWS 134 does not show a clear difference to that of dew point temperature frequency distributions (fig 5.3a and fig 5.3b). This implies the moisture brought in as cold pool during a cold pool passage and

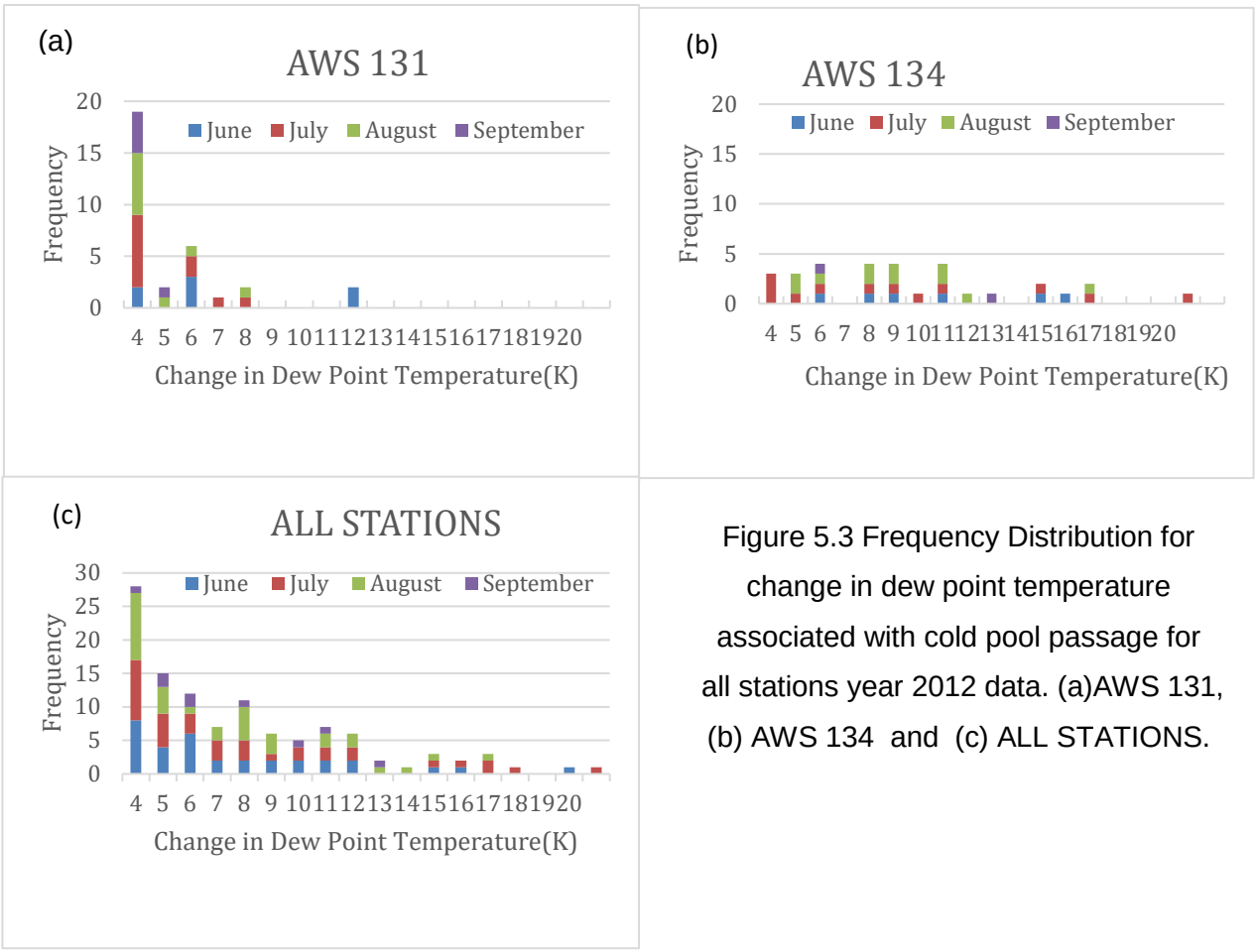

Figure 5.3 Frequency Distribution for change in dew point temperature associated with cold pool passage for all stations year 2012 data. (a)AWS 131, (b) AWS 134 and (c) ALL STATIONS.

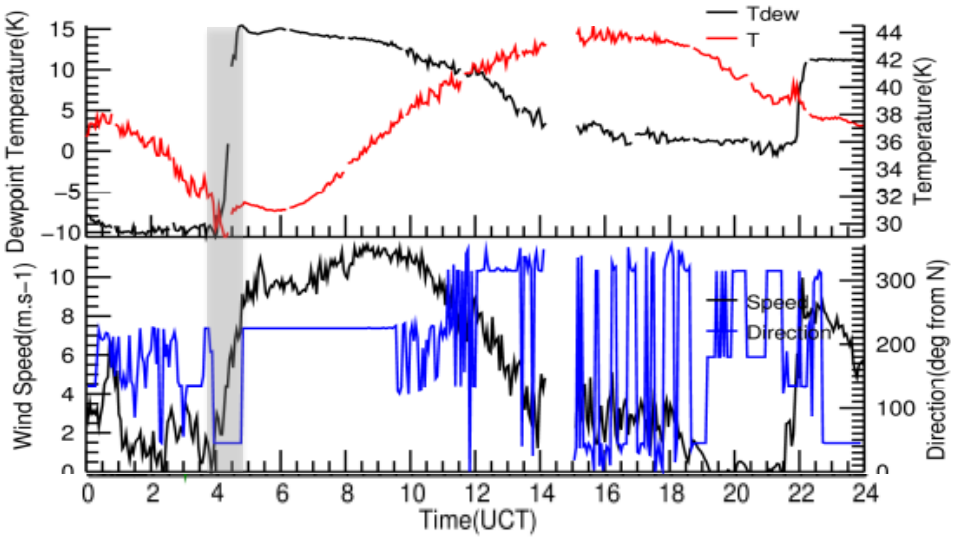

Figure 5.4 Cold Pool resulting the largest change in dew point temperature occurred at AWS 134 on July 17, 2012, ~04:00. The shaded region shows the arrival of the cold pool.

wind speed of the cold pool do not have a correlation based on the results of the two stations. The average wind speed for all available data is 7.0 m s^{-1} and maximum speed up to 14 m s^{-1} is recorded (Trzeciak et al., 2017). The average change in magnitude of wind is 3.4 m s^{-1}, the maximum being 11 m s^{-1}. Wind speed increases in general as a result of cold pool passage but there are cases of decrease in wind speed. This could be due to the prevalence of strong background wind flow in the opposite direction prior to cold pool arrival at a particular station. It is therefore necessary to take this into account when using wind speed as a selection criteria and therefore avoid misses when change in wind speed is negative. This is the reason for using magnitude of average wind as selection criteria in addition to change in wind speed in this work.

A rapid change in wind direction is a common feature of arrival and passage of cold pools (Engerer et al., 2008;Provod et al., 2016). Despite the inaccuracies in wind direction data at AWS as already mentioned, it still shows the arrival of cold pool. I also find there is change in wind direction up to 180^0 resulting from cold pool arrival at a given station (fig. 5.4). However this is mostly followed by erratic changes in wind direction after the cold pool passage making it practically challenging to set a threshold for identification. Besides wind direction could exhibit similar sudden and rapid change due to non-cold pool related atmospheric features.

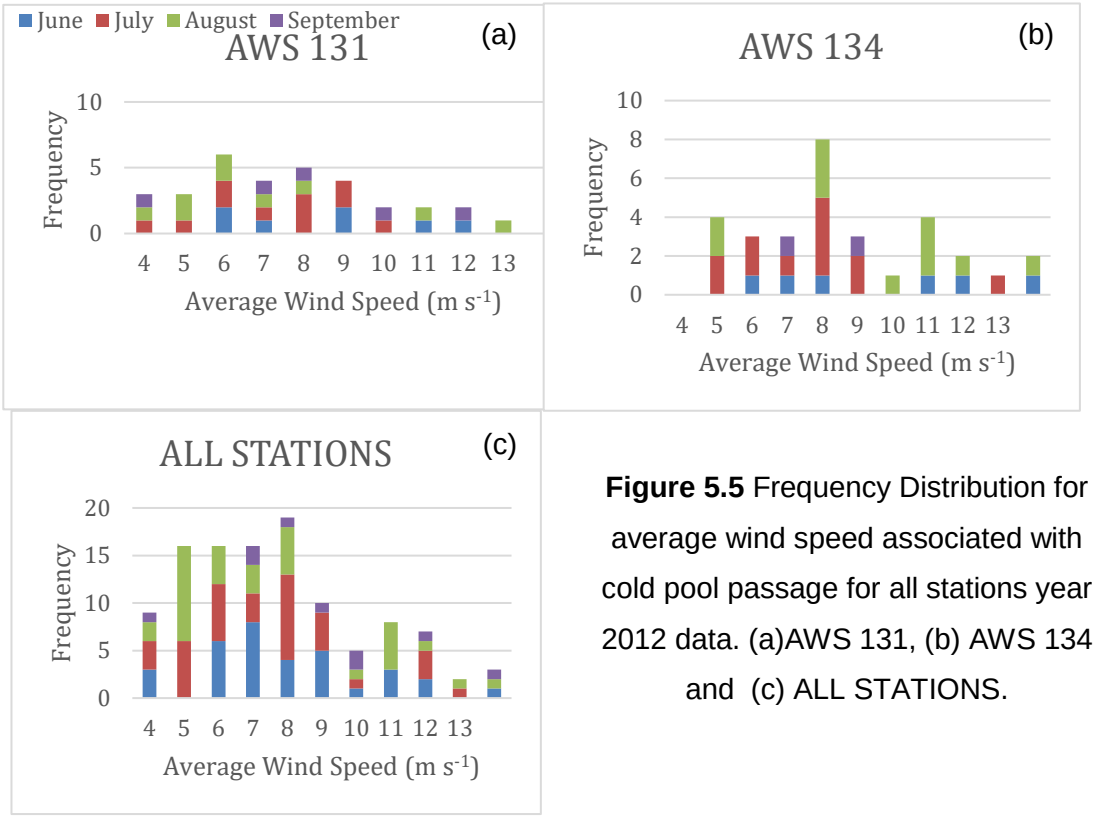

Figure 5.5 Frequency Distribution for average wind speed associated with cold pool passage for all stations year 2012 data. (a)AWS 131, (b) AWS 134 and (c) ALL STATIONS.

Temperature does not always show the same response to cold pools arrival. I find cold pools mostly with clear drop in temperature however several instances of rise in temperature due to cold pool passage were also identified. Figure 5.6 shows examples of two typical cold pools occured in the same day which resulted in drop and rise of temperature. The first cold pool arrived at ~02:00 raising the temperature by ~5 K while the second cold pool which is relatively weaker arrived at ~23:30 resulting in a temperature drop of ~1.5 K. Emmel et al. (2010) also recorded an increase of 2m air temperature up to 6 ^{0}C as a result of cold pool passage while Provod et al. (2016) showed all the cold pools considered in their study to have decrease in temperature of up to 14 ^{0}C. In my results temperature drops mostly occur in the late afternoon cold pools while temperature rise occurs when cold pools arrive in the early morning hours following the radiative cooling of the relatively dry background atmosphere. This however needs further investigation.

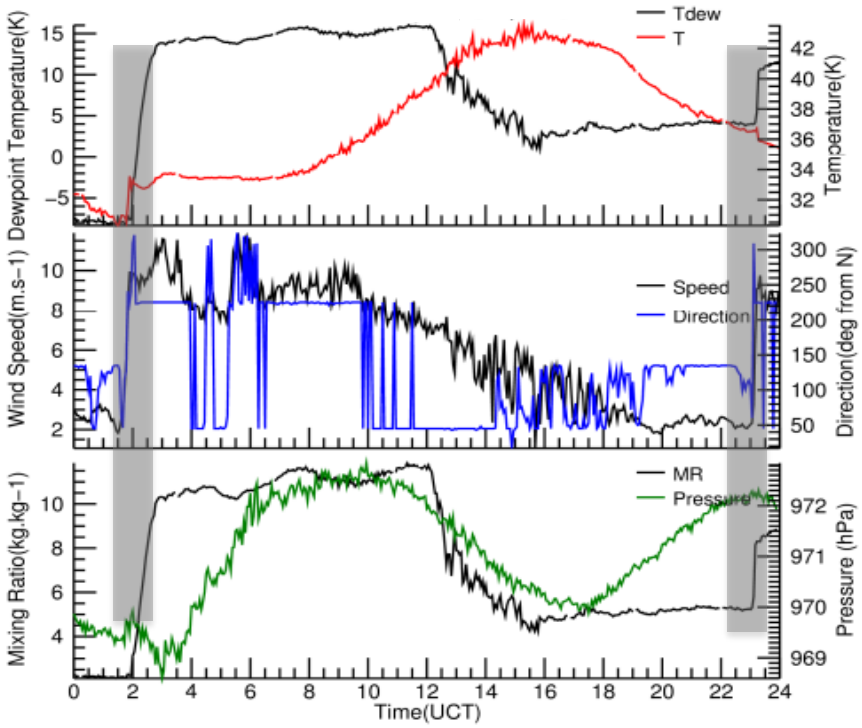

Figure 5.6 Example of cold pools resulting in temperature increase (at 02:00) and decrease (at 23:00). Shaded areas show approximate arrival time of cold pools arrival.

5.2.2 Cold Pool Frequency

Cold pool frequency shows both seasonal and inter-annual variability (Emmel et al., 2010). Here I assess the seasonal variability of cold pool frequency across the AWS

stations. I find the month July to be the time when most cold pools occur while September is the least. In 2012, from a total of 111 cold pools, 36 occurred in July, 33 each in June and August, and 9 in September. The number of cold pools identified at each station for each month is listed in table 5.4. I did not include AWS 140 in my analysis of cold pools frequency since the available data at this station is small. In addition to seasonal variability, frequency of occurrence also varies on location. I find more cold pools occur in the southern edge of the Saharan heat low region as one might expect pertaining to the monsoon flow. This can be confirmed by comparing the

Table 5.4 Number of identified Cold Pools at the AWS stations

Date	131	133	134	135	136	138	141
2011/06	-	-	6	-	3	3	
2011/07	-	-	4	-	1	1	-
2011/08	-	-	-	-	1	7	-
2011/09	-	-	-	-	-	4	3
2012/06	6	2	6	1	7	7	3
2012/07	11	2	12	6	-	3	2
2012/08	9	1	12	-	-	4	8
2012/09	5	2	2	-	-	-	-
*Frequency of occurrence	0.25	0.1	0.24	0.12	0.07	0.15	0.15

*Number of Cold Pools per day (when data is available) in 2012

number of cold pools (Table 5.4) identified at station 134 (located at 23.5^0 N and 0.3^0 E) and 138 (located at 27.4^0 N and 3.0^0 E). During the times where data is available, the number of cold pools detected at station 134 is 32 while in the same period 14 cold pools are detected at station 138. This can be further confirmed by the frequency of cold pool occurrence derived for 2012. During JJAS period an average of approximately 30 cold pools occur at AWS stations 134 and 131 compared with approximately 20 cold pools at AWS stations 138 and 141. The number of cold pools identified at AWS station 136, which is located on approximately the same latitude as AWS station 134 is to the contrary small. However there are lots of missing data at this station particularly in 2012. Allen et al., 2013 identified 20 cold pools at Bordj Bhadji Mokhtar in southern Algeria (SS1, fig. 5.1) during June 07-30, 2011. This is a large number compared to previous studies and to what I have found here during similar period at AWS 134 which is located close to SS1 (fig. 5.1). However some of the cold pools reported in Allen et al., 2013 are not verified with SEVIRI imagery. In the

calculation of the occurrence frequency of cold pools (Table 5.4) I have considered only available data. That is I exclude times with missing data within a day. This will possibly subject to biases in my calculation as there are hours in a day (early morning and late afternoon) that cold pools are more likely to happen but unidentified because of data unavailability. In spite of that, my results give us a broad overview of the distribution of cold pool across the AWS stations. This however needs further investigation with a more complete and equivalent data set at each station.

5.2.3 Missed Cold Pools

To emphasize the subjective nature of cold pool identification, I next present the list of cold pools clearly observed by SEVIRI but without strong signature on ground measurements of atmospheric variables. As mentioned earlier some cold pools could be missed undetected when changes in the atmospheric variables as a result of cold pool passage do not meet the minimum threshold. Despite the small changes in atmospheric variables, some of these events are clearly seen on SEVIRI imagery. Table A2 lists such cases with date and approximate time of arrival of cold pool at each station. More cold pools are missed unidentified at AWS stations 134 (14 cold pools) and 136 (16 cold pools) compared with those at station 138 (7 cold pools). Some of these unidentified cold pool events show a big signature (dust emission) on SEVIRI images. The cold pools observed on 10 July, 2011 around 00:30 at AWS station 136 and on 24 June 2012 around 00:30 at station 141 are typical examples. It is not clear why there is no clear signature on the data as a result of these cold pools observed on SEVIRI however there is no missing or bad data on these days. This reaffirms identification of cold pools is a subjective process and it may be challenging to identify each and every cold pool that occurred at a given station.

It is worth mentioning at this point that some atmospheric phenomena I identified have signatures in atmospheric variables similar to that of cold pool arrival but with no obvious convective activity in the vicinity. For instance at station 133 on 2012/08/31 07:00, there is an event resulting in a change in dew point temperature 11.2 K and average wind speed 5.5 m s^{-1} after the passage of this event. Another similar event but with slightly less magnitude change in dew point temperature, 9 K and stronger wind average speed 8 m s^{-1} was recorded at AWS station 136 on 2012/06/16 14:00. I have listed in table 5.6 such cases resulting in jumps in moisture and wind speed which are not related to convective activity. I will not investigate the cause of these events as it is not the objective of this research. But I would like to point out the need for a careful verification of cold pool events using satellite images or other in-situ

instruments for measurement of convective activity and (or) dust emission in the vicinity of a given station.

Table 5.5 Atmospheric processes with signatures similar to cold pools but not related to convective activity.

Station	Date	Time	ΔT_d(K)	ΔU(m s^{-1})	U_{av}(m s^{-1})	U_{max}(m s^{-1})
131	20120623	05:16	3.1	-0.4	6.1	7.8
	20120831	07:00	11.2	1.0	5.3	6.2
136	20110615	23:00	5.7	2.2	3.3	5.4
	20120616	14:00	9.0	3.8	8.1	9.3
138	20110602	02:00	25.7	3.7	3.7	4.3
	20110811	02:30	3.6	1.0	4.7	5.9
	20110928	07:06	3.0	2.8	2.9	3.2
	20120901	04:06	3.2	1.8	4.5	5.3
141	20110907	22:00	4.5	2.3	4.4	6.0
	20110909	19:00	4.4	3.7	5.6	6.4
	20110921	06:56	7.2	2	4.4	6.4
	20120704	19:00	6.2	0.6	6.5	8.2
	20120803	08:23	5.5	1.9	4.6	5.1

5.3 Comparison with Re-Analysis.

So far I have seen characteristics and frequency of occurrence of cold pools in the Sahara desert using observational data. Such meso-scale processes, which are shown to play significant role in the transport of moisture to the heart of the SHL, are not well represented in climate models (Heinold et al., 2013). To further investigate this I compare mixing ratios and surface long wave flux with corresponding reanalyses simulation. I have taken mixing ratio, instead of dew point temperature (variable used for cold pool identification) is to estimate the error in longwave flux due to bias in mixing ratio. This is derived by first deriving the approximate relation between column integrated water vapour and mixing ratio. Figures 5.7 and 5.8 show observed and MERRA output mean diurnal mixing ratio and longwave flux at selected AWS stations. MERRA has a weak representation of the diurnal cycle at most stations except AWS 141. The diurnal cycle at AWS 141 is stronger compared with other stations. This is due to the proximity of AWS 141 to North West coast of Africa which experiences strong diurnal cycle from the meso-synoptic-scale circulation of the Atlantic inflow

(Grams et al., 2010;Todd et al., 2013). The main features in this cycle are strong sea breeze penetration into land following the decaying of the turbulent convective boundary layer in the evening which extends until 7:00 AM after which sea breeze declines as a result of the redevelopment of the boundary layer (see fig. 8b in Grams et al., 2010 and fig 9a in Todd et al., 2013). MERRA slightly overestimated moisture at all stations except 141 which MERRA has underestimated moisture (Table 5.6). The error

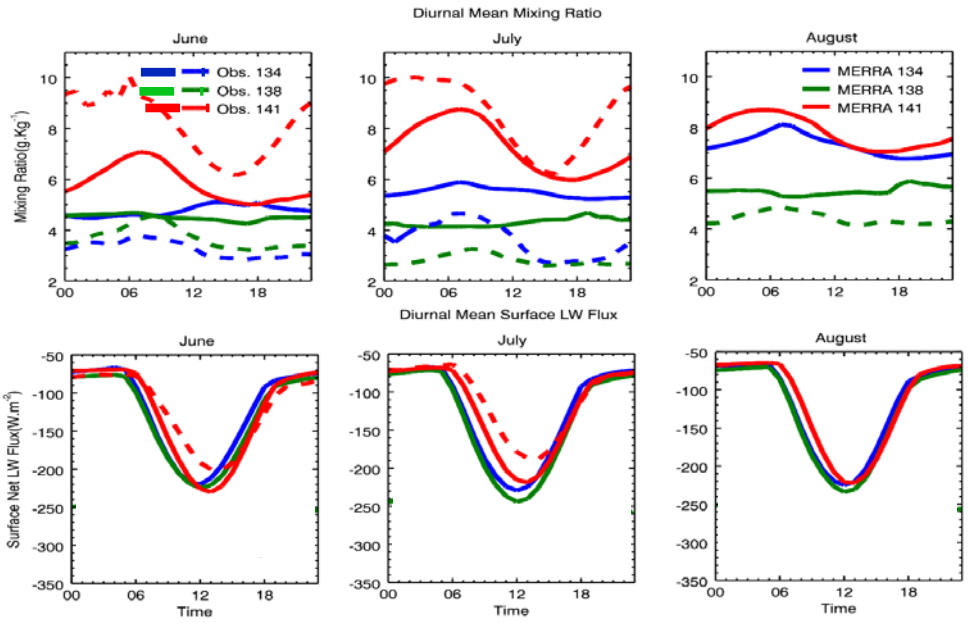

Figure 5.7 Diurnal Cycle of water vapour mixing ratio and net surface flux at selected AWS station during 2011.

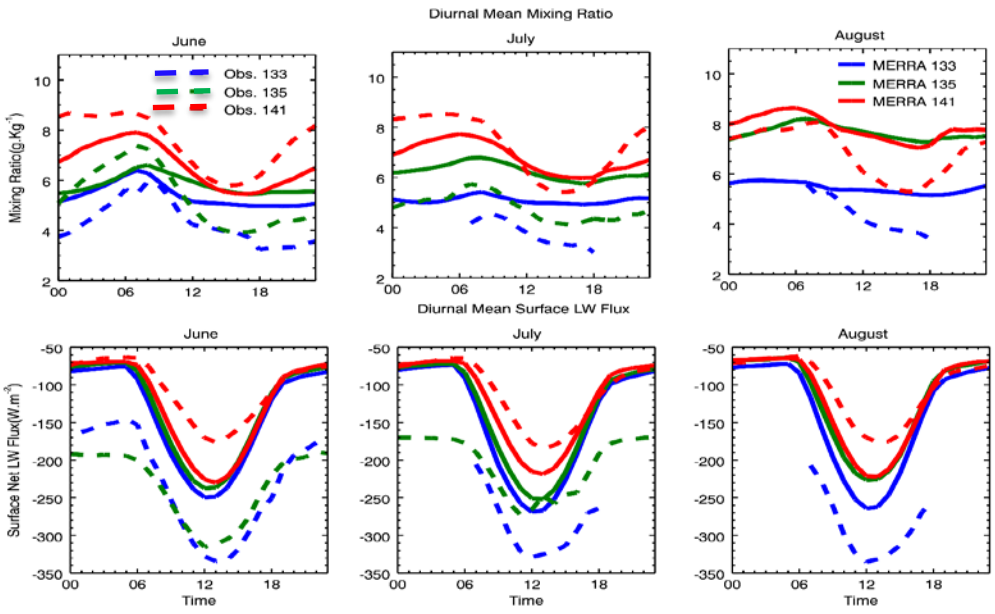

Figure 5.8 Same as fig. 5.7 except for 2012.

in observed surface longwave flux and MERRA simulation is consistent with the error in moisture amount. That is as underestimated moisture the resulting net surface longwave flux becomes smaller and the vice versa (see section 4.4.2.2 of previous chapter). However the discrepancy between observed and model longwave flux may not entirely due to error in moisture amount. To quantify this I estimated the approximate relation between vertical integrated water vapour and near surface mixing ratio at BBM (see fig. 5.9) and sensitivity of CIWV to surface longwave flux derived in chapter-IV. I apply this for example to AWS 133 at which mean mixing ratio is underestimated by 1.7 g kg^{-1}, the estimated corresponding value in CIWV will be ~22 Kg m^{-2}. Using the results of table 4.6, this will result in an error of 35 W m^{-2} on the net surface longwave flux which is about to a third of the actual difference I found between observed and MERRA simulation. This clearly shows that the error in net longwave flux is not totally a result of error in moisture amount. This will be further investigated for each cold pool cases.

Table 5.6. Diurnal mean Bias (Observation - MERRA)

Month/Year	AWS	ΔMR(g kg^{-1})	ΔLW(W m^{-2})
JJ/2011	134	-1.7	-
JJA/2011	138	-1.1	-130
JJ/2011	141	1.8	8
JJA/2012	133	-1.1	-104
JJ/2012	135	-0.7	-86
JJA/2012	141	0.2	14

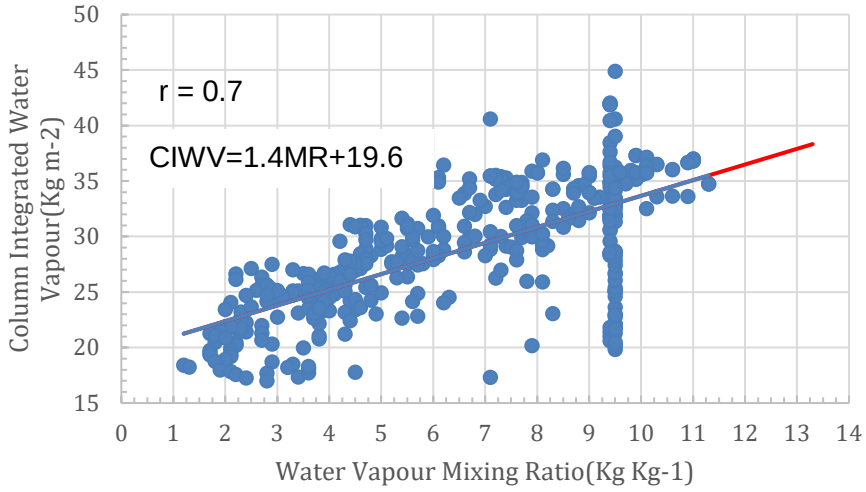

Figure 5.9 Scatter plot of water vapour mixing ratio versus column integrated water vapour at BBM, June 2011. The red line shows linear fit

5.4 Summary and Conclusion

The role of cold pools in the regional dynamics over the Sahara desert is vital, most importantly their role in (i) the transport of moisture from monsoon (Garcia-Carreras et al., 2013;Marsham et al., 2013a) in the south and Atlas in the north (Redl et al., 2016;Emmel et al., 2010) to the central Sahara desert and (ii) emission of dust (Allen et al., 2013;Marsham et al., 2013b). This chapter provides a description characteristics and frequency of cold pools using in the AWS stations data spread across the Saharan Heat Low region during JJAS in 2011 and 2012. I used a unique identification method that effectively identifies cold pools using changes in meteorological variables confirmed by SEVIRI imagery for convective cloud and dust emission. I further compared observed atmospheric variables with reanalyses simulation outputs.

A total of 137 cold pool events were identified at the eight AWS stations across the Sahara desert. It should however be emphasized that because the data is not complete for the whole study period, more cold pools expectedly occur than what I found here. There are two major sources of convection for the formation of cold pools in the in the region. The first and dominant source is the monsoon flow carrying moisture from Gulf of Guinea to the Sahel. Cold pools resulting from the monsoon flow are stronger in magnitude and mostly followed by dust emission. The second source of cold pool formation is convection triggered over the Atlas Mountains.

The passage of cold pools is associated with increase of dew point temperature up to 23 K, mean change in wind speed 3.4 m s^{-1}, and maximum wind speed up to 14 m s^{-1}. Even though I considered cases where cold pools arrival causing increase in moisture due to the dry conditions of the SHL, it is not always the case (Flamant et al., 2009;Miller et al., 2008;Provod et al., 2016). For instance Provod et al., 2017 that found in premonsoon period (June 1 - June 12) decrease in water vapour mixing ratio compared to other later periods. However their domain of study is Niamey, Niger which is located south to all the station data I used. I find more cold pools in the southern edge of the Saharan heat low compared to that of the northern edge. During JJAS 2012 period of time 0.24 and 0.15 cold pools per day are detected at AWS stations 134 and 138 respectively. Furthermore more cold pool events happen during July and August. This is related to the seasonal cycle of the intensity of the SHL which is fully developed around mid-June onwards and starts to decline after August (Lavaysse et al., 2009), see also section 3.4 of this thesis.

An important feature of cold pools is their role for the formation of next day convection after their passage and hence cycles of convection followed by cold pool

(Trzeciak et al., 2017). I observed such cases in the central Sahara. An example of cycle of convective events showing how monsoon brought moisture is transported deep into the Sahara Desert and further north west to the Atlas: Convective activity resulting in cold pool Around 06/21 ~06:30 over Algeria Mali Niger triple point, leading to formation of another convective activity resulting in cold pool arriving at BBM around 06/22 01:15 and at AWS 134 at around 10:00. This in turn triggers two convective cells in southern Algeria merging and resulting in cold pool reaching to AWS 134 on 22nd at ~22:00. And finally convective cloud forming near Western Algeria maturing and resulting in cold pool on 23rd ~21:00 which moves further to North West. Several similar processes occur over the entire summer period (Provod et al., 2016;Trzeciak et al., 2017).

This, however, is mostly missing in forecast or climate models that use parametrized convection. Reanalyses simulation despite their assimilation of observations and improved representation of atmospheric processes still struggle to resolve convection (Sodemann et al., 2015). To investigate this I have made comparison of measurement and reanalyses simulation products. The results of comparison of observed with MERRA output shows diurnal mean mixing ratio is not always underestimated. I find the mean moisture at selected AWS stations is actually overestimated compared with MERRA. In addition diurnal mean surface longwave flux shows a large bias of up to -100 W m^{-2} in MERRA. This however needs further investigation.

There is a huge implication in the dynamics and energy budget of the SHL due to lack of proper representation of convection and resulting cold pools in climate models. For instance (Evan et al., 2015) showed that the intensification in the SHL and resulting recovery in the Sahel precipitation to be linked with greenhouse forcing of water vapour. Marsham et al., 2016 (and Chapter IV of this thesis) pointed the importance of dust and water vapour in controlling the daily variability of radiative budget of the SHL. Therefore there is a need for better representation of cold pools, which are sources of large water vapour and dust emission, in climate models to better understand variability and predict future of the SHL. From the results of comparison of observation with reanalysis, there are two major areas models need to improve. The primary importance is improving models capability in resolving convection possibly development of improved parametrization for convection and based on that building objectively generalized method of identification for cold pools in models (Drager and van den Heever, 2017). Secondly the model physics which involves calculation of radiative processes due to water vapour, dust, and cloud needs to be improved. Particularly there is a chronic need to improve cloud representation and calculation of it

radiative effect which is challenging currently in models (Hannak et al., 2017). The bias in observed net surface longwave flux compared with MERRA suggests that in some cases the resulting error is not due to atmospheric constituents (such as cloud and dust) which have known radiative effect. Other possible source of uncertainty could be due to error in surface optical characteristics (Haywood et al., 2005). All these needs to be addressed for better representation of the climate system of the SHL in models.

The method I presented to identify cold pools is not free from uncertainty and could possibly miss cold pool cases. As I mentioned previously, the cold pool processes can be missed due to the choice of minimum thresholds. Related with this, I considered cases which result in increase in dew point temperature even if this is best approximation for arid environment. Atmospheric moisture could mask dust in SEVIRI observation (Brindley et al., 2012) and therefore may not detect haboobs (Allen et al., 2013). It is also challenging to identify active deep convective systems from SEVIRI imagery making it confusing in the identification of cold pools (Ashpole and Washington, 2013). This can be improved by using microwave satellite imagery to identify deep convection (Redl et al., 2015) which are possible future work. However my results present useful information on the properties and frequency of cold pools in the SHL region which are required for model evaluation. This research helps in providing the first hand information required to evaluate models simulations. However an extensive research is required to fully account the contribution of cold pools to transport of dust and moisture in the region and their associated impact on the dynamics.

CHAPTER VI

6 Summary Discussion and Future Work

6.1 Summary

Saharan heat low region is proved to play key role in the initiation and development of the West African Monsoon system (Sultan and Janicot, 2003). During summer a low pressure system is developed due to the intense heating over the Sahara (Lavaysse et al., 2009). As a result a low level cyclonic circulation is formed (Racz and Smith, 1999) and moist cold air is advected from the surrounding regions to the heat low, significantly from WAM in southern fringe of the Saharan desert(Grams et al., 2010;Lavaysse et al., 2010a;Parker et al., 2005;Sultan et al., 2003;Vizy and Cook, 2009). Moist air advected from the surrounding areas along with prevailing hot surface temperature creates a favourable condition for convection (Knippertz et al., 2009; Marsham et al., 2013a). The resulting precipitation however evaporates before reaching the ground and down drafting cold air current density is formed (Charba, 1974;Simpson, 1969) propagating at high speed and initiating emission of large wall of dust locally known as haboobs (Allen et al., 2013). Some of these processes are either totally missing or misrepresented in climate models (Evan et al., 2014; Heinold et al., 2013; Knippertz et al., 2009;Marsham et al., 2013a) and introducing errors in model simulations. Specifically amount of dust and water vapour are underrepresented in models. This will lead to further uncertainty on the radiative effect of dust and water vapour in the region.

The main aim of this thesis is to improve our understanding of key processes involved in the development, maintenance, and variability of the SHL. This enables us identify the key features that models are lacking to accurately represent present and past climate of the region. It also gives a way to assess its impact on regional scale which in turn will improve prediction of monsoon flow and associated rain fall in the Sahel region on which millions of people depend for their livelihood. This thesis has three major research chapters. In the first research chapter I presented a comprehensive analysis of the energy and moisture budget of the Saharan heat low region. Secondly, as a first step towards assessing biases in climate model outputs, I have investigated the roles of dust and water vapour in controlling variability of energy budget of the region using observational data. Last I have characterised occurrence

frequency and distribution of cold pools that are shown to be important features in transport of dust and moisture into Saharan Heat Low region.

To this end, I used various data sources including reanalysis output, recent in-situ measurement data, and satellite data. Heat and moisture budget of the heat low region is derived from the thermodynamic equation and continuity equation respectively using three dimensional temperature and wind fields. Radiative effects of dust and water vapour are calculated using radiative transfer model. I characterised the frequency and distribution of cold pools with a unique detection algorithm using data from the AWS. The main results of the research questions are summarized below for each of the three chapters.

Summary of Chapter III

One of main motivating reason for doing this research is the recent increases in trends of temperature and precipitation compared with the draught in the 1980s over the Sahel (Dong and Suton 2016; Evan et al., 2015; Lavaysse et al., 2016). It is suggested that this could be due to the intensification of the Saharan Heat Low. In chapter III I investigated heat and moisture budget and its variability in the Saharan heat low region. The long-time (1979-2014) JJA mean heat and moisture is derived using the three commonly used reanalyses models. I find that all models have consistent representation of the heat and moisture budgets on a larger temporal and spatial scales. In all cases I found average horizontal temperature advection from both mean and transient flows plays important role in cooling the SHL the former being more important. However these results will notably deviate from each other on smaller regional scales. The long term variability in the intensity is verified with the 1980's being weak heat low years while in the past two decades there is intensification of the SHL. To explore the differences in heat and moisture budgets, I identified two contrasting periods of the mean of three warmest heat and the mean of three coolest seasons and derived the average heat and moisture budget for composite of the two contrasting periods. During the weak heat low years cooling from horizontal temperature advection is found to be larger than that of the strong heat low years. To the contrary I found more moisture advected during the strong heat low periods compared with weak heat low periods. No significant difference is observed in the diabatic heat between the strong and weak SHL periods. Specifically I find small correlation between intensity of the SHL and surface sensible heat flux.

I infer from this (i) the damping, negative feedback process linking the heat low intensity to the magnitude of cooling from the mean convergent circulation is perturbed

at inter-annual timescales i.e. the weaker SHL years actually have stronger advective cooling, likely due to circulation anomalies driven by processes outside the SHL itself (ii) Inter-annual variability in SHL temperature and intensity is related more to the advective processes described above rather than total diabatic heating. Evan et al., 2015 propose a positive feedback process to explain the decadal increasing trend in SHL intensity, in which a stronger SHL and associated mean circulation drives greater import of water vapour into the SHL core and radiative warming. I have also confirmed their assertion that there is an increased moisture during the strong SHL years (fig. 3.11) which will lead to the strengthening of SHL through the greenhouse gas effect.

Overall reanalyses models are able to represent the heat and moisture budget of the SHL on a larger domain. However notable difference are observed when one considers the detailed processes to smaller regional scales. This is evident from the vertical profile of heating rates averaged over the SHL region. The differences in these results could be due to the different core model physics and assimilation methods involved in each model. Climate models still lack to represent the detailed heat and moisture budget particularly on a regional scale. In line to this models are known to misrepresent mesoscale convective cold pools, (see chapter V) which affects the moisture budget to first order and heating/drying rates subsequently. Furthermore models use climatological aerosol loading which is known to underestimate aerosol loadings. Aerosol effects on variability on a smaller time scale are not thus accounted reanalyses models. However, Marsham et al. 2015 find dust aerosol variability dominates surface rather than top of atmosphere radiative fluxes with net surface radiative sensitivity of ~13 W m^{-2} AOD^{-1}. An improved representation of aerosols is thus imperative for a comprehensive understanding all physical processes involved with in the SHL.

I have presented a comprehensive analysis of the heat and moisture budget of SHL in chapter-III. However my analysis is made during summer period of time limited over core heat low area. Since SHL has strong link with the WAM and Ocean SSTs, a wider analysis that covers a larger domain on land and ocean is essential to give a complete description of causes and effects that are being observed in the region. It is further possible to infer dynamical aspects from diabatic heating diagnosis. I was not able to do it in this thesis because of time shortage. But I would like to further investigate these and other related features in future projects, which are described in section 6.3.

Summary of Chapter IV

A major source of uncertainty in climate models arises from lack of accurate representation of aerosols impact on the climate. Among the several reasons for the uncertainties in aerosols climate impact some are: the rather non-uniform distribution of aerosols in the globe, difficult nature of representing processes involved in emission mechanisms of aerosols, and challenges in calculation of radiative effects due to lack of geometrical and optical properties of aerosols. In Sahara dust aerosol is known to play significant role in modulating the climate of the region. Despite its importance on influencing the regions climate, accurate quantitative values of its radiative forcing is far from being known accurately. In addition to dust water vapour is also shown to have a pivotal role in controlling the mean state and variability of the heat budget of the SHL (Evan et al., 2015; Marsham et al., 2016). Recent publications suggest the important roles of moisture in controlling (1) diurnal variability of the radiative budget (Marsham et al., 2016) and (2) the decadal variability in the intensity of SHL (Evan et al., 2015). Therefore improving quantitative values of the radiative effect of dust and water vapour and their role in controlling the climate of the region is vital.

In this chapter, I derived the radiative effect of dust aerosol and water vapour at surface, top of atmosphere, and within atmospheric over a one month period at BBM. On average the SHL has large net radiative positive surplus at the surface, 83 W m^{-2}, relatively smaller but also positive TOA net radiative surplus, 31 W m^{-2}, and therefore large atmospheric radiative divergence of 52 W m^{-2}. The results I found suggest that dust and water vapour have similar radiative forcing at TOA while dust is found to have a stronger surface radiative cooling effect compared with heating effect of water vapour. The radiative effects of dust and water vapour are separated by undergoing sensitivity experiments. I found for every change in one standard deviation of dust AOD DRE of 7 W m^{-2}, -11 W m^{-2}, and 22 W m^{-2} at surface, TOA, and within the atmosphere respectively. The contrasting TOA heating and surface cooling effects of dust results in considerable atmospheric convergence heating the PBL below 500 hPa by up to 0.6 K Day^{-1}. However episodic and synoptic dust events can result in atmospheric heating as large as 6 K Day^{-1}. Water vapour has small radiative convergence due to its similar TOA and surface radiative effects in both magnitude and sign. DRE of water vapour at surface, TOA and within atmosphere is 8 W m^{-2}, 6 W m^{-2}, and 1 W m^{-2} per unit change in one standard deviation of column integrated water vapour respectively. My results suggest that the effect of dust is larger than what it is believed to be previously in controlling the day to day variability and climate change of the region. It is therefore essential to include these updated effects of dust in climate models.

RT codes are simplified to undergo different experiments. But this comes at its own disadvantage. The main limitation of standalone radiative transfer calculations is

their inability to account feedback from a radiative active component of the atmosphere. This can however be improved by using climate models that provide simulation options to run with and without feedback of aerosols.

Summary of Chapter V

The occurrence frequency and spatial distributions of cold pools in the Sahara heat low region are assessed in Chapter-V .For this I implemented a unique identification method which can effectively detect cold pools when the criteria set is fulfilled. Once the cold pools are identified, they are further confirmed by looking at SEVIRI satellite imagery for emission of dust or deep convective cloud. I found two sources of cold pool formation: (I) from convection fed by moisture carried from the WAM flow and (ii) from convection triggered over the North most Africa across the Atlas. Based on that I identified 145 cold pool events in eight AWS stations during, 2011, and 2012. However I expect the actual number to be more than what I found here since there times when there is no measurement and times when measured data were not accurate. I found the mean changes of 7.2 K in dew point temperature and 3.4 m s^{-1} in wind speed and average wind speed of 7 m s^{-1} associated with passage of cold pools. In this work, I have not considered temperature as selection criteria which is used in previous research publications. Temperature in general is found to drop as a result of cold pool passage. Nevertheless, several cold pools events resulting in rise in temperature are also identified. The magnitude of cold pools, measured by the changes in atmospheric variables as a result of their passage, varies both on season and location. The month July is the time with the most cold pool events identified compared with other months. From 111 cold pools identified in 2012 from June to September, 36 occurred during July, 33 occurred each in June and August, and 9 occurred in September. It is also in the month July that cold pools with strong signatures are identified. Moreover more cold pools are identified in the southern edge of the domain which is close to the monsoon flow. I identified 32 cold pools at AWS 134 compared with 18 cold pools identified at AWS 138. (refer to fig 5.2 for the location of this two stations). On average Cold pools triggered by monsoon surge are comparatively stronger than those triggered over the Atlas. Furthermore monsoon triggered cold pools are often associated with emission of dust as confirmed by SEVIRI imagery. I have finally compared measurements with reanalyses model results. Moisture is not always underestimated in reanalyses simulations as I confirmed in some stations moisture produced in models greater than what is being observed. Large discrepancy in surface net longwave flux exists between models and reanalyses

outputs. This difference is not necessarily associated with error in moisture or other factors (eg. cloud, dust) in the atmosphere. LW flux in measurement has uncertainity up to ~50 W m^{-2} which could partly explain the discrepancy to model values.

There is no standard or reference identification method for cold pools. This is because characteristics of cold pools could vary depending on location and time of occurrence. In this chapter I used SEVIRI satellite imagery for dust or convective cloud as confirmation for cold pools when the thresholds for selection criteria for atmospheric variables are satisfied. However dust is not visible when covered by higher level cloud. Moreover it is challenging to distinguish convective cloud from high level cloud from SEVIRI images. For a more robust cold pool identification process, an additional source would be beneficial for deep is essential for a more robust cold pool identification method.

6.2 Discussion and Implications

The climate system of SHL is influenced by a number of small scale and large scale dynamical processes. The most dominant forces shaping the regions climate system are the north-easterly harmattan flow and south-westerly monsoon flow which in turn are influenced by the strength of the SHL (Schepanski et al., 2017). The strength of the heat low itself is influenced by dust loading and moisture advected into the region (Evan, Flamant, et al., 2015) by primarily from monsoon flow and mesoscale convective cold pools. The future climate of the region is thus strongly influenced by variabilities in circulation and intensity of the SHL. I have shown in this thesis and also previous publications (Cook & Vizy, 2015; Evan, Flamant, et al., 2015; Lavaysse et al., 2016) increasing trend in the intensity of SHL. The causes of recent intensification of the SHL is debatable and needs further investigation however the combined or separate effects due changes in SST, increase in greenhouse gases concentration, and/or enhanced moisture advection in SHL are likely drivers. Regardless of the exact cause, the intensification of the SHL deepens the temperature gradient between the Sahara and Gulf of Guinea. This increased temperature gradient drives strengthened flows of WAM enhancing precipitation over the Sahel region. Variability across various time scales within the SHL will therefore lead to implied changes in the magnitude of monsoon flow and thus associated Sahel precipitation (Evan, Flamant, et al., 2015; Lavaysse et al., 2010). If the warming trends of the SHL continues at the present or higher rate due to future increase of greenhouse gases concentration, Sahel precipitation will likely increase in the future.

Sahel rainfall is also influenced by global climate patterns such as Atlantic and Mediterranean SSTs (Sheen et al., 2017). To understand the future Sahel rainfall, it is therefore imperial to undergo an integrated research that consists different land and atmospheric components both on regional and global scale. I have shown in this thesis that climate models despite capturing the overall picture of the climate system of the region, the uncertainty on reproducing detailed dynamical and thermodynamical processes and associated variability is still large. Models still need to improve in representation of the climate system and associated variability in the SHL. Observational data in the region both on temporal and spatial scales are not sufficient to give a detailed analysis of climate system of the region. A combined effort of improved model representation of the climate of the region abetted by observational data is therefore a necessity to improve our understanding of the physical processes of the past and predict the future. This needs to be addressed if we have to rely on models especially for future projections.

Another important component of the Sahara desert is dust. Here I considered regional radiative impact of dust over a one-month period. I have shown that dust plays significant role in controlling the energy budget of SHL region. That is dust has strong SW absorption during the daytime warming the troposphere that leads to thickening in depth of boundary layer due to increased vertical mixing (Lavaysse et al., 2011). Further I have shown dust has a strong surface cooling basically from blocking of incoming solar radiation. The radiative effects of dust will have implications on the circulation of the region particularly of the WAM summer features (N'Datchoh et al., 2018; Zhao et al., 2011). Previous researches documented that dust has a weakening effect on the northward penetration of the WAM flow and westward shift of AEJ (N'Datchoh et al., 2018). The weakening of WAM flow will lead to reduced precipitation over the Sahel region. In addition to its impact on the mean flow, dust is also shown to influence the diurnal variability of precipitation (Zhao et al., 2011). That is during daytime strong shortwave absorption increasing atmospheric stability and thus inhibiting convection while during nighttime surface warming and atmospheric cooling from LW emission reducing atmospheric stability leading to anomalous warming over the land surface and atmosphere below dust layer therefore creating favourable conditions for nocturnal precipitation. Moreover, dust has a far-reaching global influence ranging from its inhibiting impact on storm formation over the Atlantic Ocean (Dunion & Velden, 2004) to influencing the ecosystem in the Amazon and northern Atlantic by serving as fertilizer upon deposition (Bristow et al., 2010; Jickells et al., 2005).

Dust emission and transport in the Sahara desert shows wide range of variability from diurnal to decadal time scales (Chaboureau et al., 2007; Evan & Mukhopadhyay, 2010). In line with this recent research findings suggest pattern of changes in dust amount with elevated periods of dustiness during the 70s and 80s and less dustiness periods in 2000s (Evan et al., 2016). Further model predictions project less dustiness in the future Sahara as a consequence the current global warming (Evan et al., 2016). The implications of less dusty future are positive for the people living in the Sahel region. It is suggested the current global warming if continued pushes the ITD northward which could lead to future greening of the Sahara desert (Pausata et al., 2017) back to what is believed to be its state thousands of years ago. To the contrary, the projected less dustiness will have adverse consequences to the people living in the Americas due to stronger tropical cyclones and less deposition in the Amazon (Pausata et al., 2017).

The above important features clearly show the crucial role dust plays in the circulation and energy budget of the region and hence the need to implement improved dust modules climate models. There are two important aspects that need urgent attention in modelling of dust. First accurate calculation of the radiative effect of dust which requires precise representation of geometrical and optical properties of dust aerosols in models. For this advanced in-situ measurements accounting details of different types of dust at various altitudes needs to be collected. Second there is a need to develop improved dust emission schemes with accurate capabilities of simulating emission and transport of dust. In this way it is possible to improve the modelling and thus accurate calculation of dust radiative effect and prediction of dust loading and variability in the atmosphere by models.

6.3 Future works

In general, lack of complete observational data due to the harsh weather conditions in the heart of the Sahara desert is a major setback to research. FENNEC field campaign during 2011 and 2012 has provided useful data in the remote locations of Sahara desert. However the data collection were not made in such a way that can be used for calculation of horizontal advection of temperature and moisture. Aircraft flights for the dropsondes designed in a similar way as those described in Eric Smith, 1985 would be great advantage for the calculation heat and moisture budget from observations. In addition to atmospheric variables, measurements should include surface characteristics, dust distribution, dust optical and geometrical properties, and cloud distribution and properties. A comprehensive set data including surface,

atmosphere, and ocean is key to disclose what remains to be challenging to explain otherwise. Below I summarize some of the future works I would like to carry out as extension to what has been done in this thesis.

The impact of ocean on land (teleconnection) is one of the major research field of our times. The details of variability and connection of SHL with the WAM flow and the various time scale changes in ocean SST is not yet understood. In relation to this there is a rich source of evidence that variability in West African Monsoon is strongly coupled with variability in tropical SST (Janicot et al., 1998; E. R. Martin & Thorncroft, 2014; Mohino et al., 2011). However there is considerable uncertainty both on magnitude and sign of relationship between variability in WAM (and trends in Sahel precipitation) and changes in SST. Diabatic heating, the main source of energy driving circulation, is important quantity to investigate land-atmosphere and land-ocean interactions.

In chapter III I determined the heat and moisture budget of the Saharan heat low region. I would like to extend the this work to explore roles of changes in SST on variability of SHL informed by studying the heat and moisture budget of the larger domain which includes land and ocean on the west side of Sahara on longer temporal scales. Here I derived heat and moisture budget from three reanalyses model output. I would like to further study the important dynamical and thermodynamical processes using simulation of coupled meteorology and aerosol/chemistry model WRF-Chem and RegCM. These regional models improve the representation and thus radiative effect of dust compared with reanalyses models that use climatological dust. By analysing different components of vertical and horizontal distributions diabatic heating, it is possible to infer processes that affect land-ocean circulations (G. M. Martin et al., 2017). This will present a more complete picture and thus improved understanding of the dynamics of the region.

A major component of this research focuses on dust impact on the climate. In chapter IV, I quantified the role of dust and water vapour on the SHL radiative budget using a standalone radiative transfer code. For that, I used different set of input dataset. I used Dubovik dust size distribution in the radiative transfer calculations. However, there are large uncertainties in some of the input dataset I used for simulation of RT code. For instance Dubovik dust size distribution is not an ideal representation of dust particularly close to the emission sources. Lack of accurate size distribution and optical properties of dust are the major sources of uncertainty in calculation of radiative impact of dust. In addition to uncertainties in optical properties, dust modules in climate models have limited number of bins representing dust. As a future project, I would like to implement an improved dust representation in WRF and

RegCM models by presenting an improved size distribution with more dust bins that best approximate the actual distribution of dust in the atmosphere. The use of climate models to calculate radiative effect of dust will further enable us to include the dynamic and thermodynamic feedback from dust.

Another important but challenging aspect causing uncertainty in the radiative calculations of the SHL is lack of data of cloud properties. In this thesis, I used cloud properties from reanalysis. However, reanalysis models miss cloud specifically those associated with convection. It is therefore essential to have measurements of cloud properties in order to give a complete and accurate radiative budget the Sahara heat low. Therefore, with accurate measurements of dust and cloud properties, it is possible to significantly reduce the uncertainty in the radiative budget of the region, and hence a major plan of my future work.

A shortcoming of the cold pool identification algorithm I used in this thesis is that SEVIRI imagery are not always reliable on detecting dust and convective cloud. Satellite microwave imagery are more reliable on detecting deep convective clouds, which are pre-coursers of cold pool outflows. This will increase the robustness of my cold pool detection method which is a possible future work. Having an improved cold pool identification method the next plan will be to study cold pools representation in regional models specifically using WRF-Chem and RegCM. Model evaluation of cold simulation has been studied by several authors for different locations (Heinold et al., 2013; Knippertz et al., 2009; Marsham et al., 2013). A case studies have also been conducted over the Sahara region (Provod et al., 2016). I would like to carry out a more rigorous evaluation of regional climate models performance in resolving cold pool characteristics. This includes comparison of the model simulations and observations at all AWS stations spread over the Sahara desert.

Furthermore I would like to study the contribution of cold pools to the emission of dust in the region. This has been studied previously by a number of authors. But all previous studies focus on limited locations. For instance Allan et al., 2013 showed that cold pools contribute to 30% of the total dust emitted during summer time at BBM. I would like to extend this to other AWS stations. Such studies are vital for attribution of cold pools in the emission of dust in the region. In doing so it will be possible to figure out the shortcomings of models and thus indicate ways via developers can be informed possible future improvements.

References

Allen, C. J. T., Washington, R. & Engelstaedter, S. 2013. Dust emission and transport mechanisms in the central Sahara: Fennec ground-based observations from Bordj Badji Mokhtar, June 2011. *Journal of Geophysical Research-Atmospheres,* 118**,** 6212-6232.

Ansell, C., Brindley, H. E., Pradhan, Y. & Saunders, R. 2014. Mineral dust aerosol net direct radiative effect during GERBILS field campaign period derived from SEVIRI and GERB. *Journal of Geophysical Research-Atmospheres,* 119**,** 4070-4086.

Ansmann, A., Tesche, M., Knippertz, P., Bierwirth, E., Althausen, D., Muller, D. & Schulz, O. 2009. Vertical profiling of convective dust plumes in southern Morocco during SAMUM. *Tellus Series B-Chemical and Physical Meteorology,* 61**,** 340-353.

Ansmann, A., Petzold, A., Kandler, K., Tegen, I., Wendisch, M., Muller, D., . . . Heintzenberg, J. (2011). Saharan Mineral Dust Experiments SAMUM-1 and SAMUM-2: what have we learned? *Tellus Series B-Chemical and Physical Meteorology, 63*(4), 403-429. doi:10.1111/j.1600-0889.2011.00555.x

Ashpole, I. & Washington, R. 2012. An automated dust detection using SEVIRI: A multiyear climatology of summertime dustiness in the central and western Sahara. *Journal of Geophysical Research-Atmospheres,* 117.

Ashpole, I. & Washington, R. 2013. A new high-resolution central and western Saharan summertime dust source map from automated satellite dust plume tracking. *Journal of Geophysical Research-Atmospheres,* 118**,** 6981-6995.

Balkanski, Y., Schulz, M., Claquin, T., & Guibert, S. (2007). Reevaluation of Mineral aerosol radiative forcings suggests a better agreement with satellite and AERONET data. *Atmospheric Chemistry and Physics, 7*, 81-95. doi:DOI 10.5194/acp-7-81-2007

Banks, J. R. & Brindley, H. E. 2013. Evaluation of MSG-SEVIRI mineral dust retrieval products over North Africa and the Middle East. *Remote Sensing of Environment,* 128**,** 58-73.

Banks, J. R., Brindley, H. E., Hobby, M. & Marsham, J. H. 2014. The daytime cycle in dust aerosol direct radiative effects observed in the central Sahara during the Fennec campaign in June 2011. *Journal of Geophysical Research-Atmospheres,* 119**,** 13861-13876.

Biasutti, M., Sobel, A. H., & Camargo, S. J. (2009). The Role of the Sahara Low in Summertime Sahel Rainfall Variability and Change in the CMIP3 Models. *Journal of Climate, 22*(21), 5755-5771. doi:10.1175/2009jcli2969.1

Birch, C. E., Marsham, J. H., Parker, D. J. & Taylor, C. M. 2014. The scale dependence and structure of convergence fields preceding the initiation of deep convection. *Geophysical Research Letters,* 41**,** 4769-4776.

Blake, D. W., Krishnamurti, T. N., Lownam, S. V., & Fein, J. S. (1983). Heat Low over the Saudi Arabian Desert during May 1979 (Summer Monex). *Monthly Weather Review, 111*(9), 1759-1775. doi:Doi 10.1175/1520-0493(1983)111<1759:Hlotsa>2.0.Co;2

Bounoua, L. & Krishnamurti, T. N. 1991. Thermodynamic Budget of the 5 Day Wave over the Saharan Desert during Summer. *Meteorology and Atmospheric Physics,* 47**,** 1-25.

Brindley, H., Knippertz, P., Ryder, C. & Ashpole, I. 2012. A critical evaluation of the ability of the Spinning Enhanced Visible and Infrared Imager (SEVIRI) thermal infrared red-green-blue rendering to identify dust events: Theoretical analysis. *Journal of Geophysical Research-Atmospheres,* 117.

Bristow, C. S., Hudson-Edwards, K. A. & Chappell, A. 2010. Fertilizing the Amazon and equatorial Atlantic with West African dust. *Geophysical Research Letters,* 37.

Chan, S. C. & Nigam, S. 2009. Residual Diagnosis of Diabatic Heating from ERA-40 and NCEP Reanalyses: Intercomparisons with TRMM. *Journal of Climate,* 22**,** 414-428.

Chaboureau, J. P., Tulet, P., & Mari, C. (2007). Diurnal cycle of dust and cirrus over West Africa as seen from Meteosat Second Generation satellite and a regional forecast model. *Geophysical Research Letters, 34*(2). doi:Artn L02822 10.1029/2006gl027771

Charba, J. 1974. Application of Gravity Current Model to Analysis of Squall-Line Gust Front. *Monthly Weather Review,* 102**,** 140-156.

Chauvin, F., Roehrig, R. & Lafore, J. P. 2010. Intraseasonal Variability of the Saharan Heat Low and Its Link with Midlatitudes. *Journal of Climate,* 23**,** 2544-2561.

Chou, C., Neelin, J. D. & Su, H. 2001. Ocean-atmosphere-land feedbacks in an idealized monsoon. *Quarterly Journal of the Royal Meteorological Society,* 127**,** 1869-1891.

Cook, K. H. & Vizy, E. K. 2015. Detection and Analysis of an Amplified Warming of the Sahara Desert. *Journal of Climate,* 28**,** 6560-6580.

Couvreux, F., Guichard, F., Bock, O., Campistron, B., Lafore, J. P. & Redelsperger, J. L. 2010. Synoptic variability of the monsoon flux over West Africa prior to the onset. *Quarterly Journal of the Royal Meteorological Society,* 136**,** 159-173.

Cuesta, J., Edouart, D., Mimouni, M., Flamant, P. H., Loth, C., Gibert, F., Marnas, F., Bouklila, A., Kharef, M., Ouchene, B., Kadi, M. & Flamant, C. 2008. Multiplatform observations of the seasonal evolution of the Saharan atmospheric boundary layer in Tamanrasset, Algeria, in the framework of the African Monsoon Multidisciplinary Analysis field campaign conducted in 2006. *Journal of Geophysical Research-Atmospheres,* 113.

Cuesta, J., Lavaysse, C., Flamant, C., Mimouni, M. & Knippertz, P. 2010. Northward bursts of the West African monsoon leading to rainfall over the Hoggar Massif, Algeria. *Quarterly Journal of the Royal Meteorological Society,* 136**,** 174-189.

Dee, D. P., Uppala, S. M., Simmons, A. J., Berrisford, P., Poli, P., Kobayashi, S., Andrae, U., Balmaseda, M. A., Balsamo, G., Bauer, P., Bechtold, P., Beljaars, A. C. M., van de Berg, L., Bidlot, J., Bormann, N., Delsol, C., Dragani, R., Fuentes, M., Geer, A. J., Haimberger, L., Healy, S. B., Hersbach, H., Holm, E. V., Isaksen, L., Kallberg, P., Kohler, M., Matricardi, M., McNally, A. P., Monge-Sanz, B. M., Morcrette, J. J., Park, B. K., Peubey, C., de Rosnay, P., Tavolato, C., Thepaut, J. N. & Vitart, F. 2011. The ERA-Interim reanalysis: configuration and performance of the data assimilation system. *Quarterly Journal of the Royal Meteorological Society,* 137**,** 553-597.

Dong, B. W., & Sutton, R. (2015). Dominant role of greenhouse-gas forcing in the recovery of Sahel rainfall. *Nature Climate Change, 5*(8), 757-U173. doi:10.1038/Nclimate2664

Drager, A. J. & van den Heever, S. C. 2017. Characterizing convective cold pools. *Journal of Advances in Modeling Earth Systems,* 9**,** 1091-1115.

Drobinski, P., Sultan, B. & Janicot, S. 2005. Role of the Hoggar massif in the West African monsoon onset. *Geophysical Research Letters,* 32.

Dubovik, O., Holben, B., Eck, T. F., Smirnov, A., Kaufman, Y. J., King, M. D., Tanre, D. & Slutsker, I. 2002. Variability of absorption and optical properties of key aerosol types observed in worldwide locations. *Journal of the Atmospheric Sciences,* 59**,** 590-608.

Dunion, J. P., & Velden, C. S. (2004). The impact of the Saharan air layer on Atlantic tropical cyclone activity. *Bulletin of the American Meteorological Society, 85*(3), 353-+. doi:10.1175/Bams-85-3-353

Edwards, J. M. & Slingo, A. 1996. Studies with a flexible new radiation code .1. Choosing a configuration for a large-scale model. *Quarterly Journal of the Royal Meteorological Society,* 122**,** 689-719.

Emmel, C., Knippertz, P. & Schulz, O. 2010. Climatology of convective density currents in the southern foothills of the Atlas Mountains. *Journal of Geophysical Research-Atmospheres,* 115.

Engelstaedter, S., Tegen, I. & Washington, R. 2006. North African dust emissions and transport. *Earth-Science Reviews,* 79**,** 73-100.

Engelstaedter, S., Washington, R., Flamant, C., Parker, D. J., Allen, C. J. T. & Todd, M. C. 2015. The Saharan heat low and moisture transport pathways in the central Sahara-Multiaircraft observations and Africa-LAM evaluation. *Journal of Geophysical Research-Atmospheres,* 120**,** 4417-4442.

Engerer, N. A., Stensrud, D. J. & Coniglio, M. C. 2008. Surface Characteristics of Observed Cold Pools. *Monthly Weather Review,* 136**,** 4839-4849.

Evan, A. T., Fiedler, S., Zhao, C., Menut, L., Schepanski, K., Flamant, C., & Doherty, O. (2015). Derivation of an observation-based map of North African dust emission. *Aeolian Research, 16*, 153-162. doi:10.1016/j.aeolia.2015.01.001

Evan, A. T., Flamant, C., Gaetani, M., & Guichard, F. (2016). The past, present and future of African dust. *Nature, 531*(7595), 493-+. doi:10.1038/nature17149

Evan, A. T., Flamant, C., Fiedler, S. & Doherty, O. 2014. An analysis of aeolian dust in climate models. *Geophysical Research Letters,* 41**,** 5996-6001.

Evan, A. T., Flamant, C., Lavaysse, C., Kocha, C. & Saci, A. 2015. Water Vapor-Forced Greenhouse Warming over the Sahara Desert and the Recent Recovery from the Sahelian Drought. *Journal of Climate,* 28**,** 108-123.

Evan, A. T., Foltz, G. R., Zhang, D. X. & Vimont, D. J. 2011. Influence of African dust on ocean-atmosphere variability in the tropical Atlantic. *Nature Geoscience,* 4**,** 762-765.

Evan, A. T., & Mukhopadhyay, S. (2010). African Dust over the Northern Tropical Atlantic: 1955-2008. *Journal of Applied Meteorology and Climatology, 49*(11), 2213-2229. doi:10.1175/2010jamc2485.1

Fiedler, S., Schepanski, K., Heinold, B., Knippertz, P. & Tegen, I. 2013. Climatology of nocturnal low-level jets over North Africa and implications for modeling mineral dust emission. *Journal of Geophysical Research-Atmospheres,* 118**,** 6100-6121.

Flamant, C., Knippertz, P., Parker, D. J., Chaboureau, J. P., Lavaysse, C., Agusti-Panareda, A. & Kergoat, L. 2009. The impact of a mesoscale convective system cold pool on the northward propagation of the intertropical discontinuity over West Africa. *Quarterly Journal of the Royal Meteorological Society,* 135**,** 139-159.

Garcia-Carreras, L., Marsham, J. H., Parker, D. J., Bain, C. L., Milton, S., Saci, A., Salah-Ferroudj, M., Ouchene, B. & Washington, R. 2013. The impact of convective cold pool outflows on model biases in the Sahara. *Geophysical Research Letters,* 40**,** 1647-1652.

Giannini, A., Salack, S., Lodoun, T., Ali, A., Gaye, A. T., & Ndiaye, O. (2013). A unifying view of climate change in the Sahel linking intra-seasonal, interannual and longer time scales. *Environmental Research Letters, 8*(2). doi:Artn 024010 10.1088/1748-9326/8/2/024010

Giannini, A., Saravanan, R., & Chang, P. (2003). Oceanic forcing of Sahel rainfall on interannual to interdecadal time scales. *Science, 302*(5647), 1027-1030. doi:10.1126/science.1089357

Goudie, A. S. (2014). Desert dust and human health disorders. *Environment International, 63*, 101-113. doi:10.1016/j.envint.2013.10.011

Grams, C. M., Jones, S. C., Marsham, J. H., Parker, D. J., Haywood, J. M. & Heuveline, V. 2010. The Atlantic Inflow to the Saharan heat low: Observations and Modelling. *Quarterly Journal of the Royal Meteorological Society,* 136**,** 125-140.

Greed, G., Haywood, J. M., Milton, S., Keil, A., Christopher, S., Gupta, P. & Highwood, E. J. 2008. Aerosol optical depths over North Africa: 2. Modeling and model validation. *Journal of Geophysical Research-Atmospheres,* 113.

Hagos, S. & Zhang, C. D. 2010. Diabatic heating, divergent circulation and moisture transport in the African monsoon system. *Quarterly Journal of the Royal Meteorological Society,* 136**,** 411-425.

Hagos, S. M. & Cook, K. H. 2008. Ocean warming and late-twientieth-century Sahel drought and recovery. *Journal of Climate,* 21**,** 3797-3814.

Hannak, L., Knippertz, P., Fink, A. H., Kniffka, A. & Pante, G. 2017. Why Do Global Climate Models Struggle to Represent Low-Level Clouds in the West African Summer Monsoon? *Journal of Climate,* 30**,** 1665-1687.

Harries, J. E., Russell, J. E., Hanafin, J. A., Brindley, H., Futyan, J., Rufus, J., Kellock, S., Matthews, G., Wrigley, R., Last, A., Mueller, J., Mossavati, R., Ashmall, J., Sawyer, E., Parker, D., Caldwell, M., Allan, P. M., Smith, A., Bates, M. J., Coan, B., Stewart, B. C., Lepine, D. R., Cornwall, L. A., Corney, D. R., Ricketts, M. J., Drummond, D., Smart, D., Cutler, R., Dewitte, S., Clerbaux, N., Gonzalez, L., Ipe, A., Bertrand, C., Joukoff, A., Crommelynck, D., Nelms, N., Llewellyn-Jones, D. T., Butcher, G., Smith, G. L., Szewczyk, Z. P., Mlynczak, P. E., Slingo, A., Allan, R. P. & Ringer, M. A. 2005. The geostationary Earth Radiation Budget Project. *Bulletin of the American Meteorological Society,* 86**,** 945-+.

Haywood, J. M., Allan, R. P., Culverwell, I., Slingo, T., Milton, S., Edwards, J. & Clerbaux, N. 2005. Can desert dust explain the outgoing longwave radiation anomaly over the Sahara during July 2003? *Journal of Geophysical Research-Atmospheres,* 110.

Haywood, J. M., Johnson, B. T., Osborne, S. R., Baran, A. J., Brooks, M., Milton, S. F., . . . Gupta, P. (2011). Motivation, rationale and key results from the GERBILS Saharan dust measurement campaign. *Quarterly Journal of the Royal Meteorological Society, 137*(658), 1106-1116. doi:10.1002/qj.797

Haywood, J. M., Pelon, J., Formenti, P., Bharmal, N., Brooks, M., Capes, G., . . . Tulet, P. (2008). Overview of the Dust and Biomass-burning Experiment and African Monsoon Multidisciplinary Analysis Special Observing Period-0. *Journal of Geophysical Research-Atmospheres, 113*. doi:Artn D00c1710.1029/2008jd010077

Heinold, B., Knippertz, P., Marsham, J. H., Fiedler, S., Dixon, N. S., Schepanski, K., Laurent, B. & Tegen, I. 2013. The role of deep convection and nocturnal low-level jets for dust emission in summertime West Africa: Estimates from convection-permitting simulations. *Journal of Geophysical Research-Atmospheres,* 118**,** 4385-4400.

Heintzenberg, J. (2009). The SAMUM-1 experiment over Southern Morocco: overview and introduction. *Tellus Series B-Chemical and Physical Meteorology, 61*(1), 2-11. doi:10.1111/j.1600-0889.2008.00403.x

Highwood, E. J., Haywood, J. M., Silverstone, M. D., Newman, S. M. & Taylor, J. P. 2003. Radiative properties and direct effect of Saharan dust measured by the C-130 aircraft during Saharan Dust Experiment (SHADE): 2. Terrestrial spectrum. *Journal of Geophysical Research-Atmospheres,* 108.

Hobby, M., Gascoyne, M., Marsham, J. H., Bart, M., Allen, C., Engelstaedter, S., Fadel, D. M., Gandega, A., Lane, R., McQuaid, J. B., Ouchene, B., Ouladichir, A., Parker, D. J., Rosenberg, P., Ferroudj, M. S., Saci, A., Seddik, F., Todd, M., Walker, D. & Washington, R. 2013. The Fennec Automatic Weather Station (AWS) Network: Monitoring the Saharan Climate System. *Journal of Atmospheric and Oceanic Technology,* 30**,** 709-724.

Holben, B. N., Eck, T. F., Slutsker, I., Tanre, D., Buis, J. P., Setzer, A., Vermote, E., Reagan, J. A., Kaufman, Y. J., Nakajima, T., Lavenu, F., Jankowiak, I. & Smirnov, A. 1998. AERONET - A federated instrument network and data archive for aerosol characterization. *Remote Sensing of Environment,* 66**,** 1-16.

Hoose, C., & Mohler, O. (2012). Heterogeneous ice nucleation on atmospheric aerosols: a review of results from laboratory experiments. *Atmospheric Chemistry and Physics, 12*(20), 9817-9854. doi:10.5194/acp-12-9817-2012

Huang, J. P., Wang, T. H., Wang, W. C., Li, Z. Q. & Yan, H. R. 2014. Climate effects of dust aerosols over East Asian arid and semiarid regions. *Journal of Geophysical Research-Atmospheres,* 119**,** 11398-11416.

Huneeus, N., Schulz, M., Balkanski, Y., Griesfeller, J., Prospero, J., Kinne, S., Bauer, S., Boucher, O., Chin, M., Dentener, F., Diehl, T., Easter, R., Fillmore, D., Ghan, S., Ginoux, P., Grini, A., Horowitz, L., Koch, D., Krol, M. C., Landing, W., Liu, X., Mahowald, N., Miller, R., Morcrette, J. J., Myhre, G., Penner, J., Perlwitz, J., Stier, P., Takemura, T. & Zender, C. S. 2011. Global dust model intercomparison in AeroCom phase I. *Atmospheric Chemistry and Physics,* 11**,** 7781-7816.

Janicot, S., Harzallah, A., Fontaine, B., & Moron, V. (1998). West African monsoon dynamics and eastern equatorial Atlantic and Pacific SST anomalies (1970-88). *Journal of Climate, 11*(8), 1874-1882. doi:Doi 10.1175/1520-0442-11.8.1874

Jickells, T. D., An, Z. S., Andersen, K. K., Baker, A. R., Bergametti, G., Brooks, N., Cao, J. J., Boyd, P. W., Duce, R. A., Hunter, K. A., Kawahata, H., Kubilay, N., laRoche, J., Liss, P. S., Mahowald, N., Prospero, J. M., Ridgwell, A. J., Tegen, I. & Torres, R. 2005. Global iron connections between desert dust, ocean biogeochemistry, and climate. *Science,* 308**,** 67-71.

Kanamitsu, M., Ebisuzaki, W., Woollen, J., Yang, S. K., Hnilo, J. J., Fiorino, M. & Potter, G. L. 2002. NCEP-DOE AMIP-II reanalysis (R-2). *Bulletin of the American Meteorological Society,* 83**,** 1631-1643.

Karam, D. B., Flamant, C., Tulet, P., Chaboureau, J. P., Dabas, A. & Todd, M. C. 2009. Estimate of Sahelian dust emissions in the intertropical discontinuity region of the West African Monsoon. *Journal of Geophysical Research-Atmospheres,* 114.

Karam, D. B., Williams, E., Janiga, M., Flamant, C., McGraw-Herdeg, M., Cuesta, J., Auby, A. & Thorncroft, C. 2014. Synoptic-scale dust emissions over the Sahara Desert initiated by a moist convective cold pool in early August 2006. *Quarterly Journal of the Royal Meteorological Society,* 140**,** 2591-2607.

Knippertz, P. & Todd, M. C. 2012. Mineral Dust Aerosols over the Sahara: Meteorological Controls on Emission and Transport and Implications for Modeling. *Reviews of Geophysics,* 50.

Knippertz, P., Trentmann, J. & Seifert, A. 2009. High-resolution simulations of convective cold pools over the northwestern Sahara. *Journal of Geophysical Research-Atmospheres,* 114.

Kok, J. F., Ridley, D. A., Zhou, Q., Miller, R. L., Zhao, C., Heald, C. L., Ward, D. S., Albani, S. & Haustein, K. 2017. Smaller desert dust cooling effect estimated from analysis of dust size and abundance. *Nature Geoscience,* 10**,** 274-+.

Lafore, J. P., Flamant, C., Giraud, V., Guichard, F., Knippertz, P., Mahfouf, J. F., Mascart, P. & Williams, E. R. 2010. Introduction to the AMMA Special Issue on 'Advances in understanding atmospheric processes over West Africa through the AMMA field campaign'. *Quarterly Journal of the Royal Meteorological Society,* 136**,** 2-7.

Lavaysse, C. (2015). Saharan desert warming. *Nature Climate Change, 5*(9), 807-808. doi:DOI 10.1038/nclimate2773

Lavaysse, C., Chaboureau, J. P. & Flamant, C. 2011. Dust impact on the West African heat low in summertime. *Quarterly Journal of the Royal Meteorological Society,* 137**,** 1227-1240.

Lavaysse, C., Flamant, C., Evan, A., Janicot, S. & Gaetani, M. 2016. Recent climatological trend of the Saharan heat low and its impact on the West African climate. *Climate Dynamics,* 47**,** 3479-3498.

Lavaysse, C., Flamant, C. & Janicot, S. 2010a. Regional-scale convection patterns during strong and weak phases of the Saharan heat low. *Atmospheric Science Letters,* 11**,** 255-264.

Lavaysse, C., Flamant, C., Janicot, S. & Knippertz, P. 2010b. Links between African easterly waves, midlatitude circulation and intraseasonal pulsations of the West African heat low. *Quarterly Journal of the Royal Meteorological Society,* 136**,** 141-158.

Lavaysse, C., Flamant, C., Janicot, S., Parker, D. J., Lafore, J. P., Sultan, B. & Pelon, J. 2009. Seasonal evolution of the West African heat low: a climatological perspective. *Climate Dynamics,* 33**,** 313-330.

Lensky, I. M. & Rosenfeld, D. 2008. Clouds-Aerosols-Precipitation Satellite Analysis Tool (CAPSAT). *Atmospheric Chemistry and Physics,* 8**,** 6739-6753.

Liu, Z. Y., Vaughan, M., Winker, D., Kittaka, C., Getzewich, B., Kuehn, R., Omar, A., Powell, K., Trepte, C. & Hostetler, C. 2009. The CALIPSO Lidar Cloud and Aerosol Discrimination: Version 2 Algorithm and Initial Assessment of Performance. *Journal of Atmospheric and Oceanic Technology,* 26**,** 1198-1213.

Loeb, N. G., Wielicki, B. A., Doelling, D. R., Smith, G. L., Keyes, D. F., Kato, S., Manalo-Smith, N. & Wong, T. 2009. Toward Optimal Closure of the Earth's Top-of-Atmosphere Radiation Budget. *Journal of Climate,* 22**,** 748-766.

Marsham, J. H., Dixon, N. S., Garcia-Carreras, L., Lister, G. M. S., Parker, D. J., Knippertz, P. & Birch, C. E. 2013a. The role of moist convection in the West African monsoon system: Insights from continental-scale convection-permitting simulations. *Geophysical Research Letters,* 40**,** 1843-1849.

Marsham, J. H., Hobby, M., Allen, C. J. T., Banks, J. R., Bart, M., Brooks, B. J., Cavazos-Guerra, C., Engelstaedter, S., Gascoyne, M., Lima, A. R., Martins, J. V., McQuaid, J. B., O'Leary, A., Ouchene, B., Ouladichir, A., Parker, D. J., Saci, A., Salah-Ferroudj, M., Todd, M. C. & Washington, R. 2013b. Meteorology and dust in the central Sahara: Observations from Fennec supersite-1 during the June 2011 Intensive Observation Period. *Journal of Geophysical Research-Atmospheres,* 118**,** 4069-4089.

Marsham, J. H., Parker, D. J., Todd, M. C., Banks, J. R., Brindley, H. E., Garcia-Carreras, L., Roberts, A. J. & Ryder, C. L. 2016. The contrasting roles of water and dust in controlling daily variations in radiative heating of the summertime Saharan heat low. *Atmospheric Chemistry and Physics,* 16**,** 3563-3575.

Martin, E. R. & Thorncroft, C. D. 2014. The impact of the AMO on the West African monsoon annual cycle. *Quarterly Journal of the Royal Meteorological Society,* 140**,** 31-46.

Martin, E. R., Thorncroft, C., & Booth, B. B. B. (2014). The Multidecadal Atlantic SST-Sahel Rainfall Teleconnection in CMIP5 Simulations. *Journal of Climate, 27*(2), 784-806. doi:10.1175/Jcli-D-13-00242.1

Martin, G. M., Peyrille, P., Roehrig, R., Rio, C., Caian, M., Bellon, G., Codron, F., Lafore, J. P., Poan, D. E. & Idelkadi, A. 2017. Understanding the West African Monsoon from the analysis of diabatic heating distributions as simulated by climate models. *Journal of Advances in Modeling Earth Systems,* 9**,** 239-270.

McConnell, C. L., Highwood, E. J., Coe, H., Formenti, P., Anderson, B., Osborne, S., . . . Harrison, M. A. J. (2008). Seasonal variations of the physical and optical characteristics of Saharan dust: Results from the Dust Outflow and Deposition to the Ocean (DODO) experiment. *Journal of Geophysical Research-Atmospheres, 113*(D14). doi:Artn D14s05 10.1029/2007jd009606

Mekonnen, A., Thorncroft, C. D. & Aiyyer, A. R. 2006. Analysis of convection and its association with African easterly waves. *Journal of Climate,* 19**,** 5405-5421.

Messager, C., Parker, D. J., Reitebuch, O., Agusti-Panareda, A., Taylor, C. M. & Cuesta, J. 2010a. Structure and dynamics of the Saharan atmospheric boundary layer during the West African monsoon onset: Observations and analyses from the research flights of 14 and 17 July 2006. *Quarterly Journal of the Royal Meteorological Society,* 136**,** 107-124.

Messager, E., Lordkipanidze, D., Delhon, C. & Ferring, C. R. 2010b. Palaeoecological implications of the Lower Pleistocene phytolith record from the Dmanisi Site (Georgia). *Palaeogeography Palaeoclimatology Palaeoecology,* 288**,** 1-13.

Miller, S. D., Kuciauskas, A. P., Liu, M., Ji, Q., Reid, J. S., Breed, D. W., Walker, A. L. & Al Mandoos, A. 2008. Haboob dust storms of the southern Arabian Peninsula. *Journal of Geophysical Research-Atmospheres,* 113.

Mishchenko, M. I., Lacis, A. A., Carlson, B. E., & Travis, L. D. (1995). Nonsphericity of Dust-Like Tropospheric Aerosols - Implications for Aerosol Remote-Sensing and Climate Modeling. *Geophysical Research Letters, 22*(9), 1077-1080. doi:Doi 10.1029/95gl00798

Mohino, E., Rodriguez-Fonseca, B., Mechoso, C. R., Gervois, S., Ruti, P., & Chauvin, F. (2011). Impacts of the Tropical Pacific/Indian Oceans on the Seasonal Cycle of the West African Monsoon. *Journal of Climate, 24*(15), 3878-3891. doi:10.1175/2011jcli3988.1

Mulcahy, J. P., Walters, D. N., Bellouin, N. & Milton, S. F. 2014. Impacts of increasing the aerosol complexity in the Met Office global numerical weather prediction model. *Atmospheric Chemistry and Physics,* 14**,** 4749-4778.

Muller, T., Schladitz, A., Massling, A., Kaaden, N., Kandler, K. & Wiedensohler, A. 2009. Spectral absorption coefficients and imaginary parts of refractive indices of Saharan dust during SAMUM-1. *Tellus Series B-Chemical and Physical Meteorology,* 61**,** 79-95.

Myhre, G., Shindell, D., Breon, F. M., Collins, W., Fuglestvedt, J., Huang, J. P., . . . Young, P. (2014). Anthropogenic and Natural Radiative Forcing. *Climate Change 2013: The Physical Science Basis*, 659-740.

N'Datchoh, E. T., Diallo, I., Konare, A., Silue, S., Ogunjobi, K. O., Diedhiou, A., & Doumbia, M. (2018). Dust induced changes on the West African summer monsoon features. *International Journal of Climatology, 38*(1), 452-466. doi:10.1002/joc.5187

Oke, T. R. 1987. *Boundary layer climates,* London, Methuen.

Osborne, S. R., Baran, A. J., Johnson, B. T., Haywood, J. M., Hesse, E. & Newman, S. 2011. Short-wave and long-wave radiative properties of Saharan dust aerosol. *Quarterly Journal of the Royal Meteorological Society,* 137**,** 1149-1167.

Osipov, S., Stenchikov, G., Brindley, H. & Banks, J. 2015. Diurnal cycle of the dust instantaneous direct radiative forcing over the Arabian Peninsula. *Atmospheric Chemistry and Physics,* 15**,** 9537-9553.

Otto, S., Bierwirth, E., Weinzierl, B., Kandler, K., Esselborn, M., Tesche, M., Schladitz, A., Wendisch, M. & Trautmann, T. 2009. Solar radiative effects of a Saharan dust plume observed during SAMUM assuming spheroidal model particles. *Tellus Series B-Chemical and Physical Meteorology,* 61**,** 270-296.

Otto, S., de Reus, M., Trautmann, T., Thomas, A., Wendisch, M. & Borrmann, S. 2007. Atmospheric radiative effects of an in situ measured Saharan dust plume and the role of large particles. *Atmospheric Chemistry and Physics,* 7**,** 4887-4903.

Otto, S., Trautmann, T. & Wendisch, M. 2011. On realistic size equivalence and shape of spheroidal Saharan mineral dust particles applied in solar and thermal radiative transfer calculations. *Atmospheric Chemistry and Physics,* 11**,** 4469-4490.

Parker, D. J., Burton, R. R., Diongue-Niang, A., Ellis, R. J., Felton, M., Taylor, C. M., Thorncroft, C. D., Bessemoulin, P. & Tompkins, A. M. 2005. The diurnal cycle of the West African monsoon circulation. *Quarterly Journal of the Royal Meteorological Society,* 131**,** 2839-2860.

Pausata, F. S. R., Emanuel, K. A., Chiacchio, M., Diro, G. T., Zhang, Q., Sushama, L., . . . Donnelly, J. P. (2017). Tropical cyclone activity enhanced by Sahara greening and reduced dust emissions during the African Humid Period. *Proceedings of the National Academy of Sciences of the United States of America, 114*(24), 6221-6226. doi:10.1073/pnas.1619111114

Petzold, A., Rasp, K., Weinzierl, B., Esselborn, M., Hamburger, T., Dornbrack, A., Kandler, K., Schutz, L., Knippertz, P., Fiebig, M. & Virkkula, A. 2009. Saharan dust absorption and refractive index from aircraft-based observations during SAMUM 2006. *Tellus Series B-Chemical and Physical Meteorology,* 61**,** 118-130.

Peyrille, P. & Lafore, J. P. 2007. An idealized two-dimensional framework to study the West African monsoon. Part II: Large-scale advection and the diurnal cycle. *Journal of the Atmospheric Sciences,* 64**,** 2783-2803.

Prospero, J. M., Ginoux, P., Torres, O., Nicholson, S. E. & Gill, T. E. 2002. Environmental characterization of global sources of atmospheric soil dust identified with the Nimbus 7 Total Ozone Mapping Spectrometer (TOMS) absorbing aerosol product. *Reviews of Geophysics,* 40.

Provod, M., Marsham, J. H., Parker, D. J. & Birch, C. E. 2016. A Characterization of Cold Pools in the West African Sahel. *Monthly Weather Review,* 144**,** 1923-1934.

Racz, Z. & Smith, R. K. 1999. The dynamics of heat lows. *Quarterly Journal of the Royal Meteorological Society,* 125**,** 225-252.

Randles, C. A., Kinne, S., Myhre, G., Schulz, M., Stier, P., Fischer, J., Doppler, L., Highwood, E., Ryder, C., Harris, B., Huttunen, J., Ma, Y., Pinker, R. T., Mayer, B., Neubauer, D., Hitzenberger, R., Oreopoulos, L., Lee, D., Pitari, G., Di Genova, G., Quaas, J., Rose, F. G., Kato, S., Rumbold, S. T., Vardavas, I., Hatzianastassiou, N., Matsoukas, C., Yu, H., Zhang, F., Zhang, H. & Lu, P. 2013. Intercomparison of shortwave radiative transfer schemes in global aerosol modeling: results from the AeroCom Radiative Transfer Experiment. *Atmospheric Chemistry and Physics,* 13**,** 2347-2379.

Redelsperger, J. L., Thorncroft, C. D., Diedhiou, A., Lebel, T., Parker, D. J., & Polcher, J. (2006). African monsoon multidisciplinary analysis - An international research project and field campaign. *Bulletin of the American Meteorological Society, 87*(12), 1739-+. doi:10.1175/Bams-87-12-1739

Redl, R., Fink, A. H. & Knippertz, P. 2015. An Objective Detection Method for Convective Cold Pool Events and Its Application to Northern Africa. *Monthly Weather Review,* 143**,** 5055-5072.

Redl, R., Knippertz, P. & Fink, A. H. 2016. Weakening and moistening of the summertime Saharan heat low through convective cold pools from the Atlas Mountains. *Journal of Geophysical Research-Atmospheres,* 121**,** 3907-3928.

Ridley, D. A., Heald, C. L. & Ford, B. 2012. North African dust export and deposition: A satellite and model perspective. *Journal of Geophysical Research-Atmospheres,* 117.

Rienecker, M. M., Suarez, M. J., Gelaro, R., Todling, R., Bacmeister, J., Liu, E., Bosilovich, M. G., Schubert, S. D., Takacs, L., Kim, G. K., Bloom, S., Chen, J. Y., Collins, D., Conaty, A., Da Silva, A., Gu, W., Joiner, J., Koster, R. D., Lucchesi, R., Molod, A., Owens, T., Pawson, S., Pegion, P., Redder, C. R., Reichle, R., Robertson, F. R., Ruddick, A. G., Sienkiewicz, M. & Woollen, J. 2011. MERRA: NASA's Modern-Era Retrospective Analysis for Research and Applications. *Journal of Climate,* 24**,** 3624-3648.

Roberts, A. J., Marsham, J. H. & Knippertz, P. 2015. Disagreements in Low-Level Moisture between (Re)Analyses over Summertime West Africa. *Monthly Weather Review,* 143**,** 1193-1211.

Roehrig, R., Bouniol, D., Guichard, F., Hourdin, F. & Redelsperger, J. L. 2013. The Present and Future of the West African Monsoon: A Process-Oriented Assessment of CMIP5 Simulations along the AMMA Transect. *Journal of Climate,* 26**,** 6471-6505.

Ryder, C. L., Highwood, E. J., Lai, T. M., Sodemann, H. & Marsham, J. H. 2013a. Impact of atmospheric transport on the evolution of microphysical and optical properties of Saharan dust. *Geophysical Research Letters,* 40**,** 2433-2438.

Ryder, C. L., Highwood, E. J., Rosenberg, P. D., Trembath, J., Brooke, J. K., Bart, M., Dean, A., Crosier, J., Dorsey, J., Brindley, H., Banks, J., Marsham, J. H., McQuaid, J. B., Sodemann, H. & Washington, R. 2013b. Optical properties of Saharan dust aerosol and contribution from the coarse mode as measured during the Fennec 2011 aircraft campaign. *Atmospheric Chemistry and Physics,* 13**,** 303-325.

Ryder, C. L., McQuaid, J. B., Flamant, C., Rosenberg, P. D., Washington, R., Brindley, H. E., Highwood, E. J., Marsham, J. H., Parker, D. J., Todd, M. C., Banks, J. R., Brooke, J. K., Engelstaedter, S., Estelles, V., Formenti, P., Garcia-Carreras, L., Kocha, C., Marenco, F., Sodemann, H., Allen, C. J. T., Bourdon, A., Bart, M., Cavazos-Guerra, C., Chevaillier, S., Crosier, J., Darbyshire, E., Dean, A. R., Dorsey, J. R., Kent, J., O'Sullivan, D., Schepanski, K., Szpek, K., Trembath, J. & Woolley, A. 2015. Advances in understanding mineral dust and boundary layer processes over the Sahara from Fennec aircraft observations. *Atmospheric Chemistry and Physics,* 15**,** 8479-8520.

Schepanski, K., Heinold, B., & Tegen, I. (2017). Harmattan, Saharan heat low, and West African monsoon circulation: modulations on the Saharan dust outflow towards the North Atlantic. *Atmospheric Chemistry and Physics, 17*(17), 10223-10243. doi:10.5194/acp-17-10223-2017

Schmetz, J., Pili, P., Tjemkes, S., Just, D., Kerkann, J., Rota, S. & Ratier, A. 2002. An introduction to Meteosat Second Generation (MSG) (vol 83, pg 977, 2002). *Bulletin of the American Meteorological Society,* 83**,** 1271-1271.

Schwarz, M., Folini, D., Hakuba, M. Z., & Wild, M. (2017). Spatial Representativeness of Surface-Measured Variations of Downward Solar Radiation. *Journal of Geophysical Research-Atmospheres, 122*(24), 13319-13337. doi:10.1002/2017jd027261

Seinfeld, J. H., Bretherton, C., Carslaw, K. S., Coe, H., DeMott, P. J., Dunlea, E. J., Feingold, G., Ghan, S., Guenther, A. B., Kahn, R., Kraucunas, I., Kreidenweis, S. M., Molina, M. J., Nenes, A., Penner, J. E., Prather, K. A., Ramanathan, V., Ramaswamy, V., Rasch, P. J., Ravishankara, A. R., Rosenfeld, D., Stephens, G. & Wood, R. 2016. Improving our fundamental understanding of the role of aerosol-cloud interactions in the climate system. *Proceedings of the National Academy of Sciences of the United States of America,* 113**,** 5781-5790.

Semazzi, F. H. M. & Sun, L. Q. 1997. The role of orography in determining the Sahelian climate. *International Journal of Climatology,* 17**,** 581-596.

Sheen, K. L., Smith, D. M., Dunstone, N. J., Eade, R., Rowell, D. P., & Vellinga, M. (2017). Skilful prediction of Sahel summer rainfall on inter-annual and multi-year timescales. *Nature Communications, 8*. doi:ARTN 1496610.1038/ncomms14966

Shekhar, R. & Boos, W. R. 2017. Weakening and Shifting of the Saharan Shallow Meridional Circulation during Wet Years of the West African Monsoon. *Journal of Climate,* 30**,** 7399-7422.

Simpson, J. E. 1969. A Comparison between Laboratory and Atmospheric Density Currents. *Quarterly Journal of the Royal Meteorological Society,* 95**,** 758-&.

Slingo, A., Ackerman, T. P., Allan, R. P., Kassianov, E. I., McFarlane, S. A., Robinson, G. J., Barnard, J. C., Miller, M. A., Harries, J. E., Russell, J. E. & Dewitte, S. 2006. Observations of the impact of a major Saharan dust storm on the atmospheric radiation balance. *Geophysical Research Letters,* 33.

Smith, E. A. (1986). The Structure of the Arabian Heat Low .2. Bulk Tropospheric Heat-Budget and Implications. *Monthly Weather Review, 114*(6), 1084-1102. doi:Doi 10.1175/1520-0493(1986)114<1084:Tsotah>2.0.Co;2

Sodemann, H., Lai, T. M., Marenco, F., Ryder, C. L., Flamant, C., Knippertz, P., Rosenberg, P., Bart, M. & McQuaid, J. B. 2015. Lagrangian dust model simulations for a case of moist convective dust emission and transport in the western Sahara region during Fennec/LADUNEX. *Journal of Geophysical Research-Atmospheres,* 120**,** 6117-6144.

Sokolik, I. N., Winker, D. M., Bergametti, G., Gillette, D. A., Carmichael, G., Kaufman, Y. J., . . . Penner, J. E. (2001). Introduction to special section: Outstanding problems in quantifying the radiative impacts of mineral dust. *Journal of Geophysical Research-Atmospheres, 106*(D16), 18015-18027. doi:Doi 10.1029/2000jd900498

Solmon, F., Elguindi, N. & Mallet, M. 2012. Radiative and climatic effects of dust over West Africa, as simulated by a regional climate model. *Climate Research,* 52**,** 97-113.

Stanelle, T., Vogel, B., Vogel, H., Baumer, D. & Kottmeier, C. 2010. Feedback between dust particles and atmospheric processes over West Africa during dust episodes in March 2006 and June 2007. *Atmospheric Chemistry and Physics,* 10**,** 10771-10788.

Stein, T. H. M., Parker, D. J., Hogan, R. J., Birch, C. E., Holloway, C. E., Lister, G. M. S., Marsham, J. H. & Woolnough, S. J. 2015. The representation of the West African monsoon vertical cloud structure in the Met Office Unified Model: an evaluation with CloudSat. *Quarterly Journal of the Royal Meteorological Society,* 141**,** 3312-3324.

Sultan, B. & Janicot, S. 2003. The West African monsoon dynamics. Part II: The "preonset'' and "onset'' of the summer monsoon. *Journal of Climate,* 16**,** 3407-3427.

Sultan, B., Janicot, S. & Diedhiou, A. 2003. The West African monsoon dynamics. Part I: Documentation of intraseasonal variability. *Journal of Climate,* 16**,** 3389-3406.

Tanaka, T. Y. & Chiba, M. 2006. A numerical study of the contributions of dust source regions to the global dust budget. *Global and Planetary Change,* 52**,** 88-104.

Tegen, I. & Lacis, A. A. 1996. Modeling of particle size distribution and its influence on the radiative properties of mineral dust aerosol. *Journal of Geophysical Research-Atmospheres,* 101**,** 19237-19244.

Tegen, I. (2003). Modeling the mineral dust aerosol cycle in the climate system. *Quaternary Science Reviews, 22*(18-19), 1821-1834. doi:10.1016/S0277-3791(03)00163-X

Thorncroft, C. & Hodges, K. 2001. African easterly wave variability and its relationship to Atlantic tropical cyclone activity. *Journal of Climate,* 14**,** 1166-1179.

Thorncroft, C. D. & Blackburn, M. 1999. Maintenance of the African easterly jet. *Quarterly Journal of the Royal Meteorological Society,* 125**,** 763-786.

Todd, M. C., Allen, C. J. T., Bart, M., Bechir, M., Bentefouet, J., Brooks, B. J., Cavazos-Guerra, C., Clovis, T., Deyane, S., Dieh, M., Engelstaedter, S., Flamant, C., Garcia-Carreras, L., Gandega, A., Gascoyne, M., Hobby, M., Kocha, C., Lavaysse, C., Marsham, J. H., Martins, J. V., McQuaid, J. B., Ngamini, J. B., Parker, D. J., Podvin, T., Rocha-Lima, A., Traore, S., Wang, Y. & Washington, R. 2013. Meteorological and dust aerosol conditions over the western Saharan region observed at Fennec Supersite-2 during the intensive observation period in June 2011. *Journal of Geophysical Research-Atmospheres,* 118**,** 8426-8447.

Todd, M. C. & Cavazos-Guerra, C. 2016. Dust aerosol emission over the Sahara during summertime from Cloud-Aerosol Lidar with Orthogonal Polarization (CALIOP) observations. *Atmospheric Environment,* 128**,** 147-157.

Tompkins, A. M. 2001. Organization of tropical convection in low vertical wind shears: The role of cold pools. *Journal of the Atmospheric Sciences,* 58**,** 1650-1672.

Trenberth, K. E. & Guillemot, C. J. 1995. Evaluation of the Global Atmospheric Moisture Budget as Seen from Analyses. *Journal of Climate,* 8**,** 2255-2272.

Trzeciak, T. M., Garcia-Carreras, L. & Marsham, J. H. 2017. Cross-Saharan transport of water vapor via recycled cold pool outflows from moist convection. *Geophysical Research Letters,* 44**,** 1554-1563.

Vaughan, M., Young, S., Winker, D., Powell, K., Omar, A., Liu, Z. Y., Hu, Y. X. & Hostetler, C. 2004. Fully automated analysis of space-based lidar data: an overview of the CALIPSO retrieval algorithms and data products. *Laser Radar Techniques for Atmospheric Sensing,* 5575**,** 16-30.

Vizy, E. K. & Cook, K. H. 2009. A mechanism for African monsoon breaks: Mediterranean cold air surges. *Journal of Geophysical Research-Atmospheres,* 114.

Washington, R., Todd, M., Middleton, N. J. & Goudie, A. S. 2003. Dust-storm source areas determined by the total ozone monitoring spectrometer and surface observations. *Annals of the Association of American Geographers,* 93**,** 297-313.

Washington, R. & Todd, M. C. 2005. Atmospheric controls on mineral dust emission from the Bodele Depression, Chad: The role of the low level jet. *Geophysical Research Letters,* 32.

Wei, N., Zhou, L. M., Dai, Y. J., Xia, G. & Hua, W. J. 2017. Observational Evidence for Desert Amplification Using Multiple Satellite Datasets. *Scientific Reports,* 7.

Weinzierl, B., Sauer, D., Minikin, A., Reitebuch, O., Dahlkotter, F., Mayer, B., . . . Schumann, U. (2012). On the visibility of airborne volcanic ash and mineral dust from the pilot's perspective in flight. *Physics and Chemistry of the Earth, 45-46*, 87-102. doi:10.1016/j.pce.2012.04.003

Weisman, M. L. & Klemp, J. B. 1982. The Dependence of Numerically Simulated Convective Storms on Vertical Wind Shear and Buoyancy. *Monthly Weather Review,* 110**,** 504-520.

Weisman, M. L. & Rotunno, R. 2004. "A theory for strong long-lived squall lines'' revisited. *Journal of the Atmospheric Sciences,* 61**,** 361-382.

Wielicki, B. A. 1996. Clouds and the Earth's radiant energy system (CERES): An earth observing system experiment (vol 77, pg 860, 1996). *Bulletin of the American Meteorological Society,* 77**,** 1590-1590.

Winker, D. M., Vaughan, M. A., Omar, A., Hu, Y. X., Powell, K. A., Liu, Z. Y., Hunt, W. H. & Young, S. A. 2009. Overview of the CALIPSO Mission and CALIOP Data Processing Algorithms. *Journal of Atmospheric and Oceanic Technology,* 26**,** 2310-2323.

Wu, X. Q. 1993. Effects of Cumulus Ensemble and Mesoscale Stratiform Clouds in Midlatitude Convective Systems. *Journal of the Atmospheric Sciences,* 50**,** 2496-2518.

Xue, Y. K., De Sales, F., Lau, W. K. M., Boone, A., Feng, J. M., Dirmeyer, P., Guo, Z. C., Kim, K. M., Kitoh, A., Kumar, V., Poccard-Leclercq, I., Mahowald, N., Moufouma-Okia, W., Pegion, P., Rowell, D. P., Schemm, J., Schubert, S. D., Sealy, A., Thiaw, W. M., Vintzileos, A., Williams, S. F. & Wu, M. L. C. 2010. Intercomparison and analyses of the climatology of the West African Monsoon in the West African Monsoon Modeling and Evaluation project (WAMME) first model intercomparison experiment. *Climate Dynamics,* 35**,** 3-27.

Yang, E. S., Gupta, P. & Christopher, S. A. 2009. Net radiative effect of dust aerosols from satellite measurements over Sahara. *Geophysical Research Letters,* 36.

Zhao, C., Liu, X., Leung, L. R., & Hagos, S. (2011). Radiative impact of mineral dust on monsoon precipitation variability over West Africa. *Atmospheric Chemistry and Physics, 11*(5), 1879-1893. doi:10.5194/acp-11-1879-2011

Zhou, L. M. 2016. Desert Amplification in a Warming Climate. *Scientific Reports,* 6.

Appendix

Table A1 All Stations Identified Cold Pools

Date	ΔTd	ΔU	U_av	Umax
AWS_134				
20110614 08:00	9.6	5.2	5.2	5.9
20110619 01:00	7.8	-1.1	4.1	6.3
20110621 09:00	5.5	3	5.1	5.6
20110621 18:30	9.7	8.1	11.1	12.2
20110625 21:30	5.4	1.4	5.2	5.5
20110627 21:30	4.6	4.5	9.7	11.6
20110705 06:00	11.5	2	8.5	9.3
20110710 02:00	20.6	7.9	10.4	11.2
20110710 23:30	7.2	6.3	8.6	9.7
20110714 22:00	10.6	2.8	4.6	5.3
20120617 23:30	8.5	5.9	7.8	10.3
20120622 10:00	15.1	1.7	11.5	11.9
20120622 22:00	5.6	10.8	13.8	14.8
20120627 02:00	14.5	4.4	6.7	9.5
20120629 09:00	10.5	2.5	10.2	11.4
20120630 02:00	7.7	2.5	6	9.4
20120702 23:30	3.9	1.2	4.4	8.6
20120705 05:00	5.8	6.7	12.2	12.5
20120711 03:30	8.6	3.2	4.1	4.9
20120716 08:00	7.7	8	9	9.9
20120717 04:00	23.4	4.8	7.3	9.1
20120717 22:00	11	7.6	8	10
20120719 10:00	4.4	3	6.3	7.2
20120719 19:26	3.5	1.5	5.3	6
20120720 01:00	3.8	6.8	8.7	10.4
20120725 03:00	9.8	3.3	5.9	7.7
20120729 01:30	14.5	1.6	7.5	9.1
20120731 02:00	16.1	5.5	7.9	8.5
20120808 09:00	7.2	4.4	11.1	11.8
20120809 19:30	5.3	8.6	13.5	15.3
20120812 09:00	8.1	6	7.4	8.9
20120815 20:00	4.5	3.8	7.2	7.9
20120819 19:00	16.7	8.6	11	12.5
20120820 23:00	8.3	5	9.2	10.2
20120821 18:00	10.2	6.5	7.5	8.6
20120824 05:00	10.6	-0.2	4.5	4.7
20120830 02:00	7.6	-0.2	4.2	4.7
20120830 23:00	4.9	7.8	10.6	13.2
20120831 23:00	11.3	8.4	11	12
20120904 18:30	5.7	3.4	7	9
20120920 07:00	12.4	3.4	9	10.1
S_131				

20120617 21:23	5.6	8.3	8.6	11.3
20120618 02:30	6	1.2	5.7	7.5
20120618 20:36	5.9	1.5	5.7	9.7
20120623 00:30	11.6	7.9	11.1	15.8
20120623 05:16	3.1	-0.4	6.1	7.8
20120623 13:00	3.8	2.3	10.1	10.9
20120629 22:00	11.1	6.2	8.6	10.7
20120701 02:00	3.4	2.7	4.4	6
20120702 21:30	7.7	6.9	7.4	8.5
20120720 19:30	5.8	3.5	8.3	9.3
20120722 00:16	17.9	2.1	3.1	4.8
20120725 23:00	4.6	3.2	7.2	8.6
20120726 08:30	9.7	-1.3	6.5	8.4
20120729 07:33	16.3	7.4	10	10.7
20120729 21:00	6.5	1.2	5.5	7.1
20120730 02:00	3.4	5.1	8.6	9.9
20120731 01:16	15.8	3	6	6.9
20120731 20:00	4.9	5.9	7.4	8.5
20120807 07:46	7.5	0.5	4.5	5.2
20120807 21:23	3.1	3.6	3.7	4.7
20120809 17:30	4.9	2.7	6.5	7.3
20120809 23:00	6.9	5.6	12.9	14.1
20120819 22:00	14.8	8	10.2	11.5
20120821 01:00	7.1	3.4	6	7.1
20120824 17:30	8.2	4.1	8	9.5
20120831 07:00	11.2	1	5.3	6.2
20120831 19:23	3.1	2.8	4.9	5.5
20120904 18:00	4.7	1.9	11.4	15.5
20120904 23:00	5.3	3.7	8	8.5
20120905 17:30	9.5	1.5	6.7	12
20120906 02:00	3.5	2.1	4	4.9
20120920 17:00	10.1	4.1	10	10.7
S_133				
20120618 13:00	5.3	1.2	7.9	8.9
20120630 10:00	4.1	-1.2	8.8	10.1
20120703 08:23	6.7	3.5	11.2	12.5
20120706 16:20	4.3	5.8	12	12.4
20120820 14:46	3.1	-0.5	5.7	9
20120901 08:26	7.3	2.9	9.4	10.5
20120905 15:03	4.3	6.6	13.1	16.2
S_135				
20120623 19:30	19.8	7.8	9.6	12.9
20120703 21:00	11.5	3.1	4.6	7.1
20120705 17:00	3.5	-1.5	5.2	9.5
20120713 03:00	5.8	-0.8	5.1	6.1
20120718 08:00	3	4	8	8.7
20120720 20:00	4	3.3	4.1	7.3

20120721	19:00	6.4	5	11.2	13
S_136					
20110617	**15:30**	3.5	3.8	5.7	6.5
20110618	17:16	3.2	2.8	4.5	8.5
20110630	16:00	3.8	2	4.7	6.1
20110713	**15:30**	3.3	1.8	5.2	6.6
20110823	**19:06**	5	2.1	3.9	7
20120603	**04:00**	9.6	1.8	6.7	9.1
20120603	17:00	5	6.3	8.9	9.5
20120603	20:00	3.2	3.3	6.9	8.7
20120605	19:30	6	4.3	6.4	8.7
20120606	23:30	6.4	3.2	5.4	9.6
20120612	20:00	9.6	3.3	6.9	8.4
20120616	14:30	9	3.8	8.1	9.3
S_138					
20110604	**06:00**	10.5	1.4	5.8	7.8
20110611	06:30	12.3	4.4	6.7	8.6
20110621	00:00	8.5	7.7	11.1	12.8
20110711	**05:30**	5.6	2.2	4.2	5.2
20110802	**05:00**	3.1	3.5	3.9	4.9
20110803	23:43	3	5.8	8.2	9.7
20110808	03:00	7.6	1.8	5.5	8.6
20110829	10:00	3.3	2.5	5.1	6.2
20110829	19:00	6.4	1.8	5.1	6.2
20110830	15:00	4.4	6.7	12.1	15.8
20110830	20:20	3.1	-2.4	7.7	10.7
20110909	**00:13**	3	2.1	3.2	4.1
20110915	00:00	9	-0.3	4.6	5.2
20110928	07:06	3	2.8	2.9	3.2
20110928	21:00	12	2.2	7.9	12.2
20120617	**01:30**	3.1	3	6.8	10.3
20120618	07:00	4.7	3.1	10.2	11.6
20120618	19:30	7.9	-0.3	7	12.1
20120619	17:30	3.4	-0.5	5.5	7.1
20120620	15:33	3.9	3.8	8	11.6
20120620	21:36	3.5	2.3	3.6	5.5
20120624	01:00	3.4	3.3	3.3	5.2
20120703	**01:13**	3	0.6	4.6	5.9
20120705	20:00	10.1	4.9	7.5	10
20120708	04:00	4.1	2.1	3.9	4.5
20120816	**16:36**	3.2	5.2	10.7	12.6
20120817	08:06	3.2	2.1	4.8	6.2
20120817	18:00	3.6	2.3	4.2	5.2
20120817	22:00	3.5	1.3	6.8	8.7
S_140					
20110602	**08:00**	10.6	5.6	7.4	8.6
S_141					

20110922	**21:00**	11.5	3.5	5	6.5
20110923	21:00	3.2	1.5	5.6	6.9
20110929	20:00	6	1.9	5.1	5.9
20120628	**01:00**	10.5	2.4	3.7	5.1
20120628	19:00	4.1	3	5.3	6.4
20120629	15:00	6.1	4.2	7.4	8.3
20120716	**23:16**	11.2	2.1	2.6	3.5
20120721	20:00	7.5	2.4	6.2	7.4
20120801	**19:00**	13.8	4.5	6.5	8.9
20120802	22:00	12.5	2.9	3.9	4.3
20120811	22:00	3	3	4.6	6.6
20120813	19:06	4.7	1.5	4.6	6.3
20120817	05:23	3.9	-0.3	4.7	6.1
20120817	18:00	6.9	1.1	4.9	7.2
20120821	20:00	7.3	3.8	5.9	7.1
20120823	21:00	3.9	-1.7	7.2	8.5

Table A2 Cold Pools dates missed by my detection algorithm and due to data unavailability (red highlighted) but observed on SEVIRI

YYYY/mm	131	133	134	135	136	138	141
2011/06	21/~05:00		12/~03:30	20/~00:00		05/~20:30	20/~05:30
	22/~07:00		13/~12:30	23/~08:00	12/~19:00		
			13/~21:30		13/~21:00		
			14/~01:30		22/~03:00		
			18/~03:00		24/~04:30		
			30/~01:30		30/~06:00		
2011/07			01/~01:30		10/~00:30[b]	15/~21:00[d]	
			15/~00:45		14/~12:30		
			16/~00:45		14/~16:15		
			18/~00:00		15/~20:30		
			22/~21:00		18/~04:00		
			28/~03:15		22/~18:30		
			31/~02:00		31/~18:00		
			31/~22:45				
2011/08					06/~05:30	05/~02:00	
					06/~21:15	07/~07:00	
					14/~07:00	19/~06:00	
					20/~17:45		

					27/~03:00		
					27/~16:45		
2011/09					27/~21:30		
2012/06	19/~06:30	23/~05:30	16/~17:30[d]	11/~03:00	04/~18:00	22/~22:00	24/~00:30[b]
	22/~19:30		18/~22:30	16/~20:45	07/~21:00	30/~23:00	
	27/~05:00		29/~21:00		13/~01:30	22/~02:00	
	29/~18:30				13/~17:30	31/~04:00[s]	
	30/~19:00				21/~22:00	31/~20:00[d]	
					29/~04:00		
					29/~21:00		
2012/07	05/~09:00	13/~03:30	31/~14:30	15/~23:00[d]			13/~16:00
	13/~01:00	18/~02:30s		19/~15:45[d]			16/~04:00
		21/~04:00					
		21/~18:00					
		30/~05/15					
2012/08	16/~23:30	01/~02:00	06/~22:00			09/~22:00	08/~21:00
	24/~08:00	03/~01:15	16/~21:00				17/~11:45
		08/~03:00					
		10/~04:00					
		16/~31:15					
		20/~04:30					
		25/~01:00					
		01/~20:00					
2012/09	05/~19:45					02/~03:00	
	21/~19:15					05/~18:00	
						21/~21:00	

[d]Dust, [b]Big [s]Small based on SEVIRI imagery